LINEARIZED INVERSE THEORY APPLIED TO DIRECT CURRENT RESISTIVITY MEASUREMENTS

by

DONALD H. PLENDERLEITH

B.Sc.(honours Geophysics), University Of B.C., 1980

A THESIS SUBMITTED IN PARTIAL FULFILMENT OF

THE REQUIREMENTS FOR THE DEGREE OF

MASTER OF SCIENCE

in

THE FACULTY OF GRADUATE STUDIES

Department Of Geophysics And Astronomy

We accept this thesis as conforming

to the required standard

THE UNIVERSITY OF BRITISH COLUMBIA

May 1983

© Donald H. Plenderleith, 1983

In presenting this thesis in partial fulfilment of the requirements for an advanced degree at the University of British Columbia, I agree that the Library shall make it freely available for reference and study. I further agree that permission for extensive copying of this thesis for scholarly purposes may be granted by the head of my department or by his or her representatives. It is understood that copying or publication of this thesis for financial gain shall not be allowed without my written permission.

Department of Geophysics + Astronomy

The University of British Columbia
1956 Main Mall
Vancouver, Canada
V6T 1Y3

Date July 1983

DE-6 (3/81)

Abstract

Layered resistivity models have been constructed from the potential difference measurements made in direct current resistivity soundings using Backus and Gilbert's linearized inverse theory in a manner similar to that of Oldenburg (1978). The efficiency of the original method has been improved by approximating the one-dimensional structure with a finite number of layers, and by computing the Hankel transforms used in evaluating the Fréchet kernels, and solving the forward equation, with a digital filter. Also, the surface resistivity is no longer required thus making the method fully automatic.

The constructed model's representation of a hypothetical resistivity structure was tested, varying the starting model, adding up to 20 percent noise to the synthetic data, and decreasing the data density. In all cases the hypothetical structure was recognizably reproduced.

With the program's ability to reproduce this structure verified, six Schlumberger soundings in the Anahim Volcanic belt in British Columbia were inverted. Although the setting was not ideal, models which fit the data according to the chi-squared criterion were constructed. A standard deviation of 10 percent was assigned to the data to account for measurement errors, and invalidity of the flat one-dimensional earth approximation made in solving the potential equation.

From the models constructed and the known near-surface geology, three integrated interpretations were made. The first is a purely geological interpretation of the low resistivity zones. In the second, they are attributed to increasing temperatures with depth and to the north, and a heat source north of the survey region is hypothesized from an observed north-south resistivity gradient. The third is the most probable interpretation. In it, the heat source to the north is retained because it is inferred from a trend of decreasing average resistivities indicated by the four northernmost soundings, but one of the remaining southern anomalies is questioned, and a geological explanation is given for the other. There was not enough information in this data set to favor either the hot-spot, or the edge effect hypothesis for the genesis of the Anahim Volcanic belt.

The two soundings most important to the heat-source-to-the-north hypothesis were linearly appraised. Average models have been constructed with a predetermined standard deviation and, on the basis the low resistivity zones being present, it can be said that the features which form the basis of this hypothesis are resolvable.

Table of Contents

Abstract ii

List of figures vii

Acknowledgements ix

AN INTRODUCTION 1

CHAPTER 1 The Basic Equations of Resistivity 5

1-1 The Potential Equation 5

1-2 Obtaining the Fréchet Kernels 10

CHAPTER 2 Construction of Resistivity Models 15

2-1 Backus and Gilbert's Linearized Construction 16

2-2 Smallest Perturbation Construction 17

2-3 Flattest Perturbation Construction 20

2-4 Errors and their Infuence 23

2-4.1 Sources of Error 24

2-4.2 How Errors are Accomodated 26

2-4.3 Final Considerations Regarding Perturbations 31

2-5 Computing Hankel Transforms 34

2-6 Testing the Linearized Construction Program 40

2-6.1 Objectives 40

2-6.2 Effects of the Starting Model 41

2-6.3 Effects of Noise and Data Density 52

2-6.4 Representation Testing 55

CHAPTER 3 A Resistivity Survey in the Anahim Belt 59
3-1 The Anahim Resistivity Project 60
3-2 Causes of Resistivity Anomalies in Geothermal Areas ..63
3-3 Geological Settings of the Schlumberger Soundings 65
3-4 Constructions Obtained from the Schlumberger Data 69
3-5 Results from the Dipole-Dipole Line 78
3-6 Geological-Geothermal Interpretations 79
3-6.1 Simplest Model with Geological Constraints 80
3-6.2 Regional Heating Model 82
3-6.3 Most Probable Model 85
3-7 Correlation with the Larger Scale Tectonic Picture ...86
3-7.1 Geological History of the Anahim Belt 87
3-7.2 Fit to the Hot-Spot Trace Hypothesis 92
3-7.3 Fit to the Edge Effect Hypothesis 93

CHAPTER 4 Appraisal 95
4-1 Objectives of Appraisal 95
4-2 Linearized Appraisal 96
4-2.1 Averaging Functions and Model Averages 97
4-2.2 Deltaness Criterion 101
4-2.3 The Tradeoff Between Resolution and Accuracy 104
4-3 Appraisal of some Schlumberger Constructions 107
4-4 Towards Comprehensive Appraisal 114

CONCLUSION 117

BIBLIOGRAPHY 121

Appendix A Evaluation of the Modal Coefficient $A(\lambda)$ 125

Appendix B Solving for $H(z,\lambda)$ in a Layered Medium 129

Appendix C Fréchet Differentiability 134

Appendix D Evaluating Indefinite Integrals 141

Appendix E Winnowing Eigenvalues 144

Appendix F The Schlumberger Data Set 147

List of Figures

1.1 Notation used for any electrode configuration 8
1.2 Layering convention 9

2.1 Perturbation processing 33
2.2 True structure, apparent res. and starting models tested 42
2.3 Smallest perturbation construction from 7.8 ohm-meters ..44
2.4 Smallest perturbation construction from 13.4 ohm-meters .45
2.5 Smallest perturbation construction from 34 ohm-meters ...47
2.6 Flattest perturbation construction from 7.8 ohm-meters ..49
2.7 Flattest perturbation construction from 13.4 ohm-meters .50
2.8 Construction using automatic starting model selector 51
2.9 Constructions from noisy data 53
2.10 Constructions obtained varying data density 55
2.11 Construction with a half-space as the true structure ...56
2.12 Construction with a box car as the true structure 57

3.1 B.C. showing the Anahim Volcanic belt 60
3.2 The Schlumberger survey region 61
3.3 A potential difference record 62
3.4 Effects of temperature and salinity on the resistivity of water 64
3.5 Geological setting of VES 1 66
3.6 Geological setting of VES 5 68
3.7 VES 1 constructions 71
3.8 VES 2 construction 72
3.9 VES 3 constructions 73

3.10 VES 4 constructions 75

3.11 VES 5 constructions 76

3.12 VES 6 construction 78

3.13 The resistivity gradient inferred from VES 1,2,3,and 6 .85

3.14 Plate boundaries and volcanic chains 89

3.15 Mechanism for Stacey's edge effect hypothesis 93

4.1 The resistivity gradient 108

4.2 Tradeoff curve at 150 m for VES 2 109

4.3 VES 2 Average model with σ=0.25 110

4.4 VES 1 Average model with σ=0.3 112

4.5 VES 5 constructions and average model 113

4.6 Schematic showing appraisal methods and nonuniqueness ..116

Acknowledgments

I feel very fortunate at having had such a rewarding thesis topic, and I am grateful to Doug Oldenburg for suggesting it. His intimate knowledge of inverse theory, and of the D.C. resistivity problem in particular, were invaluable in this work – especially in getting the construction program operational.

For their part in providing the data, and for several discussions regarding the Anahim resistivity project, I wish to thank Greg Shore and Michael Schlax of Premier Geophysics. I also appreciate Dr. J.G. Souther of the Geological Survey of Canada permitting us the use of this data before it was released in the open file report.

Other faculty members I have enjoyed working with on field experiments and as a teaching assistant are Drs. R.M. Clowes, W.F. Slawson, and T. Watanabe.

Through the M-T discussion group, I received exposure to the closely related magnetotelluric problem, and learned a few useful tricks. Wang, Kerry, and Ken also gave me advice on various aspects of my problem.

During my stay in the Department of Geophysics and Astronomy I have enjoyed the superb company of many of the other graduate students and their partners. Those whom I got to know well were: Brad Prager, Ian and Gemma Jones, Jim Horn, David Waldron, Max and Allison, Wang, Julian Cabrera, Ed Waddington, and Lynda Fisk.

AN INTRODUCTION

Measuring the earth's resistance to the flow of electric current is the central purpose behind all of the electric and electromagnetic methods used in geophysics. When the resistivity structure is known, information on rock types, porosities, and temperatures of the earth may then be inferred. In the direct current resistivity method, potential differences in the presence of an electro-static field are measured. These measurements constitute a data set which can be inverted to yield resistivity information as a function of depth. In this thesis linearized inverse methods are used to construct and appraise resistivity models. Geological and geothermal interpretations are made from data taken in the Anahim Volcanic Belt of British Columbia.

The resistivity method was first successfully applied in 1912 by Conrad Schlumberger. He was the first to introduce electric currents to the earth using a current circuit and measure the potential differences with a separate circuit. This is still the essence of any resistivity experiment done today. Earlier workers had either tried to measure the resistance between two electrodes with a current flowing between them, or used the right circuits with frequencies that were too high. Neither of these methods allow the electric field much depth of penetration.

The understanding behind resistivity measurements has advanced tremendously since 1912. By 1925 Stefanesco, Kostitzn, and Maillet had a patent on measuring the depth to a horizontal layer using resistivity, and Gish and Rooney had

published papers on determining the true resistivity structure from potential measurements (Kunetz,1966). In 1933 R.E. Langer published "An inverse problem in differential equations" in which he obtained the true vertical resistivity distribution from apparent resistivity curves. Further, he showed how it is uniquely determined by the complete set of apparent resistivities. This still stands as the uniqueness proof for resistivity models.

The first major publication in an American journal appeared in 1947 wherein Maillet extolled the virtues of the resistivity method to the American audience and introduced Dar Zarrouk parameters as a means of calculating surface potentials. Prior to that data, interest in the electrical methods had existed only in Europe, China, and the USSR.

As the body of knowledge about resistivity grew, interpretation methods became increasingly sophisticated. Conrad Schlumberger measured the potential distribution on a grid near a current electrode and contoured it to produce an equipotential map. He compared this to the potential distribution of a half-space and made interpretations based upon the differences between the two equipotential maps. The number of measurements mapping the potential involves is in the hundreds.

After the potential equation was solved, it became possible to compute the apparent resistivity curves for any layered structure, and curve matching became the premier interpretation method. Several catalogues of apparent resistivity curves exist; the original, compiled by Orella and

Mooney (1966), had a hundred and forty such curves.

Shortly thereafter, direct interpretation methods were started. Koefoed in 1966 used raised kernel functions to calculate resistivities and layer thicknesses from data over a one dimensional earth, and Zohdy developed a fast iterative scheme using modified Dar Zarrouk functions (Zohdy, 1975). Generalized inverse theory, and later ridge regression were employed by Inman to invert potential differences over a layered earth (Inman et al, 1973; Inman, 1975). And in 1978, Oldenburg used Backus and Gilbert's linearized inverse theory to construct and appraise continuous one dimensional models (Oldenburg, 1978). Models have also been constructed using Weidelt's inverse scattering method which, unlike the linearized method, solves the full nonlinear equation (Cohen and Wu, 1981). At present though, the ability to appraise models lags somewhat behind the ability to construct them, and the problem of nonuniqueness still looms.

In this thesis linearized inverse theory is used to invert potential measurements in a way very similar to that formulated by Oldenburg (1978). Here though, layered models are constructed, and knowledge of the surface resistivity is not required. Also, the filter method of Gosh (1971) is used to calculate the Hankel transforms used in the potential equation and in the Fréchet kernels. This greatly reduces the computation time.

The advantage of using Backus and Gilbert's linearized construction is that the kernel functions for linearized appraisal are automatically available. Those kernels are

combined to give unique averages of earth resistivity, provided that the constructed models, and the earth model, are linearly close. Most often though, there is not enough data to guarantee linear closeness to the real earth, but linearized appraisal can be used to determine which features are common to the set of models linearly close to the constructed model.

Within linearized construction, various selection criterion exist for choosing model perturbations. Here, the smallest and flattest perturbations are used to construct models from real and synthetic data, but there is no limit to the number of perturbations that could also have been used.

The models constructed from the Anahim data are interpreted for temperatures and geological information, and three geological-geothermal explanations for the models are given. Lastly, those models which were most important to the most probable interpretation are linearly appraised.

Chapter 1

The Basic Equations of Resistivity

The potential distribution over an earth in which the resistivity varies as a function of depth will be developed here. A direct current source at r=0 on the surface produces the electo-static field, and potential differences measured in this field are inverted to obtain a resistivity model as a function of depth.

1-1 The Potential Equation

Just as in circuitry, Ohm's Law relates current and resistivity to the electro-static potential.

$$E = \rho J \tag{1.1}$$

Expressing E as the gradient of the potential, V, and using the fact that the divergence of J is zero when there are no current sources in the region results in the conservation of current condition.

$$\nabla \cdot J = \nabla \cdot \frac{-\nabla V}{\rho} = 0 \tag{1.2}$$

When the resistivity is constant, equation (1.2) is Laplace's equation for V which is easily solved; however a depth dependent resistivity will give rise to a second term.

$$\frac{1}{\rho(z)} \nabla^2 V + \nabla \frac{1}{\rho(z)} \cdot \nabla V = 0 \qquad (1.3)$$

Since the potential distribution has circular symmetry around the current source and varies with depth, cylindrical coordinates are most amenable to solving this equation. Z is positive downwards, and there is no θ dependence. Let

$$V(r,z) = R(r)\, H(z).$$

Separating the variables in equation (1.3) yields a Bessel's equation for R, and an equation of the Sturm-Liouville type for H.

$$R'' + \frac{1}{r} R' + \lambda^2 R = 0 \qquad (1.4a)$$

$$H'' - \frac{\rho'}{\rho} H' + \lambda^2 H = 0 \qquad (1.4b)$$

Of the two kinds of zeroth order Bessel functions which solve (1.4a), only the first is retained because of the seconds characteristics near r=0. At this point the solution for the potential is an integral over the continuous eigenmodes of these two solutions. $A(\lambda)$ is a modal coefficient.

$$V(r,z) = \int_0^\infty A(\lambda)\, H(\lambda,z)\, J_0(\lambda r)\, d\lambda \qquad (1.5)$$

There are many ways of evaluating $A(\lambda)$. Langer(1933), using the condition that $\frac{\partial V}{\partial z} = 0$ everywhere on the earth's surface except at the current electrode obtained:

$$V(r,z) = \frac{-I\rho_0}{2\pi a} \int_0^\infty \frac{H(z,\lambda)}{H'(0,\lambda)} \sin\lambda a \; J_0(\lambda r) \; d\lambda$$

where 'a' is the diameter of the current electrode. Stefanesco(1930) solved for V in the near and far field and combined the solutions.

$$V(r,z) = \frac{I\rho_0}{2\pi}\left[\frac{1}{r} + 2\int_0^\infty K(\lambda,k,d)J_0(\lambda r) \; d\lambda \right],$$

where $K(\lambda,k,d)$ is a kernel dependent upon layer thicknesses and resistivities, and Oldenburg(1978) used the condition that the surface integral of current density over an infinitely long cylinder centred around the current source must equal the input current, I. This condition provides the most compact expression for the potential and is used in appendix A to evaluate $A(\lambda)$.

$$A(\lambda) = \frac{-I\lambda}{2\pi} \frac{\rho_0}{H'(0,\lambda)}$$

Therefore:

$$V(r,0) = \frac{-I\rho_0}{2\pi} \int_0^\infty \lambda \frac{H(0,\lambda)}{H'(0,\lambda)} J_0(\lambda r) \; d\lambda \qquad (1.6)$$

Field measurements, however, are potential differences between two points, m and n, in the presence of two current electrodes at positions a and b. The potential difference is then:

$$\Delta V = V(r_{am}) - V(r_{an}) + V(r_{bn}) - V(r_{bm})$$

where r_{am} is the distance between current electrode, m, and the potential electrode, a.

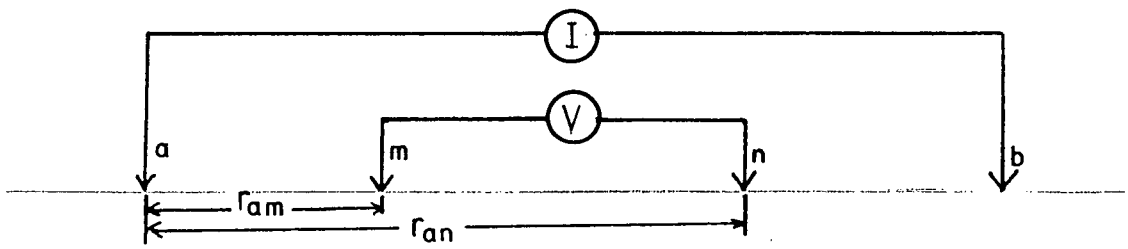

Figure 1.1 Notation for any electrode configuration. Any type of resistivity array can be specified by the four distances ram, ran, rbn, and rbm. Referring to the separations in this way, gives the method its universal applicability.

For the i'th electrode configuration, let Ci(λ) represent

$$J_0(\lambda r_{am}) - J_0(\lambda r_{an}) + J_0(\lambda r_{bn}) - J_0(\lambda r_{bm}) \qquad (1.7)$$

then,

$$\Delta Vi = \frac{-I\rho_0}{2\pi} \int_0^\infty \lambda \frac{H(0,\lambda)}{H'(0,\lambda)} Ci(\lambda)\, d\lambda \qquad (1.8)$$

If V and ρ were linearly related, ρ would appear in this integral. Their relationship, however, is nonlinear and ρ enters into it as a variable in the Sturm-Liouville equation for H (equation (1.4b)). Calculating $H(0,\lambda)$ and $H'(0,\lambda)$ was a time consuming step in the continuous structure inversion of Oldenburg(1978), but by assuming a multi-layered earth in which ρ is constant and isotropic within each layer, the difficulty and time involved in computing $H(0,\lambda)$ and $H'(0,\lambda)$ can be greatly reduced. Using this assumption, equation (1.4b) simplifies to

$$Hj''(z_j) - \lambda^2 Hj(z_j) = 0 \qquad (1.9)$$

in the j'th layer, where z_j is the depth from the top of the j'th layer.

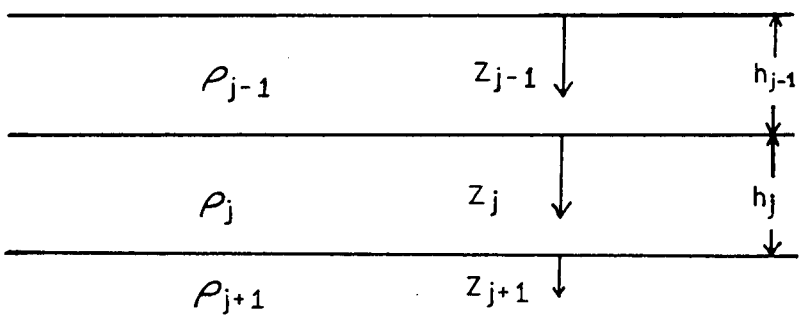

Figure 1.2 Layering convention. The layers are indexed by their lower boundary. The thickness of the j'th layer is h_j, and z_j is the distance down from the top boundary. Each z_j is only defined from 0_j to h_j.

The boundary conditions are continuity of potential and current across a layer interface. These, plus the condition that the current density must decay to zero at great depth, are used in appendix B to solve for $H(0,\lambda)$. The solution is analytic and therefore obtaining $H'(0,\lambda)$ presents no added difficulty.

1-2 Obtaining the Fréchet Kernels

The approach taken here in constructing a resistivity model which fits the data is to first make an initial guess, and then iterate to a better-fitting model. Successive iterations are made, if neccessary, until the model reproduces the observed data to within the experimental error bounds (equation (1.8)). To iterate successfully, the model must be perturbed in such a way that the misfit between measured and calculated potential differences is minimized. Accomplishing this requires relating changes in the model to changes in the data, then model perturbations implied by the misfit to the data can be made, resulting in an improved model. This procedure is simply Newton's method with the extension that we are solving for a vector, the model, in place of a single variable, and is repeated until the misfit is down to an acceptable level.

Normalizing the potential differences to unit current, and absorbing the geometric constants results in a more convienient quantity to use as data. The i'th datum is :

$$Ei = \frac{\Delta Vi}{I} 2\pi = -\rho_o \int_o^\infty \lambda \frac{H(0,\lambda)}{H'(0,\lambda)} Cj(\lambda)\, d\lambda \qquad (1.10)$$

Although the data are nonlinear in ρ, they are linear in the quantity $H(0,\lambda)/H'(0,\lambda)$. By defining $H(z,\lambda)/H'(z,\lambda)$ as $S(z,\lambda)$, a linear relationship is established which facilitates calculating the Fréchet kernel.

$$Ei = -\rho_0 \int_0^\infty \lambda S(0,\lambda) Ci(\lambda)\, d\lambda \qquad (1.11)$$

The usefulness of S is now clear; it is linearly related to the datum, Ei. A small perturbation in S is therefore linearly related to a small perturbation in Ei.

$$\delta Ei = \rho_0 \int_0^\infty \lambda \delta S(0,\lambda) Ci(\lambda)\, d\lambda \qquad (1.12)$$

With the definition of w(z) as $\rho'(z)/\rho(z)$, and substitution of both new variables into equation (1.4b) the Riccatti equation in S is obtained (Oldenburg, 1978).

$$S' + wS + \lambda^2 - 1 = 0 \qquad (1.13)$$

To find δS, S and w are perturbed and substituted back into (1.13). The perturbed versions of S and w are:

$$S_1(z,\lambda) = S(z,\lambda) + \delta S(z,\lambda), \qquad (1.14a)$$

and

$$w_1(z) = w(z) + \delta w(z) \qquad (1.14b)$$

Then the new functions S_1 and w_1 are substituted into equation (1.13), and the unperturbed version is subtracted out. After throwing away the second order terms an equation for $\delta S(z,\lambda)$ remains.

$$\delta S' + (w + 2S\lambda^2)\delta S + \delta w S = 0 \qquad (1.15)$$

Using standard techniques, (Boyce+Diprima, 1977) the integrating factor H'^2/ρ is found.

$$\frac{(\delta S\ H'^2)'}{\rho} + \frac{\delta w H H'}{\rho} = 0$$

Integrating from 0 to ∞,

$$\frac{\delta S\ H'^2}{\rho}\Big|_0^\infty = \int_0^\infty -\frac{\delta w H H'}{\rho}\ dz \qquad (1.16)$$

as $z \longrightarrow \infty$, $H'(\lambda,z) \longrightarrow 0$, (for $\lambda=0$) therefore the first term has no contribution at ∞.

$$\delta S(0,\lambda)\ \frac{H'(0)^2}{\rho(0)} = \int_0^\infty \frac{HH'\delta w(z)}{\rho(z)}\ dz\ ,$$

so

$$\delta S(0,\lambda) = \frac{\rho_0}{H'(0)^2}\int_0^\infty \frac{HH'\delta w(z)}{\rho(z)}\ dz \qquad (1.17)$$

Now through δS, the change in data resulting from a perturbation in resistivity of $\delta\rho(z)$ is available. Substituting equation (1.17) into (1.12), and changing the order of integration identifies the kernel for δEi in terms of known variables.

$$\delta Ei = \int_0^\infty Fi(z)\,\delta w(z)\,dz$$

where,

$$Fi(z) = \frac{-\rho_0^2}{\rho(z)} \int_0^\infty \frac{\lambda H(z,\lambda) H'(z,\lambda)}{H'(0,\lambda)^2}\,d\lambda \qquad (1.18)$$

This form of the perturbation equation, although mathematically fine, requires solving $\delta w(z)$ for $\delta\rho(z)$. Choices of perturbations other than $\delta w(z)$ are possible provided that the kernels are modified correspondingly. Recent work by Wang (personal communication, 1982) seems to indicate that the resolution width in linearized appraisal is dependent upon the choice of model, and general resistivity level of the environment. In highly resistive environments conductivity models gave better resolution than resistivity models. A priori knowledge could be an asset here, as it would be in many aspects of inverse theory, however it trades off against universal applicability. Only one form of model will be used here. Choosing $\ln(\rho(z)/\text{ohm-meters})$ as that dimensionless model and relating it to $\delta w(z)$ using the chain rule and the fundamental theorem of Calculus,

$$m(z) = \ln(\rho(z)/\text{ohm-meters})$$

$$\frac{d\,m(z)}{dz} = \frac{\delta\rho'(z)}{\delta\rho(z)} = \delta w(z) \qquad (1.19)$$

Substituting this expression for $\delta w(z)$ into equation (1.18), and integrating by parts yields the Fréchet kernels for these models, $Gi(z)$.

$$\delta Ei = \int_0^\infty Gi(z)\,\delta m(z)\,dz,$$

where

$$Gi(z) = \frac{-\rho_0^2}{\rho(z)} \int_0^\infty \lambda \left[\frac{\lambda^2 H(z,\lambda)^2 + H'(z,\lambda)^2}{H'(0,\lambda)^2} \right] J_0(\lambda z)\,d\lambda \qquad (1.20)$$

is the Fréchet kernel for the i'th datum. Through it, the change in the model required to minimize the misfit to the data can be found. Throughout this derivation it has been assumed that the functional $Ei(m(z))$ varies continuously with $m(z)$; this is the requirement for Fréchet differentiability. See Appendix C for the definition of Fréchet differentiability.

It must be remembered that the Fréchet differential (1.20) is only a linear approximation to the change δEi brought about by δm. Thus, the accuracy of equation (1.20) depends upon the linearity of the functional in the region of the model, or equivalently, upon the existance of higher order Fréchet derivatives.

Chapter 2

Construction of Resistivity Models

Given the set of potential differences measured in a resistivity experiment, the construction problem is to find a one-dimensional resistivity model which reproduces those data to within the experimental error bounds. By the nonlinear nature of the physics involved, data are more easily calculated given a certain model, than a model is, given a set of data. This is put to our advantage in an iterative solution for a model.

An acceptable model, one which fits the data, is constructed in a number of steps, the first of which is judiciously choosing a starting model, m_0. A constant resistivity half-space is the most frequently chosen starting model for two reasons. The data are easily calculated from this model since the equation is analytic,

$$Ei = \rho_0 \left(\frac{1}{r_{am}} - \frac{1}{r_{an}} + \frac{1}{r_{bn}} - \frac{1}{r_{bm}} \right) \qquad (2.0)$$

for the i'th configuration.
(see figure 1.1)

and secondly, when construction is started from a model with no structure, there is no ambiguity about which parts of the final model were constructed, and which are simply remnants of the initial model. If a half-space is chosen, it should lie within the upper and lower bounds of the apparent resistivity curve, and also be the best flat line through that set of

points. The starting model's effect on the final model is investigated in section 2.6.

Once the data from a starting model have been computed via the forward equation, the difference between each of the measured data and the corresponding computed datum is calculated. If this difference is less than the experimental error, an acceptable model was chosen. Otherwise, the Fréchet kernels are calculated at the starting model, and the misfits to the data are approximated by Fréchet differentials. Equation (1.20) is then solved for the perturbation vector, $\delta m(z)$.

The perturbation is then added to the initial model, and data are recomputed for the updated model. Misfits are again calculated, and depending upon their size, another iteration is made to improve the model further. This is a direct application of the linearized construction method of Backus and Gilbert (1967).

2-1 Backus and Gilbert's Linearized Construction

The essence of Backus and Gilbert construction is in the solution of the perturbation equation. A vector $\delta m(z)$ is found which solves the linear equations.

$$\delta Ei = \int_0^\infty Gi(z)\,\delta m(z)\,dz \quad \text{for } (i=1,n) \qquad (2.1)$$

Here δEi is the difference between the i'th measured datum, and the i'th computed datum for a certain model, m. The

Fréchet kernel, Gi(z) is also model dependent, and is sometimes written as Gi(z,m(z)) to emphasize this dependency. As it has been shown in appendix C, the data functionals in the D.C. resistivity problem are Fréchet differentiable for any model vector in L_2, therefore the existence of the Fréchet kernel for any model in L_2 is guaranteed.

The integal (2.1) actually expresses the differential dEi(m;δm), the linear change in the functional extrapolated from m where the Fréchet derivatives were calculated to m+δm. Thus the problem is linearized by approximating δEi with dEi(m;δm). This approximation becomes exact in the limit as $\|\delta m\|_2 \longrightarrow 0$ since the functionals are continuous. Were the functionals linear in m, the addition of δm(z) to m_0, the starting model, would exactly solve the forward problem. As they are not, this addition brings the data synthesized at this new argument closer to that which was measured, hopefully within a linear regime. If this is so, the addition of the next perturbation vector which solves equation (2.1) for the resulting δEi's will solve the forward equation. Generally, three or four such linearizations are all that are needed to construct a model which fits a given set of data.

2-2 Smallest Perturbation Construction

Backus and Gilbert (1967) have shown that solutions to the perturbation equation are nonunique; infinitely many perturbation vectors δm(z) may solve equation (2.1). High frequencies, for instance, not contained in the spectrum of Gi(z) may be arbitrarily added to δm(z) without affecting the

value of the integral. Other classes of nonuniqueness are also present, most notably that introduced by the acceptable misfit to the data.

The problem now is to define criteria for choosing physically reasonable solutions for $\delta m(z)$ out of the set of possible solutions. One of these is the vector which perturbs the previous model the least at every point – the smallest perturbation vector. We will solve equation (2.1) with the vector which has the smallest norm in an L_2 sense. Thus, equation (2.1) will be satisfied and the two norm,

$$\| \delta m(z) \|_2 = \int_0^\infty \delta m(z)^2 \, dz \qquad (2.2)$$

will be minimized.

This is now a variational problem most amenable to the method of Lagrange multipliers (Backus and Gilbert, 1967). The objective functional to be minimized is formulated as follows:

$$\psi(\delta m) = \int_0^\infty \delta m(z)^2 \, dz - 2\sum_{j=1}^{n} a_j \{\delta Ej - \int_0^\infty Gj(z)\,\delta m(z)\,dz\} \qquad (2.3)$$

where the a_j ; j=1,n are the Lagrange multipliers. Then the global minimum of $\psi(\delta m)$ is obtained by finding the δm for which the differential $d\psi(\delta m;s)$ is zero for some non-zero incremental vector, s. The differential is

$$d\psi(\delta m;s) = 2\int_0^\infty \delta m(z)s\,dz - 2\sum_{j=1}^{n} a_j \int_0^\infty Gj(z)s\,dz = 0, \quad (2.4)$$

Combining the integrals we have,

$$\int_0^\infty \{\delta m(z) - \sum_{j=1}^{n} a_j Gj(z)\}s\,dz = 0. \quad (2.5)$$

Solving this with a non-zero incremental vector s, because s is arbitrary, reveals the δm which minimizes $\psi(\delta m)$.

$$\delta m(z) = \sum_{j=1}^{n} a_j Gj(z) \quad (2.6)$$

The smallest perturbation is thus a linear combination of Fréchet kernels.

Upon substituting this solution for $\delta m(z)$ into the perturbation equation, a set of n linear equations for the a coefficients is obtained.

$$\delta Ei = \sum_{j=1}^{n} a_j \int_0^\infty Gi(z)Gj(z)\,dz \quad (2.7)$$

The set of inner products formed by integrating Gi(z)Gj(z) from zero to infinity for i=1,n and j=1,n constitutes an n x n positive symmetric matrix, Γ. Some of the properties of Γ are: the eigenvalues will be real (this is known as the spectral theorem. (Shields, 1968, theorem 17)), and it is

possible to find a semi-orthogonal matrix U such that

$$\Gamma = U\Lambda U^T \tag{2.8}$$

where Λ is a diagonal matrix of the eigenvalues such that $\Lambda_{ij} = \delta_{ij}\ \lambda_i$ (Lanczos, 1961). This is called the singular value decomposition of Γ. Equation (2.7) is solved by forming the inverse of Γ which is $U\Lambda^{-1}U^T$, and multiplying it to both sides.

$$\delta E\ U\Lambda^{-1}U^T = a \tag{2.9}$$

Once the a coefficients have been obtained, the smallest perturbation vector $\delta m(z)$ is immediately available through the linear combination (2.6).

2-3 Flattest Perturbation Construction

Another geophysically reasonable solution to the perturbation equation is that which has the minimum slope or maximum flatness. Its significance is in that it produces models with gradational features; minimizing the slope leads to models with gradual changes in the resistivity structure. The perturbation having the minimum L_2 norm of its derivative is thus called the flattest perturbation.

Other criteria also exist for choosing acceptable perturbations. The second derivative may be minimized,

thereby minimizing curvature, or perturbations can be chosen using linear programming, and objective functions can be minimized with norms other than the L_2. But, since the set of perturbation vectors which will satisfy equation (2.1) is open, the choice of which criterion is used must reflect the structure expected in the final model. Within linearized construction, the flattest or smoothest perturbations should be chosen where a continuous structure is thought to exist, and where a layered structure is expected, models should be constructed with smallest perturbations. In this way, some geological considerations can be injected back into model construction.

An equation relating the derivative of the perturbation to the misfit is obtained by integrating the perturbation equation by parts.

$$\delta Ei = \delta m(z)' \, Hi(z) \Big|_0^\infty - \int_0^\infty \delta m(z)' \, Hi(z) \, dz \qquad (2.10)$$

where

$$Hi(z) = \int_0^z Gi(u)du$$

The relationship simplifies considerably upon inspecting the first term. It expresses the product of $\delta m(z)'$ and the indefinite integral of the Fréchet kernel, evaluated at the endpoints. At the zero endpoint there is no contribution, as the integral has no width, and at infinity the perturbation must be totally flat because the data contain no information at that depth. This renders $\delta m(\infty)$, and thus the term, zero. The flattest perturbation equation is then:

$$-\delta Ei = \int_0^\infty Hi(z)\delta m(z)' \, dz. \qquad (2.11)$$

Similar operations to those done in finding the smallest acceptable perturbation are now performed on equation (2.11). The two norm of $\delta m(z)'$,

$$\| \delta m(z)' \|_2 = \int_0^\infty \{\delta m(z)'\}^2 \, dz, \qquad (2.12)$$

is minimized whilst equation (2.11) provides the constraints. This objective functional, $\psi(\delta m')$ is

$$\psi(\delta m') = \int_0^\infty \delta m(z)'^2 \, dz - 2\sum_{j=1}^{n} \beta_j \{\delta Ej + \int_0^\infty \delta m(z)' Hj(z) dz\}, \qquad (2.13)$$

which, when minimized with respect to $\delta m'$, provides the means for calculating the flattest perturbation. Setting the differential to zero yields

$$\delta m(z)' = \sum_{j=1}^{n} \beta_j \, Hj(z). \qquad (2.14)$$

A matrix equation for β similar to (2.9) results when (2.14) is substituted into equation (2.11). It is solved for β also by singular value decomposition. Once $\delta m(z)'$ has been calculated via (2.14), it must be integrated to obtain the perturbation $\delta m(z)$ which is then added to the previous model.

Appendix D describes how this, and the Hi(z) indefinite integrals are computed.

Both of these methods for obtaining perturbations require the linear independence of kernel functions (Backus and Gilbert, 1967). If this is not the case, singular value decomposition will expose an eigenvalue of zero, and the set of basis vectors for producing the perturbation will be reduced. The kernels are in fact nearly linearly dependent, with those for the flattest perturbations being even more so than those for the smallest perturbation. This condition manifests itself by making the columns of the inner product matrices nearly linearly dependent too, giving rise to some very small eigenvalues.

In matrix inversion, small eigenvalues can create large difficulties. They are often at the limit of machine resolution, and are therefore numerically inaccurate, but their influence is great because their reciprocals are involved in obtaining the α or β coefficients (equation 2.9). Again, this problem more severely effects the flattest perturbations and the way it is dealt with, which is to delete the small eigenvalues, generally reduces the size of the perturbation – sometimes to the point of preventing convergence. The method for dealing with small eigenvalues, and their relationship to data errors is developed in the following section.

2-4 Errors and their Influence

Potential difference measurements contain errors and information. Errors play an important role in linearized

construction. Not only do they dictate what degree of misfit is justifiable between the measured and computed data, but they are also used to winnow out the small eigenvalues.

2-4.1 Sources of Error

The sources of error in the data are manifold. Although the method is known as D.C. resistivity, the current which produces the electric field is a square wave with a period sufficiently long that induction effects have ceased well before the switch in polarity occurs. Ideally, the potential record is a square wave too, having its leading edges rounded by induction, and the actual potential measurement is the wave amplitude. Records however are usually tainted with noise of both instrumental and geophysical origins. All instruments whether digital, or analogue, have their own internal noise which is superimposed upon the incoming signal. Although the noise level is small, it can affect low level readings such as those taken at very large electrode spacings.

Of greater influence though, is the geophysical noise from telluric currents. Since they flow continually, the potential electrodes will always pick up some level of telluric noise, and removing it can present some difficulty because of its broad bandwidth. Periods range from 0.1 second, to 1000 seconds. The high frequency tellurics simply add high frequency noise to the record but the lower frequencies add time varying biases, the effects of which increase with potential electrode separation and in severe cases can destroy the square wave response. This is not

usually a problem in Schlumberger soundings, but it can be in pole-pole and large dipole-dipole experiments where the electrode separations may be tens or hundreds of kilometers. On-line computers have been used to calculate the stable D.C. potential.

Invalidity of the physical simplifications made to solve the forward equation is another source of error, and as such will add to the degree of misfit which must be expected of an acceptable model. These simplifications will be examined. They were:

1. The earth is flat.
2. The resistivity structure varies with depth only.
3. Resistivity structure is layered.
4. Layers are isotropic.

The curvature of the earth is unlikely to cause significant errors in calculating potentials for any experiments done to date, but the topography effect can be significant. Even if electrodes are at the same elevation, errors will be introduced if the earth's surface is not flat in the vicinity. These errors are usually not debilitating however, if they are correctly estimated and included in the total error estimate for each datum. The data successfully inverted in Chapter 3 attest to this fact, as they were taken in extremely mountainous terrain.

Assuming that the earth's structure varies with depth only is the most frequently made approximation in geophysics, with its validity depending upon where it is made. Over sedimentary structures it is often quite correct to assume

there is no lateral variation, but in igneous and metamorphic environments this simplification may be quite erroneous. Faults and vertical contacts, both of which are present in the region where data in Chapter 3 were taken, also violate the one-dimensional assumption so the data error estimates must be increased in such regions to allow a one-dimensional model to converge.

The approximation that the one-dimensional structure is layered was made to facilitate calculation of the potential equation kernel and the Fréchet kernels. Since the accuracy of this depends upon the fineness of the layering scheme, errors can be made negligible by having many layers. At present, the construction program has a capacity for seventy-five layers.

Sedimentary layers, particularly those which have undergone some metamorphism, often conduct electricity more readily parallel to the layering than perpendicular to it. It is common for the perpendicular resistivity to be four or five times greater than that parallel to the layering (Maillet, 1947, p. 530). Using the method of Dar Zarrouk parameters, apparent resistivity curves may be calculated over such strata provided the anisotropy is known. As our construction method does not deal with layer anisotropies, models constructed over such structures will have layer resistivities somewhere in between the two. The layer boundries will be correctly placed, however the absolute resistivities will be incorrect. Additional misfit tolerence may be neccessary to account for anisotropy when constructing models over such a medium.

2-4.2 How Errors are Accomodated by the Construction Method

If the approximations made in formulating this problem are valid, and the potential measurements are completely accurate, then the perturbation equations could be solved exactly, and an acceptable model would be constructed in a few iterations. However, neither of these conditions are ever met. Errors in the measurements and errors in our idealizations must therefore be accomodated by the construction algorithm.

Sets of linear equations are especially sensitive to errors. Small errors in the data affect the inner product matrix, and would cause large errors in the α or β coefficients, were the equations solved exactly. The approach taken here is to assume that errors arise from random processes with Gaussian distributions and zero means. The one standard deviation level for each measurement is ascertained, and is used in determining the chi-squared misfit to the data which measures global convergence.

Each datum is divided by its corresponding standard deviation, thereby normalizing the standard deviations to unity. If a measured value is within one standard deviation of the true value,

$$\text{then} \qquad \begin{aligned} Ei(meas) &= Ei(true) \pm \sigma \\ \frac{Ei(meas)}{\sigma_i} &= \frac{Ei(true)}{\sigma_i} \pm 1 \end{aligned} \tag{2.15}$$

The normalized i'th datum will be written as $\hat{E}i$. To maintain equality, the potential kernels and the Fréchet kernels are

also divided by the appropriate standard deviations. Thus the normalized forward, and perturbation equations are:

$$\hat{E}i = \int_0^\infty \rho_0 \frac{\lambda S(0,\lambda) Ci(\lambda)}{\sigma_i} d\lambda \qquad (2.16a)$$

$$\delta\hat{E}i = \int_0^\infty \frac{Gi(z)\delta m(z)}{\sigma_i} dz. \qquad (2.16b)$$

Normalizing the Fréchet kernels also changes the matrix equation for coefficients.

$$\delta\hat{E}i = \sum_{j=1}^{n} a_j \sigma_j \int_0^\infty \frac{Gi(z)Gj(z)}{\sigma_i \quad \sigma_j} dz \qquad (2.16c)$$

Computationally, normalizing the standard deviations is one of the first operations performed. Normalized data are compared for the misfit; normalized Fréchet kernels are integrated to form the inner product matrix, and normalized misfits are used to compute the α or β coeffients. In short, normalized quantities are used throughout the construction operation.

The chi-squared statistic for the misfit to the data is given by the following:

$$\chi^2 = \sum_{i=1}^{n} \left| \frac{Ei(meas) - Ei(calc)}{\sigma_i} \right|^2 \qquad (2.17a)$$

which for normalized data is:

$$\chi^2 = \sum_{i=1}^{n} |\hat{E}i(meas) - \hat{E}i(calc)|^2. \qquad (2.17b)$$

Chi-squared will equal n, the number of data, when the L_2 average of the normalized misfits is down to unity. This

constitutes chi-squared global convergence and iteration is stopped when it is attained.

The chi-squared criterion is also used in solving the matrix equations for a and β. Since the misfit to the i'th datum also has a standard deviation of σ_i, solving the matrix equation any more exactly than this is unjustifiable. Thus the chi-squared misfit between vectors $\delta\hat{E}$ and $\hat{\Gamma}a \cdot \sigma$ must also be approximately n.

$$\sum_{i=1}^{n} (\delta\hat{E}_i - \hat{\Gamma}_{ij}\, a_j\, \sigma_j)^2 \leq n. \qquad (2.18)$$

A solution with this degree of misfit is obtained by winnowing eigenvalues from smallest to largest until the desired misfit is attained. Winnowing progresses in this direction because the smallest eigenvalues are often at or beyond the limit of machine resolution, and are therefore inaccurate. Their influence however, can be very large because their reciprocals are used to obtain the a coefficients. In the singular value decomposition form of the matrix, winnowing corresponds to decreasing the rank of Λ, the diagonal matrix of eigenvalues, and decreasing the number of columns in U. The following equation codifies the normalized solution with n minus m eigenvalues winnowed.

$$\underset{(n,1)}{a \cdot \sigma} = \underset{(n,m)}{U}\ \underset{(m,m)}{\Lambda^{-1}}\ \underset{(m,n)}{U^T}\ \underset{(n,1)}{\delta\hat{E}} \qquad (2.19)$$

This is called the truncated solution, and chi-squared

measures the difference between the truncated data misfits which it determines and $\delta\hat{E}i$.

$$\sum_{i=1}^{n} \{\delta\hat{E}i - \delta\hat{E}i^{\dagger}\}^2 = \chi^2 \qquad (2.20)$$

Determining the number of eigenvalues to winnow is most efficiently done in the rotated misfit space. The misfit vector, $\delta\hat{E}$ is rotated by U^T, and its elements are squared and summed backwards, from n to 1. The maximum number of rotated misfits that can be summed in this direction until the value of n is reached is ℓ, the number of eigenvalues which will be winnowed. Then, the difference between n and ℓ is m, the number of eigenvalues which will be kept. (The algebreic justification for this is given in Appendix E)

$$\sum_{i=n}^{m+\ell} \delta\hat{E}rot_i^2 \leq n, \qquad (2.21)$$

where $\delta\hat{E}rot = U^T\delta\hat{E}$.

The first m rotated misfits are divided by their associated eigenvalues,

$$\underset{(m,m)}{\Lambda^{-1}} \quad \underset{(m,1)}{\delta\hat{E}rot}, \qquad (2.22)$$

then rotated back to the initial frame by U and divided by their standard deviations to obtain the chi-squared acceptable coefficients. These coefficients, which most closely satisfy

the equality condition in equation (2.18) while erring towards the inequality, are the ones used to construct the perturbation.

2-4.3 Final Considerations Regarding Perturbations

Empirically, it has been found that this raw perturbation, although it satisfies the perturbation equation, is not necessarily the best one to add to the previous model. Through solving the M-T and D.C. resistivity problems, a sequence of operations which are applied to the raw perturbation before it is added to the model has evolved. This procedure seems to produce the best perturbations possible for guiding a model towards convergence (Oldenburg, 1979, 1978, and personal communication). The 'recipe' has no real mathematical justification – it just works. A perturbation is operated on when it shows large amplitudes or high frequency oscillations, both of which are usually detrimental to the construction of a physically realistic model.

It must be remembered that the approximation which makes the perturbation equation solvable is that $\delta Ei \simeq dEi(m, \delta m)$, and when δm is large this is likely invalid. It is therefore reasonable to limit the maximum perturbation allowed in a single iteration, at the cost of possibly reducing the chi-squared misfit more slowly. A maximum absolute value of 1.4 for $\delta m(z)$, which can increase or decrease the resistivity by a factor of four, has worked well in both flattest and smoothest constructions. This is implimented by truncating any larger

or smaller values of $\delta m(z)$ at that level.

Less frequently, $\delta m(z)$ has some very large values which not only invalidate the linearization approximation, but would invariably preclude convergence if they were applied. When the perturbation is anywhere greater than 5.0, another eigenvalue is winnowed and new coefficients are computed. As these coefficients solve the misfit equation less closely, the ensuing perturbations are most often smaller. This summarizes the treatment of large amplitude features, but the frequency characteristics are important as well.

Since construction usually starts from a half-space, it must first shape the general structure of the model, and then add finer scale details for a realistic earth model. While it may be possible to fit resistivity data with a delta-function-like model as Parker (1981) has done for M-T, this is undesirable for comparison with the real earth. Instead, large scale features are desired as they are likely more resolvable (see Chapter 4), and most resistivity interpretations centre around trends rather than glitches. For these reasons, the high frequency content of a perturbation is suppressed until the model is fairly close to chi-squared convergence. This is done by convolving the perturbation with a triangular smoothing window. In this construction program, as in that of Oldenburg (1978) the extent to which the high frequencies are suppressed is proportional to the maximum perturbation. The smoothing function is passed through the perturbation a number of times equal to the integer value of the largest perturbation – up to

a limit of three. Thus, a perturbation vector having no elements larger than one will remain unsmoothed. Fine scale features of this low an amplitude are neccessary in the last stages of construction to bring the chi-squared down to statistical convergence. The following figure summarizes the treatment of a perturbation vector prior to applying it to a model.

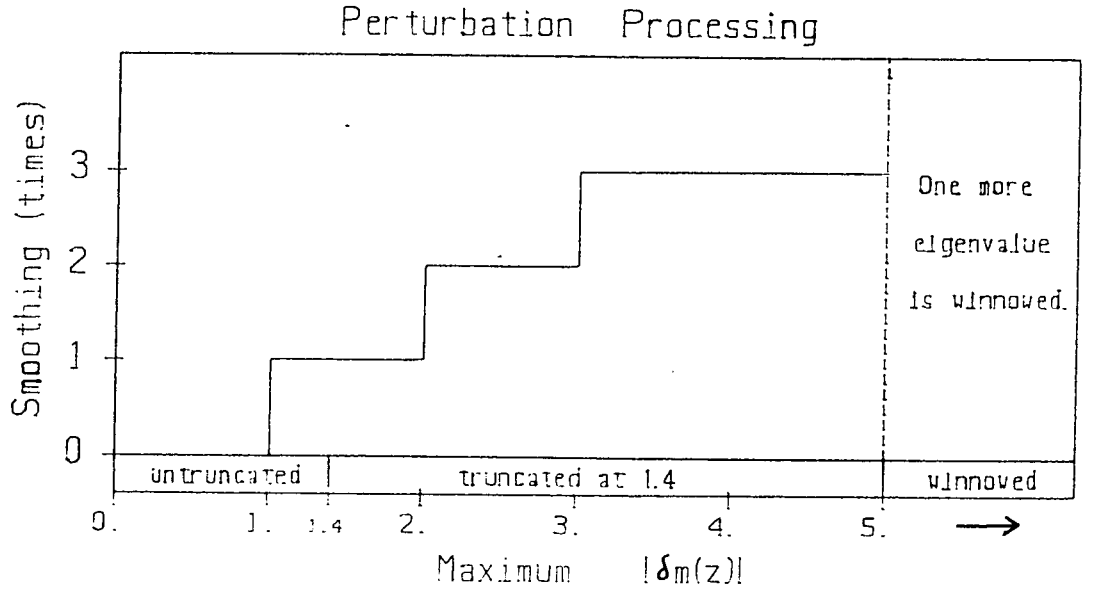

Figure 2.1 Depending upon the size of the largest element in a perturbation vector, it may be smoothed, truncated, or both. A vector having an element larger than 5 is not acceptable, and is recomputed with one more eigenvalue winnowed. Any elements having an absolute value greater than 1.4 are truncated at that level, then smoothed, with the number of times a perturbation is smoothed depending upon its largest value. The number of times a smoothing filter is passed over the truncated vector is equal to the integer value of the largest element prior to truncation.

2-5 Computing Hankel Transforms

The single most important improvement in this linearized construction program over the original is that the Hankel transforms are now computed more efficiently using the digital filter technique of Gosh (1971), rather than being integrated numerically. Not only were they difficult to compute as integrals, but since solving the forward equations requires performing four per datum as does evaluating each Fréchet kernel, Gi(z) at every depth, the difficulty quickly multiplies. For twenty data, and a good layering scheme, hundreds of Hankel transforms must be performed per iteration.

number of transforms = 4 x (no. of data + 2(no. of layers))

eg. 480 transforms = 4 x (20 data + 2(50 layers))

In addition to there being hundreds to compute, they must be accurate because the four that are added and subtracted per datum or Fréchet kernel are numerically very close. Fortuately, both speed and accuracy are attributes of the filter technique. Using it, Hankel transforms are accurately computed in less time than a numerical integration routine would require. Moreover, they are computed only once for the range of arguments, and spline-fit wherever needed reducing the CPU time for each iteration further. Now, that models can be constructed more efficiently, linearized construction is a quick and practical way of interpreting resistivity measurements.

Computing integrals of Bessel functions by convolving the kernel with a set of filter weights was first introduced by Gosh in 1971. Since then, other workers have improved the accuracy of the weights, and designed filters for specific problems in resistivity and E-M work. Anderson's 1979 paper summarizes the development to date and includes a computer program containing the most accurate set of weights in the literature (Anderson, 1979). His program performs Hankel transforms of orders zero and one, and contains 283 point filters for each transform. The filter weights have seven figure accuracy, and half-space potentials computed with them agreed with the exact values to four or five decimal places. The formulation of the filter method and our exact tailoring of it will be developed here.

The general form of a zeroth order Hankel transform is

$$K(r) = \int_0^\infty k(\lambda)\, J_0(\lambda r)\, d\lambda \qquad (2.23)$$

where $k(\lambda)$ is the transform kernel, and r is the transform argument.

At the distance r from a current source I, the expression for the potential is

$$V(r) = \frac{-I\rho_0}{2\pi} \int_0^\infty \frac{\lambda H(0,\lambda)}{H'(0,\lambda)}\, J_0(\lambda r)\, d\lambda \qquad (2.24a)$$

and the Fréchet kernel at the depth z for a single source is given by

$$G(z,r) = \frac{\rho_0}{2\rho(z)} \int_0^{\infty} \lambda \left[\frac{\lambda^2 H(z,\lambda)^2 + H'(z,\lambda)^2}{H'(0,\lambda)^2} \right] J_0(\lambda r)\, d\lambda \qquad (2.24b)$$

Both of these are Hankel transforms and can be transformed into convolution integrals by applying the following change of variables, (Gosh,1971)

$$\begin{aligned} r &= \exp(x) & x &= \ln(r) \\ \lambda &= \exp(-y) & y &= \ln(1/\lambda) \\ d\lambda &= -\exp(-y)dy \end{aligned}$$

and multiplying the Hankel transform by exp(x). Now,

$$e^{x} K(e^{x}) = \int_{\infty}^{-\infty} -k(e^{-y})\, J_0(e^{x-y}) e^{x-y}\, dy \qquad (2.25)$$

and the limits become: $\lambda = 0 \longrightarrow y = \infty$
$\lambda = \infty \longrightarrow y = -\infty$

Finally the direction of the integral needs to be reversed by changing the sign of the integral. This is now a convolution integral in log space and may be written as

$$e^{x} K(e^{x}) = k(e^{y}) * J_0(e^{x}) e^{x} \qquad (2.26)$$

where $k(e^{y})$ is the input, $J_0(e^{x})e^{x}$ is the filter, and $e^{x} K(e^{x})$ is the output (Anderson,1979). The change of variables is done automatically in Anderson's program. Computing Hankel transforms in this way requires knowing the filter, and Anderson has computed the filters by taking analytic Hankel

transform pairs and deconvolving them. He found that the most accutate filters were obtained from transforms having rapidly decreasing kernels and output functions. The zeroth order pair

$$\frac{\exp(-r^2/4)}{2} \longleftrightarrow \lambda\exp(-\lambda^2)$$

meets this condition, and was used for the zeroth order filter.

The steps involved in computing the filters are outlined below.

1. Both functions have the change of variables applied to them and are digitized at a constant sampling interval in natural log space; $\Delta=.2$ was used. This corresponds to taking samples at orders of 1.221 on a linear scale.
2. The Discrete Fourier transforms of both functions are computed, and that of the output function is divided by that of the input. Fourier transform deconvolution is the most highly resolved deconvolution method when both signals are known.
3. Multiplying the deconvolved spectrum by the spectrum of the sampling sinc function removes the spectra repeated at $1/\Delta y$ intervals whilst preserving the filter frequencies from the negative to positive Nyquist. Had a continuous Fourier transform been obtained, this step would be unneccessary.
4. The spectrum is then inverse Fourier transformed providing the filter weights. They are the sinc response

of the filter, rather than the impulse response because the functions were sampled at finite intervals.

Once the filter weights have been obtained, the zeroth order Hankel transform of k(r) may be evaluated by convolving it with the filter weights, both with the change of variables applied. For the continuous case this would be:

$$K(r) = \frac{1}{r} \int_{-\infty}^{\infty} k(e^{-y}) \, W(e^{\ln(r)-y}) \, dy \qquad (2.27)$$

but since this is a digital filter,

$$K(r) = \frac{1}{r} \sum_{i=1}^{283} k(e^{-y_i}) \, W(e^{\ln(r)-y_i}) \, \Delta y \qquad (2.28)$$

One can see that as the argument becomes larger, the filter is displaced to the left with respect to the kernel; therefore, to keep full utilization of the filter, the kernel must extend as far left as the filter will be displaced. Every factor of 1.221 increase in r shifts the filter left by another increment, and similarly arguements smaller than 1.0 will shift the weights right.

By changing the arguments so that the kernel is now shifted to the right over the weights, and returning to our original variables, the filtering operation becomes a cross correlation between the shifted kernel and filter weights.

$$K(r) = \frac{1}{r} \sum_{i=1}^{283} k(\lambda_i / r) \, W(\lambda_i) \qquad (2.29)$$

λ is given by $.735 \times 1.221^{i-130}$

Thus the endpoints of the filter stretch from .735 x 1.221^{-127} to .735 x 1.221^{153}, instead of from 0 to ∞ allowing the filter to give an accurate value for the transform, provided the kernel has decayed to zero well inside the endpoints and is not highly oscillatory. With this equation and Anderson's weights, the zeroth order Hankel transform of any such kernel can be easily and accurately computed.

In our application, the Hankel transforms of just one kernel for the computed data, and two at each layer boundary for the Fréchet kernels are required per iteration, for all the arguments r. They could be computed separately for each transform argument by re-evaluating the kernel at the 283 new points λ_i / r implied by every new r, and this would certainly provide the accuracy afforded by the filter method, but little or no savings of time would be realized. Each transform would require 283 kernel function evaluations and the summation of 283 kernel-filter products. This would have to be done for every kernel at each argument.

To make full use of the time savings possible, another implication of the analogy with convolution is used. If the filter and kernel were available in their continuous forms, the most efficient way of obtaining K(r) would be to do the cross correlation by multiplying the conjugates of the continuous spectra, and inverse Fourier transforming. Then K(r) would be available for any r.

This is approximately what is done. The kernel is evaluated at intervals of 0.2 in natural log space over the entire range in which it will be needed. That is from two

intervals left of λ_1/rmax to two intervals right of λ_{203}/rmin. Then the cross correlation is carried out in frequency domain and, upon inverse transforming, the Hankel transforms $K(r_j)$ are available; $r_j = \text{rmax}(1.221)^{1-j}$. In the zero lag position is the Hankel transform with the largest argument, and at subsequent greater lags are Hankel transforms with arguments successively smaller by factors of 1.221. Hankel transforms of all the arguments needed are then picked off the spline-fit $K(r_j)$ function, and combined to form the computed data or Fréchet kernels.

With this method, the number of full cross correlations calculated is two per layer plus one to compute the data. Thus, the computer time is proportional to the number of depths at which the Fréchet kernels are evaluated, but independent of the number of data.

2-6 Testing the Linearized Construction Program

Immediately upon programming a method for analyzing data, the performance and limitations must be found. One hopes that the program will not limit the method's capabilities, and further, that any conditions placed upon the data, in terms of quality and sample density, will not be so restrictive that most of the pre-existing data is unsuitable. Also, in testing an inversion program, such as linearized construction for resistivity models, the degree to which nonuniqueness can affect models is partially qualified by comparing models constructed from synthetic data to those from which the data was derived.

2-6.1 Objectives

There are three main objectives in testing this program.

1. The limitations of the program must be found; the extent to which a starting model affects the final model must be determined. More specifically, can the program converge upon a model representative of the true structure when iteration starts from a poorly chosen half-space?

2. Limitations on the data will be investigated by adding noise to a synthetic data set to see how a model will deteriorate with increasing errors in the data. The effects data spacing has on resolving the resistivity structure will also be investigated.

3. In both of the preceeding experiments, the differences between synthetic and constructed models will be taken as illustrations of nonuniqueness. If there is little resemblence between the two, then there is little to be gained from constructing models. Some widely different theoretical models will also be used in an attempt to catalogue the constructed models signatures of particular structures. In this way, some intuition can be acquired about what a constructed model is saying about the underlying structure. Less intuition is needed here than in other methods of interpreting resistivity data, such as apparent resistivity curves or pseudo-sections, but some understanding can certainly be gained from this comparison.

2-6.2 Effects of the Starting Model

As mentioned earlier in this chapter, the starting model

should be carefully chosen. It is evident that a model will be more easily constructed from a starting model that lies comfortably within the range of apparent resistivities, than one outside that range, but the specific effects a poor choice has on the final model should be known. Then, the starting model could be adjusted when the effects are recognized. Another aim of this experiment is to develop some intuition on choosing the best starting model from an apparent resistivity curve.

A sixteen layered structure was the hypothetical model and twenty Schlumberger data with AB/2 ranging from 5 to 3620 meters were synthesized from it. A nominal standard deviation of 0.5 percent was assigned to each datum for normalization purposes, although the data were accurate. The expansion factor for AB/2 was 1.41, the square root of 2, with the potential electrode separation was always one tenth that of the current electrodes.

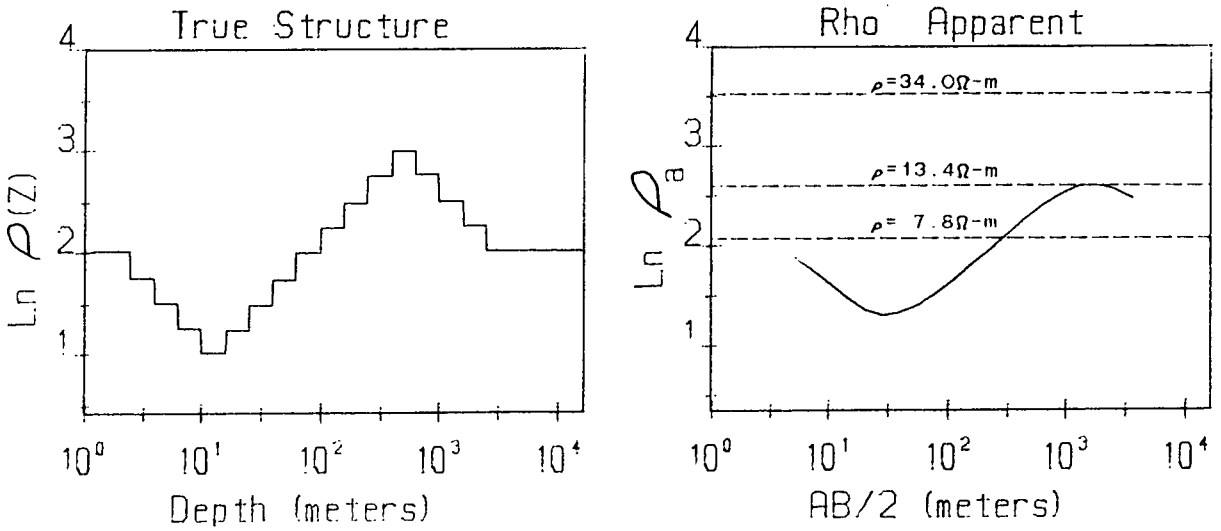

Figure 2.2 On the left, the resistivity structure used to synthesize the data for this experiment is shown. The mean value is 7.39 ohm-meters.. Twenty Schlumberger data were computed, and the resulting apparent resistivity curve is shown on the right. The horizontal dashed lines represent half-spaces of constant resistivity which were used as starting models. The models constructed from these are compared to identify the starting model's effect.

The true structure and apparent resistivity curve are shown in figure 2.2 with three different choices of starting models.

For the top 2.5 meters, the resistivity is 7.39 ohm-meters then it drops to 2.7 at 10 meters, and increases to 22 ohm-meters by 500 meters before dropping back down to the original value of 7.39 ohm-meters for the underlying half space. Constructions were done using first the smallest perturbations, then the flattest, with all the constructed models having 73 layers.

From the apparent resistivity curve, a half space of resistivity equal to exp(2.05) seems the best and most obvious choice for a good starting model. This is 7.8 ohm-meters, and from it a model was converged upon in three iterations. Below a depth of 12 meters, the constructed model matches the true structure very well, while above, it has under estimated the low resistivity layer, and compensated by increasing the resistivity just above and below that region.

Overleaf:

Figure 2.3 In three iterations, a model is constructed from the twenty Schlumberger data which reproduces the true structure very well. Starting from a half space of 7.8 ohm-meters, smallest perturbations are used to improve the preceding model and reduce the misfit to the computed data. The final model satisfies the chi-squarred criterion. The misfit at each iteration is given below.

	RMS relative misfit	Chi squared
starting model	59.7%	2.84×10^5
first iteration	12.5%	1.24×10^4
second iteration	1.1%	9.18×10^1
third iteration	0.3%	9.27

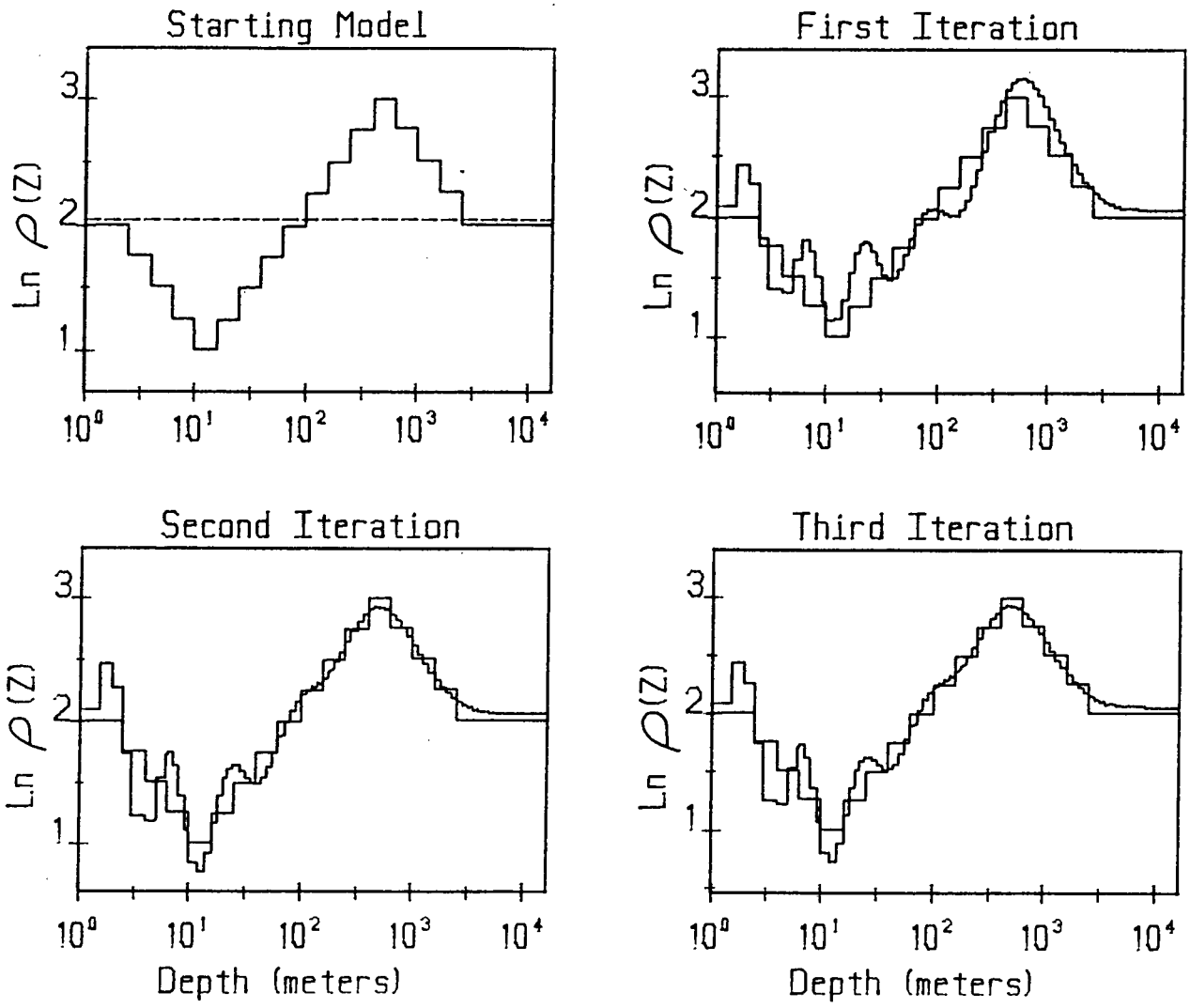

When the starting resistivity is increased to the maximum on the apparent resistivity curve, 13.4 ohm-meters, one more iteration is required to produce an acceptable model. This increase is characterized by higher frequency models at every iteration. In this construction, the decreasing ability of the Fréchet kernels to affect perturbations below a certain depth is seen. As $z \longrightarrow \infty$ the kernels decay to zero, and so must the perturbation vector since they are its basis functions (see equation 2.6). Hense, the illusion of an increase in resitivity is created in a region where the constructed model contains no reliable information.

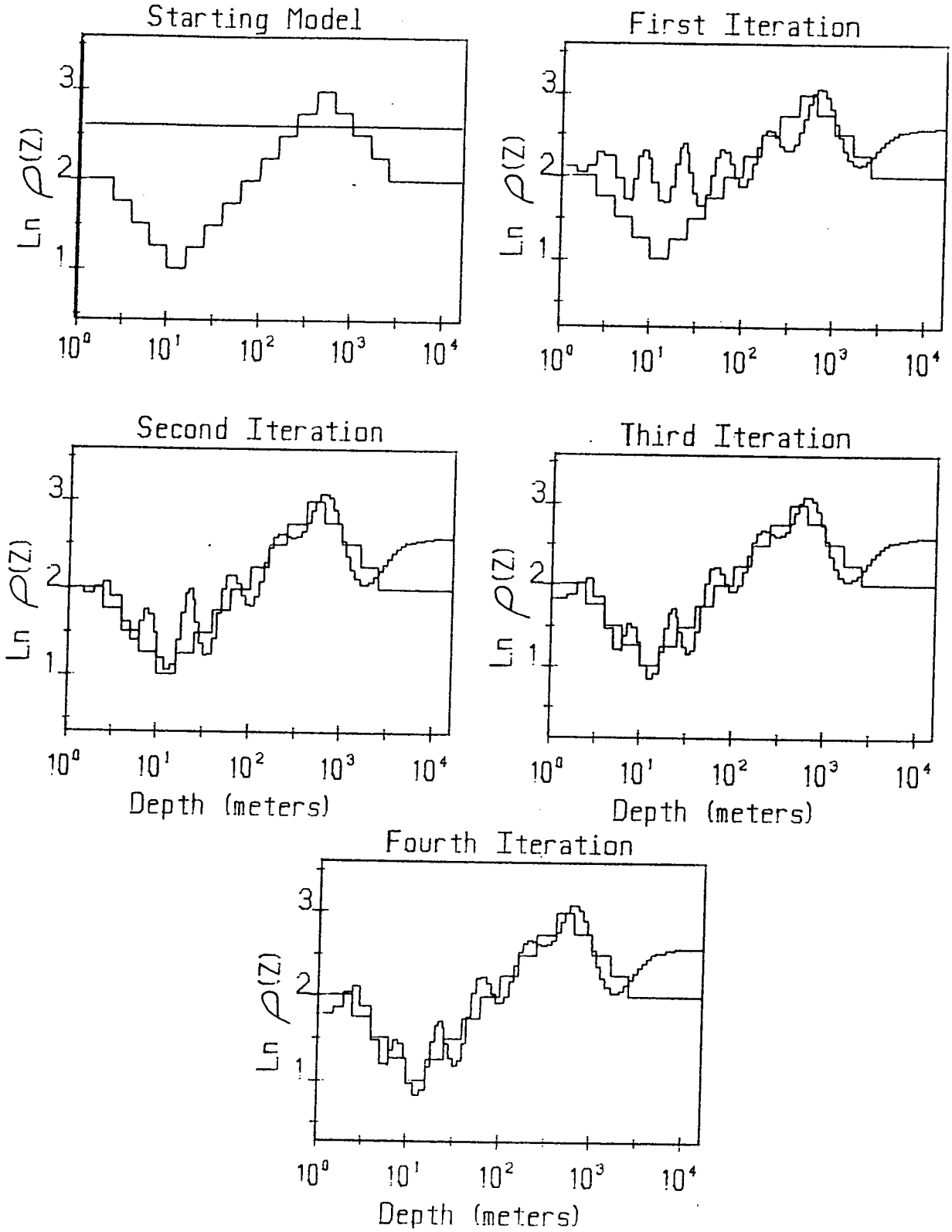

Figure 2.4 When construction starts from a half-space of 13.4 ohm-meters, one more iteration is needed to converge upon an acceptable model in the chi-squared sense. This model is slightly more oscillatory than that started from 7.8 ohm-meters, but is still a very good represintation of the true structure. The apparent increase in resistivity below 1000 meters is an artifact of the starting model, and the the construction method. It signifies loss of resolution.

Increasing the starting resistivity to 34 ohm-meters, far outside the range of apparent resistivities, results in the following construction (figure 2.5). After five iterations the model fits the data, and reproduces the true structure very well. It is no more spikey in the region from 1 to 10 meters than the construction which started from 7.8 ohm-meters, and from 10 to 500 meters it overlies the true structure exactly. It falls away from the true structure at 1000 meters depth, however, and is the least representative model in that region.

Varying the starting models over the range investigated has had very little effect on the models constructed. In fact, the construction which was started from the worst starting model fit the true structure most closely down to about 1000 metes, where the kernels begin to loose their resolving power. Below the depth where this happens, the models started from 13.4 and 34 ohm-meters falls away from the true structure more than the first construction (figure 2.3). However, this is dependent upon the difference between the starting model and the true structure at those depths, not just upon the starting model. Since the same physical interpretations would likely be drawn from any of these three models, we can say that the model constructed is fairly independent of the starting model. More iterations are required though, when the starting model is poorly chosen.

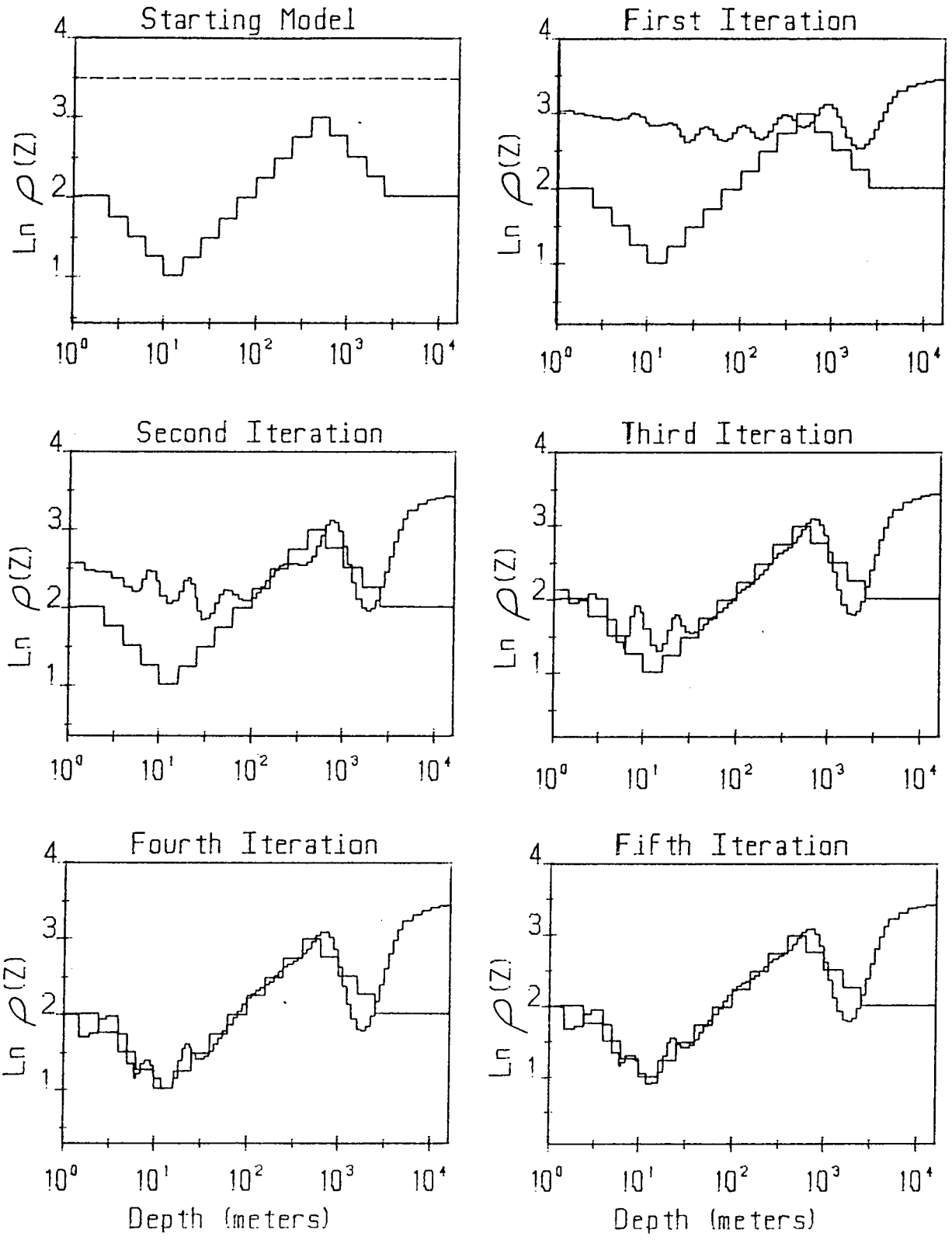

Figure 2.5 Construction started from a half-space of 34 ohm-meters. In this test a model representative of the true structure down to 1000 meters was constructed in five iterations. In the range from 1 to 1000 meters, it is as good or better than the two previous models. Varying the starting model did not cause any noticable deterioration of the final models.

Flattest perturbation constructions are more sensitive to the choice of starting models. The perturbation is the indefinite integral of $\delta m'(z)$ and as the resistivity is more likely to be known at the surface than at depth, $\delta m'(z)$ is integrated from z=0 to the maximum depth with the integration constant set to zero (see equation 2.14 and Appendix D).

$$\delta m(z) = \int_0^z \delta m'(u)\, du \qquad (2.30)$$

Since the integral is zero at the surface, and remains small at shallow depths, a large change in the starting model is impossible there. Unless the starting model is very close to the true structure at shallow depths, the perturbations will compensate for this at greater depths, and an unrepresentative model will be constructed.

The first construction with flattest perturbations was started from a half space of 7.8 ohm-meters, the best choice from the apparent resistivity curve, and a model very representative of the true structure was constructed in three iterations. At shallow depths, the constructed resistivity matches the true structure even more closely than the smallest perturbation constructions did, and at all depths from 1 to 1000 meters, it overlies the true structure. It must be remembered, that although the construction is layered, it is an approximation to a continuous resistivity distribution, and not an attempt to parameterize the resistivity structure. Therefore the constructed model is not expected to reproduce the stepped nature of the true structure.

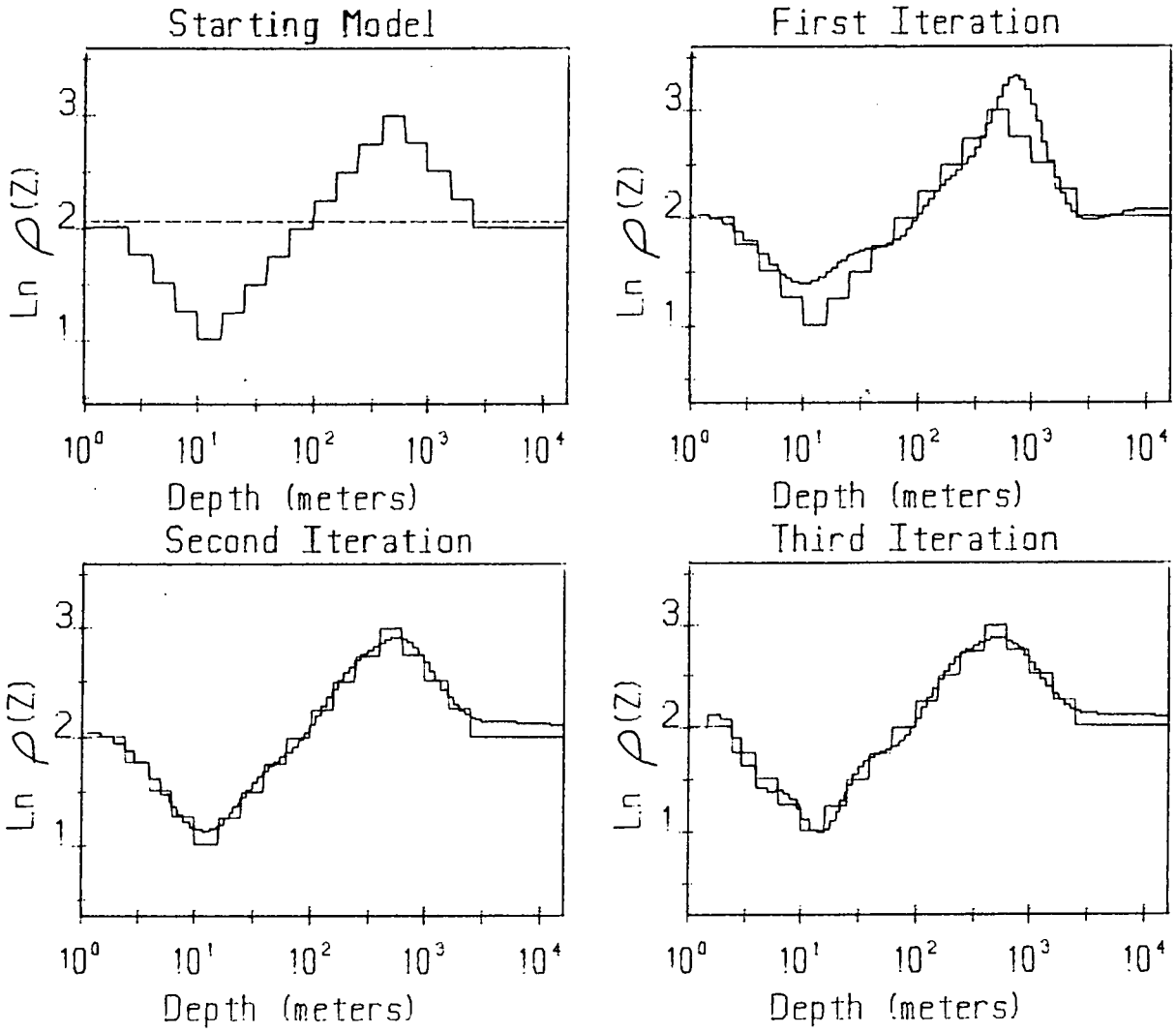

Figure 2.6 Perturbing the starting model of 7.8 ohm-meters with the flattest perturbations yields the above model. At shallow depths it overlays the true structure more closely than the corresponding smallest perturbation construction (figure 2.3), and at all depths from 1 to 2000 meters the fit to the true structure is very good. When the near surface resistivity is known, and used as the starting model, the flattest perturbations construct a smoothly varying model.

Increasing the starting resistivity to 13.4 ohm-meters prevents the construction of a representative model because of the inherent limitation in the flattest perturbations. The perturbations are not large enough at shallow depths to bring

the model down to the true structure, and chi-squared convergence was not attained here. This constructed model can only trace the structure of the theoretical model with a resistivity bias equal to the difference between the starting model and the shallow resistivity. Therefore, when constructing a model with flattest perturbations it is crucial that iteration is started from the near surface resistivity value. If this is not done, an acceptable model will not be found, and construction will be to no avail.

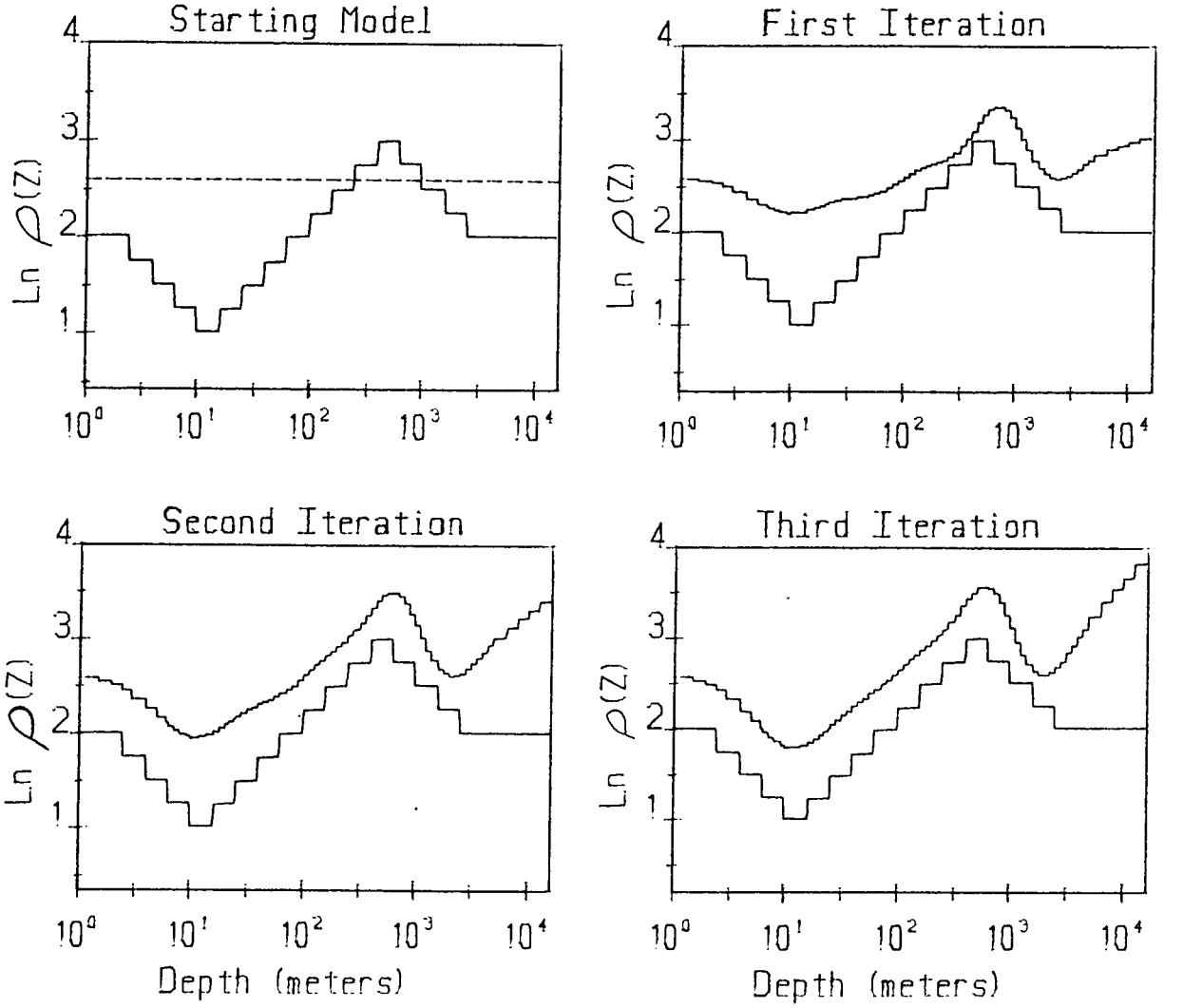

Figure 2.7 The limitations in constructing models using the flattest perturbation are clearly shown in this figure. The starting model was 13.4 ohm-meters, and they are insufficient to bring the model down to the true structure. Instead, it simply traces the true structure, keeping a mean value of 13.4 ohm-meters. The final up-swing is a result of the allowable misfit in the perturbation equation.

An automatic starting model selector has been investigated for the flattest perturbations. It sets the starting model to a half-space of the shallowest apparent resistivity value. If the resistivity structure is constant from the surface down to a depth comparable to the AB/2 spacing of this reading, a very good starting model is chosen, but when there is a resistivity variation of more than a factor of two, the automatic selector hinders construction. In environments where the resistivity varies greatly with depth, the flattest perturbations will not construct a very representative model with any starting model. Smoothly varying structures are certainly their forté.

In the data being used, the shallowest sounding has an AB/2 spacing of 5 meters, and an apparent resistivity of 6.44 ohm meters. When this is selected automatically for the starting model, the following construction results.

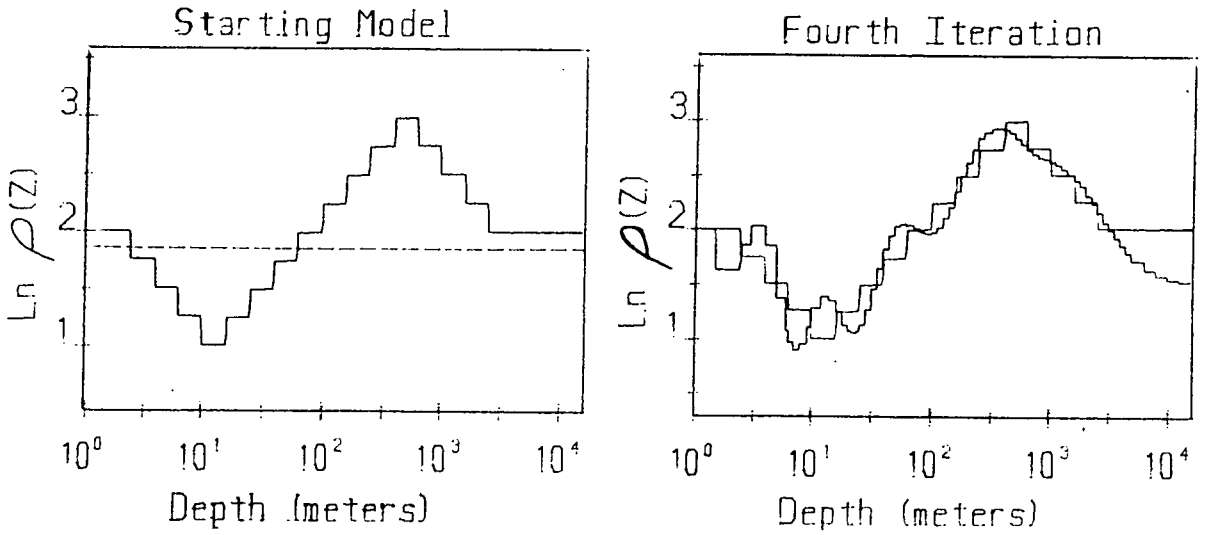

Figure 2.8 Using the shallowest apparent resistivity as a starting model, it was difficult to construct a data-fitting model. The last two iterations were made using the smallest perturbations. Had this not been done, the model would not have converged. Their extreme sensitivity to starting models makes flattest perturbations impractical for general use, but used for the first, or first two iterations, their influence is noticeable, and the model converges.

2-6.3 The Effects of Noise and Data Density

There are two aspects to data quality: accuracy, and sample density. The degree to which each of these independently affects the construction of a representative model should be known. Accurate data is that which contains no errors, from either geophysical or instrumental sources. There are no effects from lateral inhomogeneities, no human errors, and no noise in accurate data. The other aspect, data density, refers to how well the electric field has been sampled with potential measurements. In a Schlumberger sounding, data density is quantified by the expansion factor. The closer it is to one, the higher the data density; 1.41 is often used, and has been shown by Oldenburg (1979) to afford good resolution.

In the first experiment, noise is added to the data in the form of random numbers. Their mean is zero and their standard deviation is one. They are scaled by the percent noise level being tested, then multiplied by the data to give the noise error ϵ_i.

$$\epsilon_i = \text{Xi} \ \frac{\text{level}}{100\%} \ \text{Ei} \qquad (2.31)$$

Xi is the random number

This is added to the i'th datum, and the standard deviation is taken as

$$\sigma_i = \frac{\text{level}}{100\%} \ \text{Ei} \qquad (2.32)$$

Noise levels of 3,5,10, and 20 percent were tried. The

minimum error in a potential difference measurement is realistically about 3 percent. With these four noise levels added to the data, the following final models were constructed with the smallest perturbations.

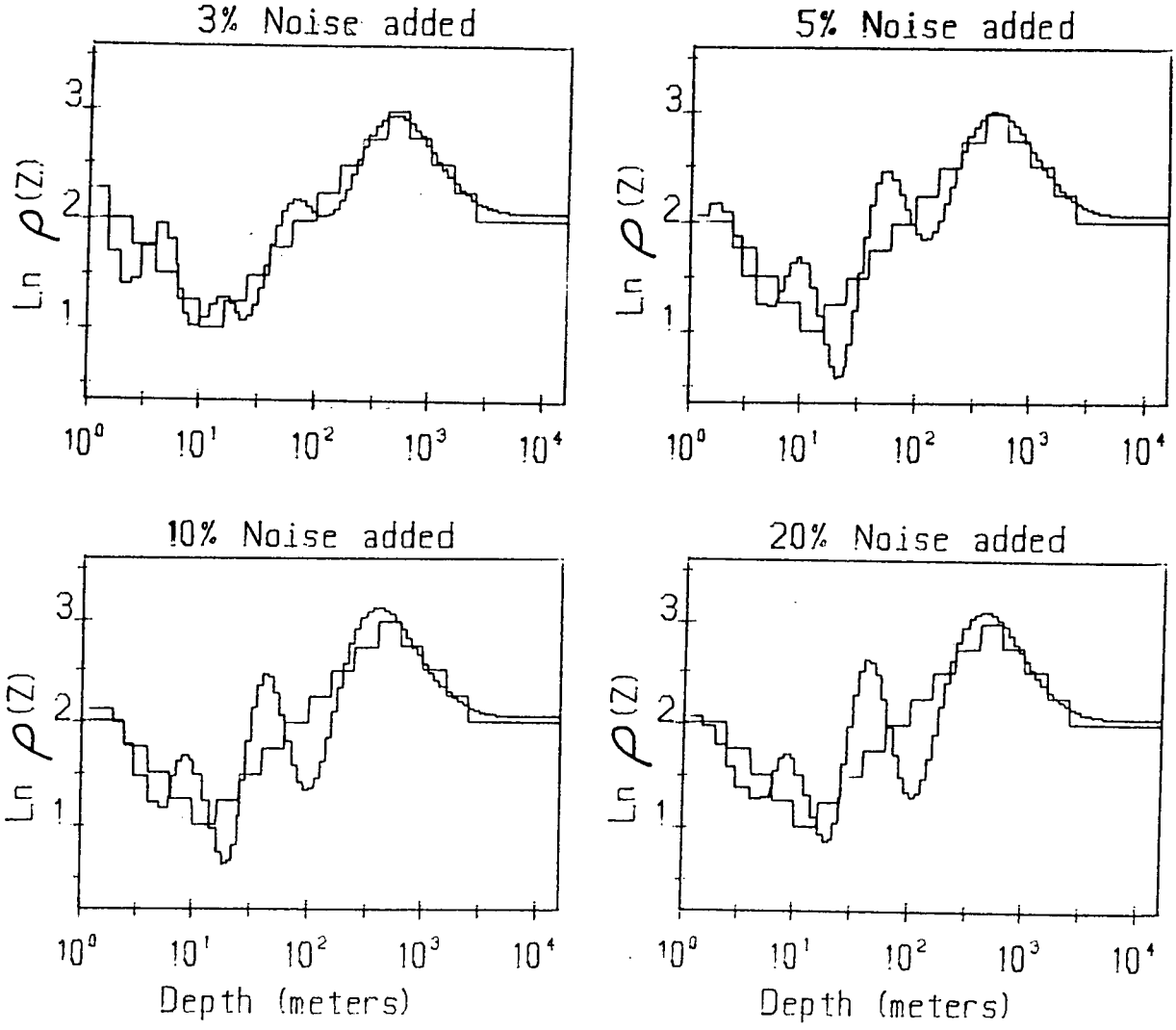

Figure 2.9 In each of these frames is a chi-squared acceptable model constructed from data to which the designated amount of random noise had been added. The models with 3 and 5 percent noise in the data took two iterations to converge, while those with 10 and 20 percent, required one more iteration. The shape of the final model does not change very much between 5 and 20 percent. Knowing the noise levels, the same general resistivity structure would probably be interpreted from any of these models.

All of the above models satisfy the chi-squared criterion for the noise levels applied. The largest change in final models occurs between levels of 3 and 5 percent. From 5 to 20

percent, there is little change, and the resistivity structure inferred from any of the four models would most likely be the same. However, it is easy to see how errors of 5 percent might cause a misinterpretation over more complex structure.

To find the dependence upon data density, Schlumberger data were calculated using expansion factors greater than 1.41. The degree to which this affects the reliability of the constructed model also dependents upon the scale length of the resistivity structure; obviously, very widely spaced data would be satisfactory over a half space. Therefore, this investigation will only return the maximum expansion factor possible for resolving this particular structure. Because there is a uniqueness theorum for resistivity measurements (Langer, 1933), it is true that infinitely many accurate data would resolve any one-dimensional structure. It is of practical interest though, to determine how a few, widely spaced data can resolve a certain structure.

Increasing the expansion factor from 1.41 to 1.71 had little effect on the final model other than to improve the fit in the region from 1 to 10 meters depth. The second increase to 2.28, likewise had little effect, except possiply allowing the position of the minimum resistivity to shift lower. By any standards, these are good fits to the true structure. No deterioration is apparent with these expansion factors. Had a structure with a smaller scale length been used, resolution with the scale factor of 2.28 may have been inadequate since higher density data is neccessary to resolve those features.

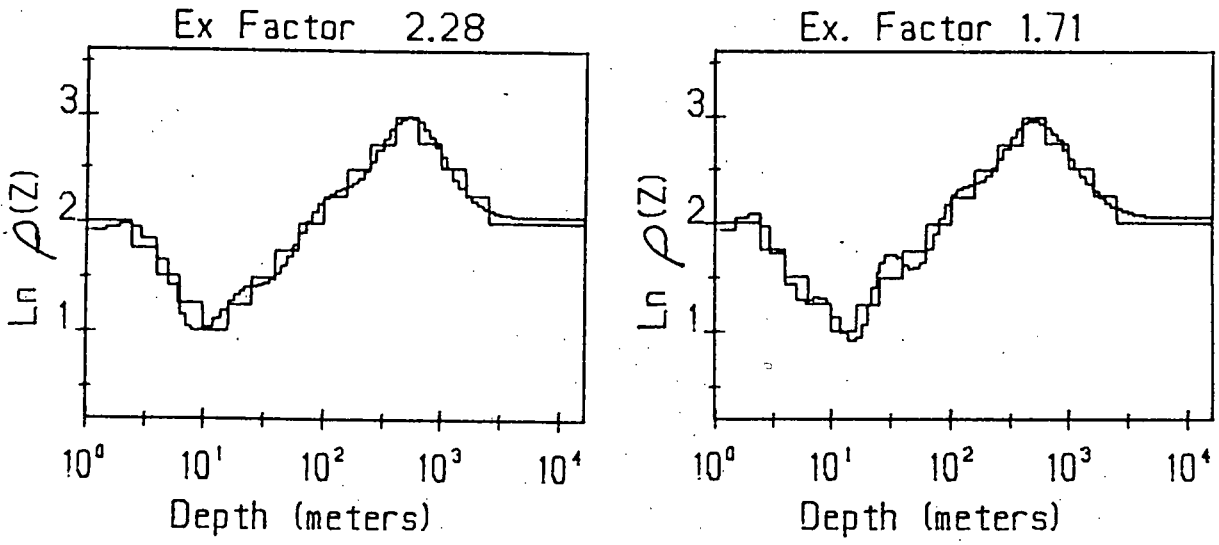

Figure 2.10 Decreasing the data density in this range did not affect the final models appreciably. The only noticeable difference between these two is that the resistivity low is displaced slightly shallower when the data density is at its lowest in the frame on the left. There are 13 data in the range from AB/2 of 5 to 3650 for an expansion factor of 1.71, and 9 in the same range with the expansion factor of 2.28. The maximum and minimum are correctly placed with expansion factors of 1.71, and 1.41 (see figure 2.3).

2-6.4 Representation Testing

The final way in which the linearized construction program should be tested is to construct models from the two extremes of structural variations. Its response to structures with no variation and large variations would be useful for interpreting constructed models, and should therefore be known.

When there is essentially no variation in the true structure, and iteration is started from a half-space value other than that of the true structure, it will be easy to see the variation between the constructed and the true models. This will illustrate how a region of constant resistivity may be represented on a constructed model.

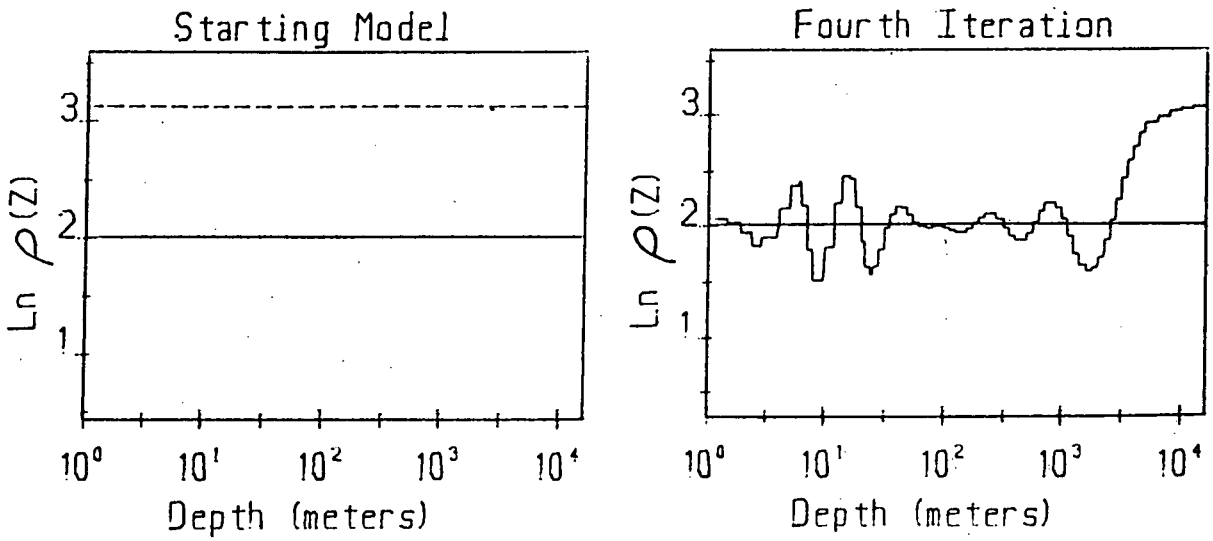

Figure 2.11 The true structure is a half-space of constant resistivity, and it is fit after four iterations by this oscillatory model. Notice that the constructed model matches the true structure most closely in the middle region, from 10**1.5 to 10**2.5 meters. There the model is constrained by both shallower and deeper seeing data. This figure is meant to illustrate the differences that are possible between a chi-squared acceptable model and the true structure.

With construction programs response to a half-space known, it remains to be seen how a large change in resistivity over a short distance will be represented. To test this, the true structure used is a box car function with the resistivity high an order of magnitude greater than the surrounding half-space. From the previous experiments, it has been learned that representative models can be constructed from twenty data starting from AB/2=5 with an expansion factor of 1.41, when the true structure has only large scale feartures. With this noted, we would expect the model constructed to be a smoothed version of the box car due to the lack of resolution, and to fall away from the true structure at about 1000 meters depth. This does in fact describe the construction.

In figure 2.12, the starting, first, and final models are shown with the box car superimposed upon each. The constructed model smooths the resistivity increase and decrease, and matches the box car best in the midrange. At 700 meters, the decrease is somewhat better fit than the increase at 20 meters, but clearly the resolution is lost just below there since the model dips below the true structure at 1000 meters.

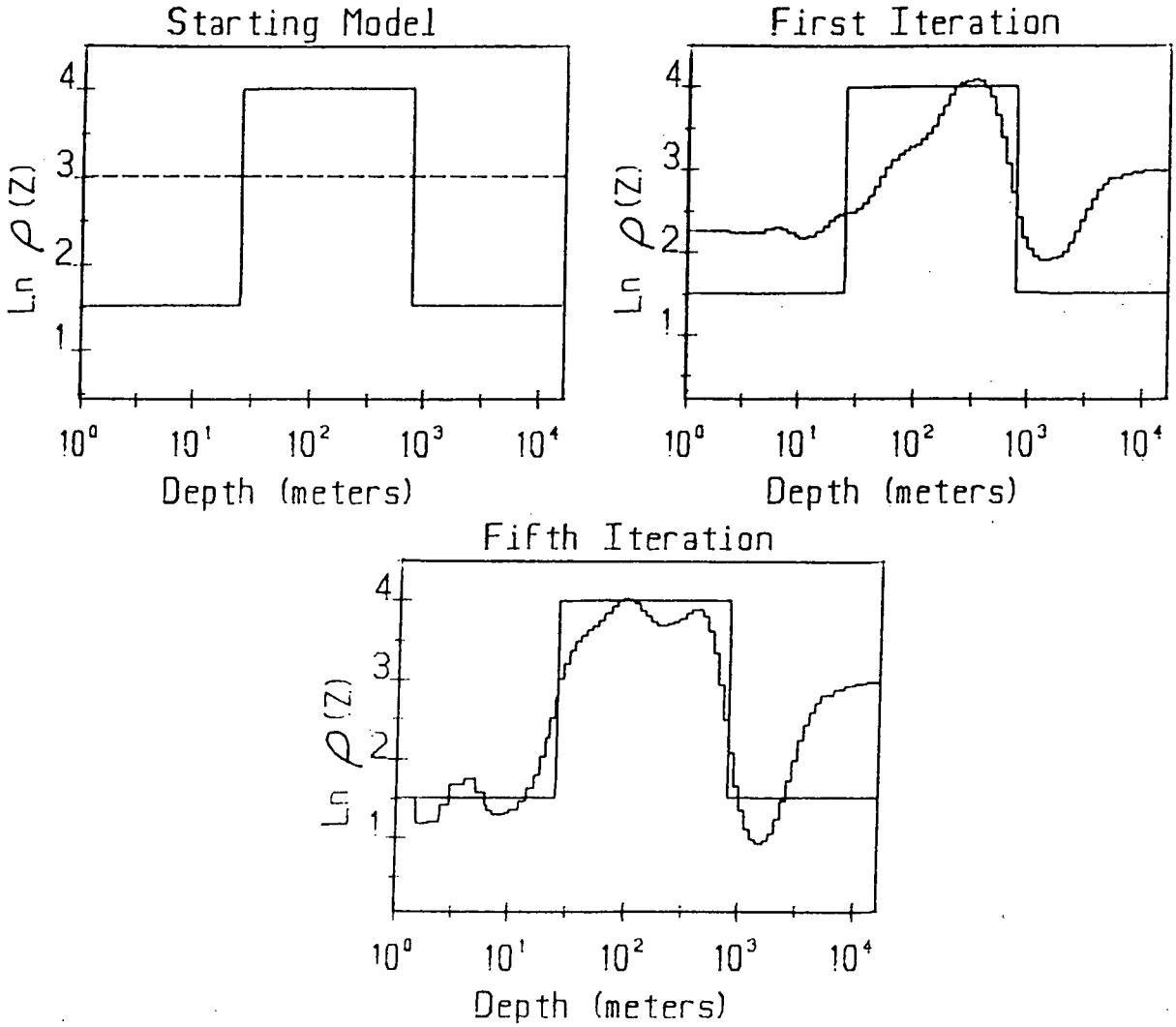

Figure 2.12 This test was to illustrate the constructed model's representation of an order of magnitude change in resistivity. The true structure, which is a 4.5 ohm-meter half-space with a 45 ohm-meter layer from 20 to 700 meters depth is matched quite closely by the model constructed after five iterations. As expected, the constructed model is somewhat smoother. High frequency features such as the corners of the structure cannot be reproduced because of the resolution of the data; therefore monotonic variations which take the constructed model through a large change in resistivity should be interpreted as layer boundries.

The general findings in testing the linearized construction program have been encouraging. It is a fairly robust program, constructing representative models from data with errors, and constructing reasonable models in every one of the tests performed. A wide range of theoretical structures have been reproduced from synthetic data. The degree of closeness between the constructed and theoretical models does not seem very dependent upon the choice of starting models, but a model is converged upon in fewer iterations when construction is started from the best flat line through the apparent resistivity curve. Further, the construction program was quite insensitive to data density over the structure used in the first two experiments, and nine data with an expansion factor of 2.28 would have adequately reproduced it.

CHAPTER 3

A Resistivity Survey in the Anahim Belt

In 1981 a large scale resistivity survey was carried out in the Anahim volcanic belt in British Columbia by Premier Geophysics under contract from the Geological Survey of Canada. The region surveyed is at the eastern end of the volcanic belt, where the recency of eruptions may signify the presence of economic geothermal energy.

The Anahim belt is a chain of Miocene and Quaternary volcanoes running from west to east approximately along the 52nd parallel. Its western limit is at Bella Coola, and its eastern limit is at Blue River (see figure 3.1). The last eruption at the western edge was 14.5 m.y. before present, while in the vicinity of Blue River 10 thousand year old lavas exist. This gradation in ages of lavas from east to west suggests that the eastern edge has the highest potential for geothermal energy, and has been used as evidence for a mantle hot spot beneath the area (Bevier et al. 1979). Resistivity surveying was used here in an effort to locate the low resistivities commonly associated with high temperatures. Some such anomalies were found, but their correlation with high temperatures at depth is still unestablished as they have yet to be drilled.

The resistivity experiment done in the Anahim belt will be described, and resistivity models constructed from the Schlumberger soundings will be presented. Geothermal interpretations will then be made from the models constructed and the existing geological information.

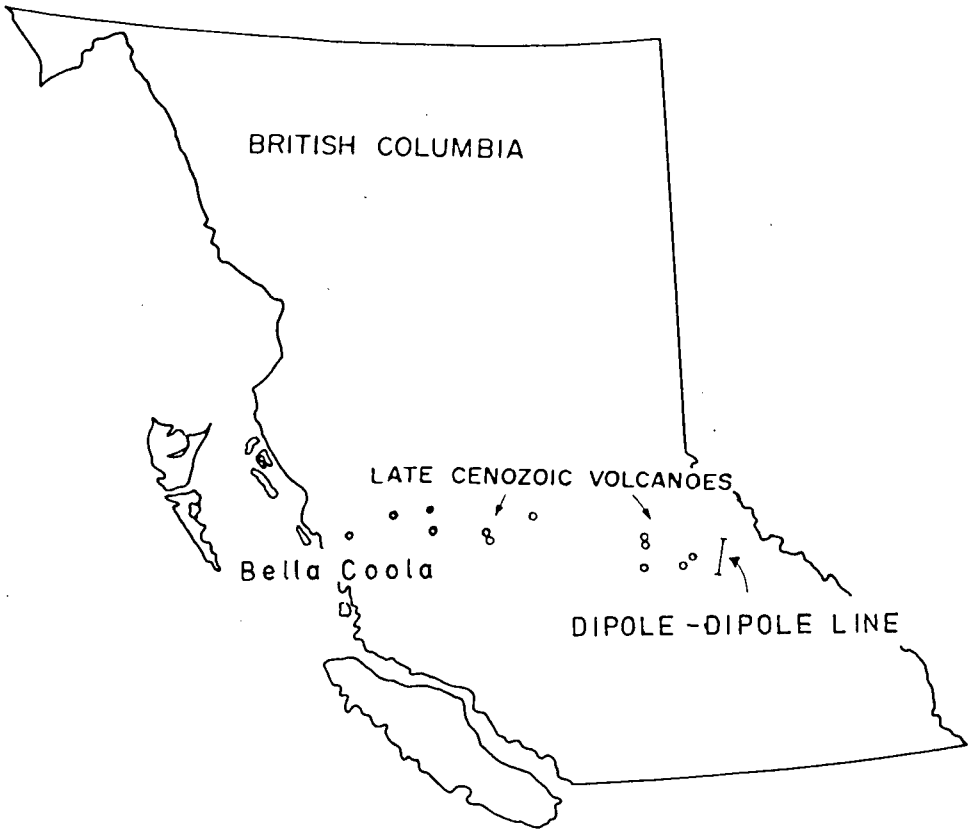

Figure 3.1 locations of some recent volcanoes in the Anahim volcanic belt, and the dipole-dipole survey line. The Schlumberger sites were along the dipole-diploe line. Figure 3.2 shows their exact locations. (from Schlax and Shore 1981)

3-1 The Anahim Resistivity Experiment

While the main purpose of the survey was to assess the area's geothermal potential, it was also used for reconnaissance purposes since the geophysical data base is so minute. Neither aeromagnetic nor gravity data exist for the area. Thus the resistivity survey consisted of two parts: a long dipole-dipole line from which the geoelectric cross section of the belt was obtained, and six Schlumberger soundings for the more detailed picture and for correlation with the dipole-dipole line.

The dipole-dipole line ran roughly north-south across the suspected hot spot trace, and the Schlumberger soundings were expanded along the line and in adjoining valleys to the west,

perpendicular to the line (see figure 3.2). Dipoles of lengths one and two kilometers were used, with separations from 1 to 8 kilometers for the 1 km dipoles, and 1 to 6 kilometers for the larger ones. This provided a deep-probing pseudo-section across the belt while the Schlumberger arrays, which had a maximum AB/2 spacing of 2 km, produced data reflecting shallower features. Their maximum penetration was between 1 and 2 kilometers.

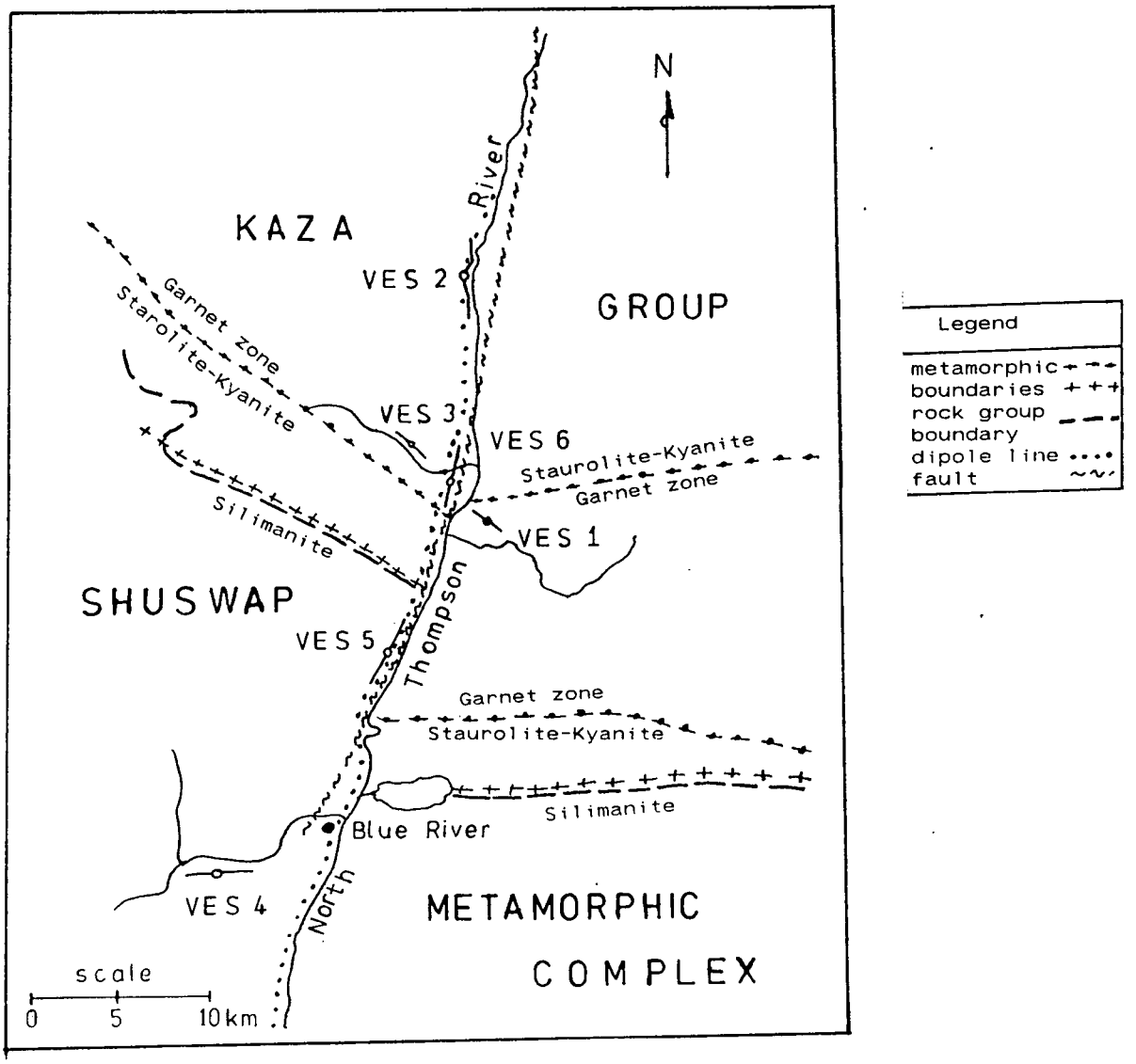

Figure 3.2 North Thompson River valley showing the six Schlumberger sites and the major geologic boundries. The thick dashed lines represent the boundary between the Kaza Group and the Shuswap Complex, and the thin dashed lines are boundaries between metamorphic zones. (from G.S.C. Map 1967-15, Canoe River)

In both of the surveys, the potential differences were recorded on a Hewlett-Packard chart recorder with a maximum resolution of 10 microvolts, while a Pheonix Geophysical transmitter supplied the current. A square wave current, with an 8 second period, and 100 percent duty cycle was used. Data quality for the Schlumberger soundings was generally very good, as can be seen in figure 3.3. Telluric, and instrumental noise levels were both low.

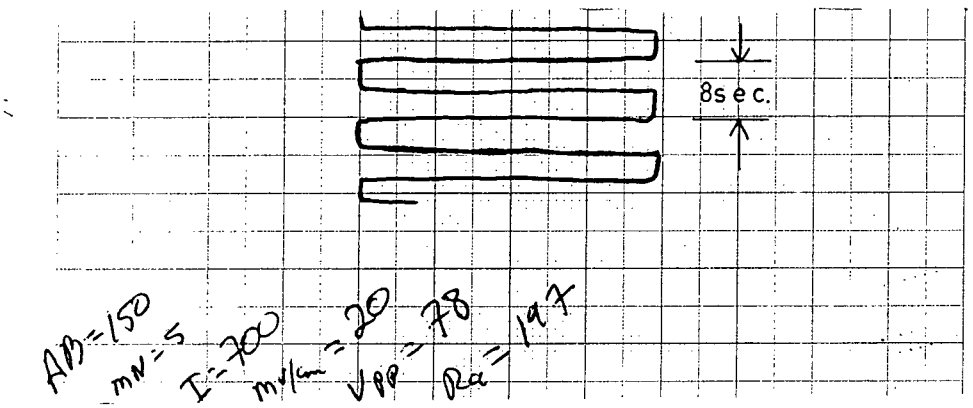

Figure 3.3 Potential difference record from VES 1 at AB/2 = 150m. The scale is 0.02 volts/cm. Both instrumental and telluric noise levels are very low.

The uncertainty level associated with this reading which is an AB/2 spacing of 150m on VES 1 is only about 2 percent, but a 10 percent standard deviation was assigned to accomodate for errors arising from the one-dimensional approximation and nonplanar topography. Where telluric noise was excessive, a mechanical filtering technique was employed for picking out the square wave's amplitude. (Premier Geophysics, 1979)

3-2 Causes of Resistivity Anomalies in Geothermal Areas

Here, as in most geophysical experiments, the quantity measured is not that which is ultimately desired. Rather, it is the physical property most correlatable with what we really want to find – in this case a heat source. The fact that high temperatures near the surface correlate with low resistivities makes the resistivity survey a useful geophysical method in geothermal exploration. Geochemical, and geological data are also essential for developing the entire picture of a geothermal area.

High temperatures near a heat source are manifested in anomalously low resistivity values for the following reasons.

1. High temperatures increase the permiability by fracturing rocks thereby allowing more ground water to enter. This in turn lowers the bulk resistivity.

2. The resistivity of water decreases with increasing temperature independent of salinity. (see figure 3.4)

3. Soluble minerals present, such as salt, go into solution more readily as a result of higher water temperature and decrease the resistivity further. Sulpher minerals, which are often present in geothermal water systems, have the same effect as salt. The less soluble minerals percipitate out as the temperature decreases near the surface, and crystalize on the sides of the conduits.

The influence of temperature and salinity on the resistivity of water is shown in figure 3.4. Data from the

Meager Creek geothermal area (also in B.C.) is included as a reference point for geothermal water. Any one, or all, of these effects will be instrumental in producing anomously low resistivities near a heat source making its detection with a resistivity survey possible.

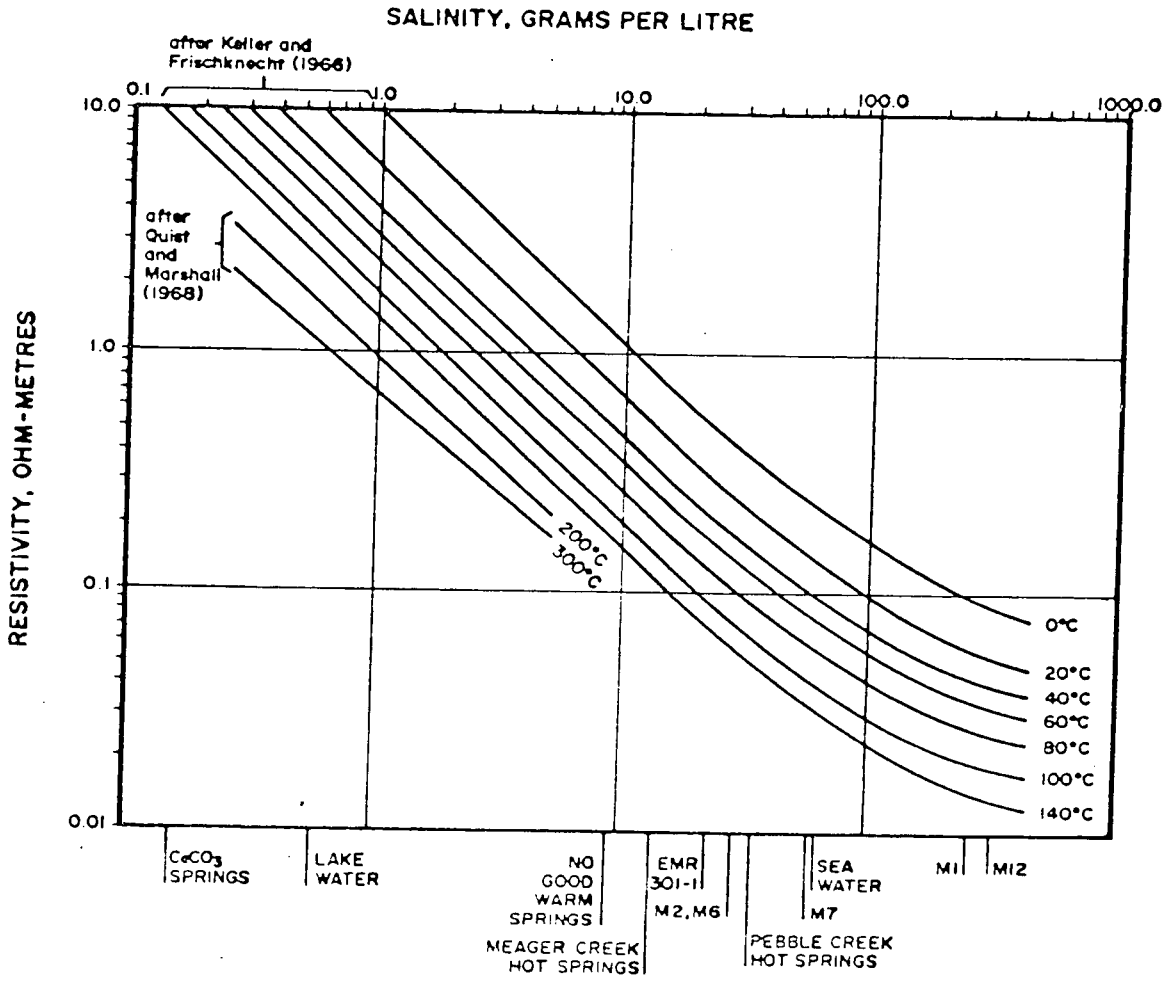

Figure 3.4 The variation of water resistivity with temperature and salinity. (from Schlax and Shore 1981).

3-3 Geological Settings of the Schlumberger Soundings

Using the Geology map entitled Canoe River (15-1967), the general geological environment of the survey area will be described, and the local geology at each Schlumberger site will be detailed in anticipation of the constructions.

The large scale geology is dominated by the North Thompson fault, and two Precambrian rock groups: the Kaza Group, and the Shushwap Metamorphic Complex. Both rock groups have undergone extensive thermal metamorphism in the survey area, and all but one of the Schlumberger soundings are in the Staurolite-Kyanite or Garnet zones of these rock groups. The North Thompson fault is a west side up normal fault having at least four kilometers of vertical throw (Pell and Simony, 1981 in Schlax and Shore, 1981). It extends from the township of Blue River, north through the survey area, and ends at the B.C.-Alberta border (see figures 3.1 and 3.2). The lateral displacement is slight, and the only place where Kaza, and Shushwap rocks oppose each other across the fault is at VES 5. Everywhere north of there the rock is of the Kaza Group, and everywhere south, it is of the Shushwap Complex. In the survey region, the metamorphic grade increases to the north hinting that a regional heat source, whether past or present, lies in that direction.

Extreme topographic variations characterize this part of the province. That is why the North Thompson River valley was chosen for the survey site despite the presence of such a large fault. In addition to the two major rock groups, there are glacial alluvium deposits on the valley floor, and in most

of the drainages leading into the valley. These are presumed thin.

VES 1 is situated on a small flood plain on the eastern shore of the North Thompson River, approximately in the middle of the survey area. Its purpose was to determine the resistivity of the alluvium which covers the ground at this and some of the other Schlumberger sites. Thus, it was expanded as far as the alluvium deposit allowed. The maximum AB/2 spacing possible was 500 meters, then marshy ground was encountered to the north-east. Kaza rock in the Garnet zone underlies the alluvium here, and the fault is to the west.

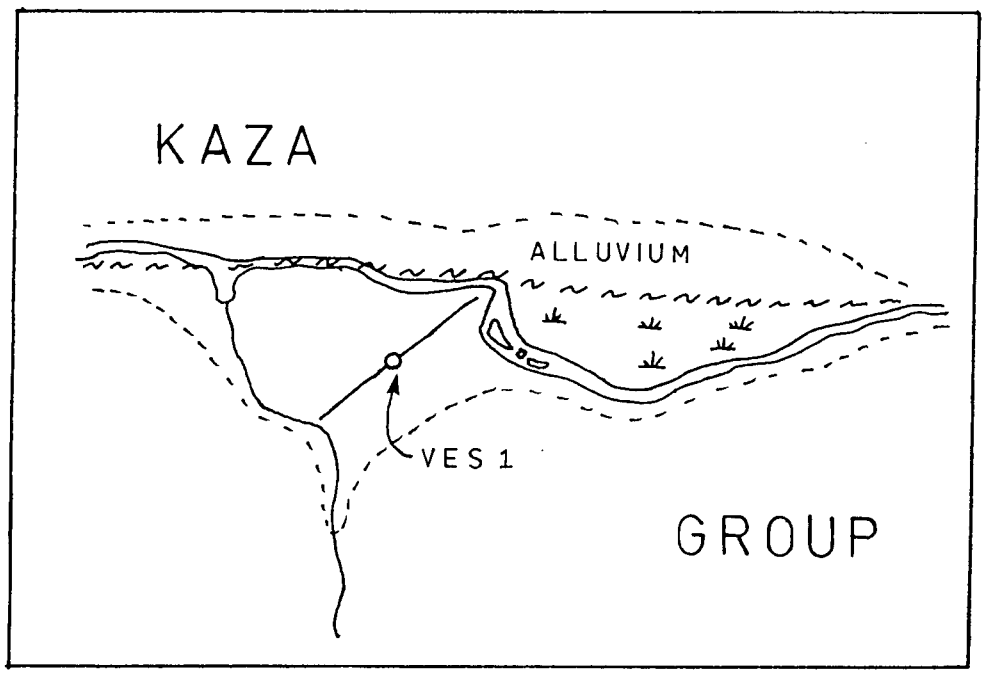

Figure 3.5 An enlargement of the VES 1 site. The electrodes were expanded out to the limits of the alluvium deposit which overlays Kaza Metasediments.

The valley is very steep at VES 2, which prevented the electrodes from being expanded in a straight line. Instead, they were expanded in a elongate W pattern. Being in the

valley gorge, as it is, the surface expression is alluvium – sand and gravel. There is no bedrock exposure, but the underlying rock is Kaza in the Staurolite–Kayanite zone with Garnet zone metamorphism across the river. This sounding is sufficiently west of the fault that only the largest expansion could register its effect.

VES 3 runs perpendicular to the fault and the dipole-dipole line in a narrow drainage to the west of the North Thompson River (Miledge Creek). Alluvium covers the ground here too, but Kaza Group rocks in the Garnet zone outcrop on either side of Miledge Creek, and likely underlay the alluvium at a shallow depth.

The fourth Schlumberger sounding, VES 4, is oriented in a similar manner to VES 3, but in the Blue River drainage, thirty kilometers south of Miledge Creek. This drainage is broader and less steep, so the alluvium which covers the floor here is probably thicker than at VES 3. Since the surrounding topography is quite subdued and the fault fairly distant, the flat earth approximation is probably quite valid. The one-dimensional approximation may not be, however, as foliation or gneissosity has been measured as dipping at 50° to the southeast nearby. This is the southernmost sounding, and is in the Sillimanite zone of the Shushwap Metamorphic Complex which is the lowest metamorphic grade.

VES 5 is in the Thompson River valley very close to the fault trace. It is also close to an oil pipeline and railroad track, but neither of these was judged to have had any effect

the readings (Schlax and Shore, 1981). The spread was entirely on alluvium, and just west of the fault trace where rock of the Shushwap Metamorphic Complex in the Sillianite zone lies opposite that of the Kaza Group in the Garnet zone to the east (see figure 3.6). This was one of the longest spreads and the closely spaced data show no wild fluctuations, however it overlies some complex geology which makes the interpretation correspondingly difficult. Since currents flow sideways, in addition to straight down, these measurements probably averaged the resistivities of the two rock groups after a certain expansion was reached. This must be taken into consideration when VES 5 is interpreted.

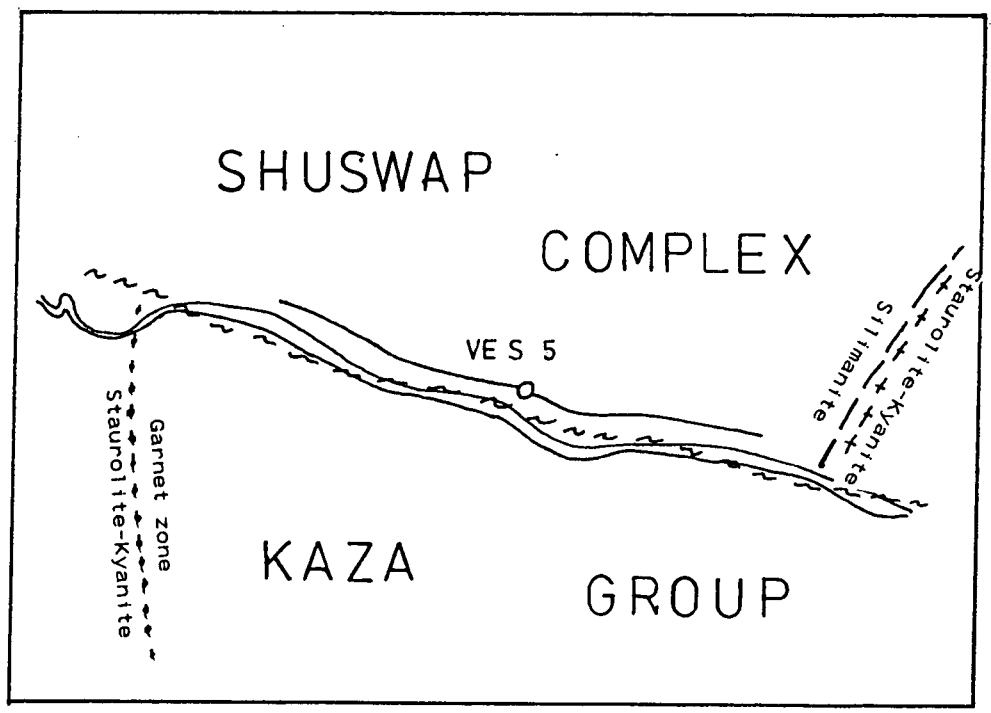

Figure 3.6 local geology at VES 5. It is on the west side of the fault trace, in rock of the Shuswap Metamorphic Complex, but the proximity of the Kaza Group across the fault will likely affect the measurements.

VES 6 was expanded halfway between VES 5 and VES 2. It was also on alluvium that overlies rock of the Kaza Group.

The spread itself was just west of the fault which put it in the Garnet zone, but the grade to the east is Staurolite-Kyanite. (see figure 3.2) Most of these measurements will have been affected by the fault zone, and those taken at larger AB/2 spacings may show an effect related to the change in metamorphic zone across the fault. Any resistivity contrast between the two metamorphic grades should be noticable on the apparent resistivity curve.

3-4 Constructions Obtained from the Schlumberger Data

Resistivity models have been constructed from each of the six Schlumberger data sets. In most cases, only the smallest perturbations were used because of their more robust convergence, but for VES 5 a model was easily constructed with the flattest perturbations too. The general problem with these constructions is that most of the data sets seem affected by lateral inhomogeneities because they violate the slope rule for one-dimensional structure somewhere (Keller and Frischknecht, 1977) The only way to compensate for this is to increase the standard deviation assigned to the points which simply allows a looser fit to these data. The model's fit to the data can be seen in the first frame of each of the following figures. Apparent resistivity curves were predicted from each of the final models, and superimposed upon the apparent resistivity values derived from the data. The one standard deviation error bars are shown for those apparent resistivities. From the degree of intersection, one can see which data cannot be fit by the program and hypothesize about

the influences – such as laterally varying structure. Data points which did not break the slope rule were normally assigned a standard deviation of 10 percent, while those which did were either assigned a greater standard deviation or omitted, depending upon the severity.

VES 1

Models were constructed from two starting models for this data set: a half-space, and a two-layered structure. The latter is strongly suggested by the apparent resistivity curves, and is shown in figure 3.7b to fit the data with little change.

Since the minimum AB/2 spacing is 25 m, the resistivity of the top layer cannot be constrained very well. With this noted, the model constructed from a half-space matches that started from the two layered model over the rest of its range. Both models show a distinct change in resistivity between 20 and 30 meters, corresponding to the thickness of the first layer. Below that, the resistivity of both models drops to around 150 ohm-meters at 100 meters depth and increases slightly with greater depth. The constructed models are reliable only down to two hundred meters (indicated with an arrow). Resolution decreases rapidly below that, as the model returns to its initial value. The upswing between 100 and 200 meters is indicated by the data. Only the smallest perturbations were used for this constructions.

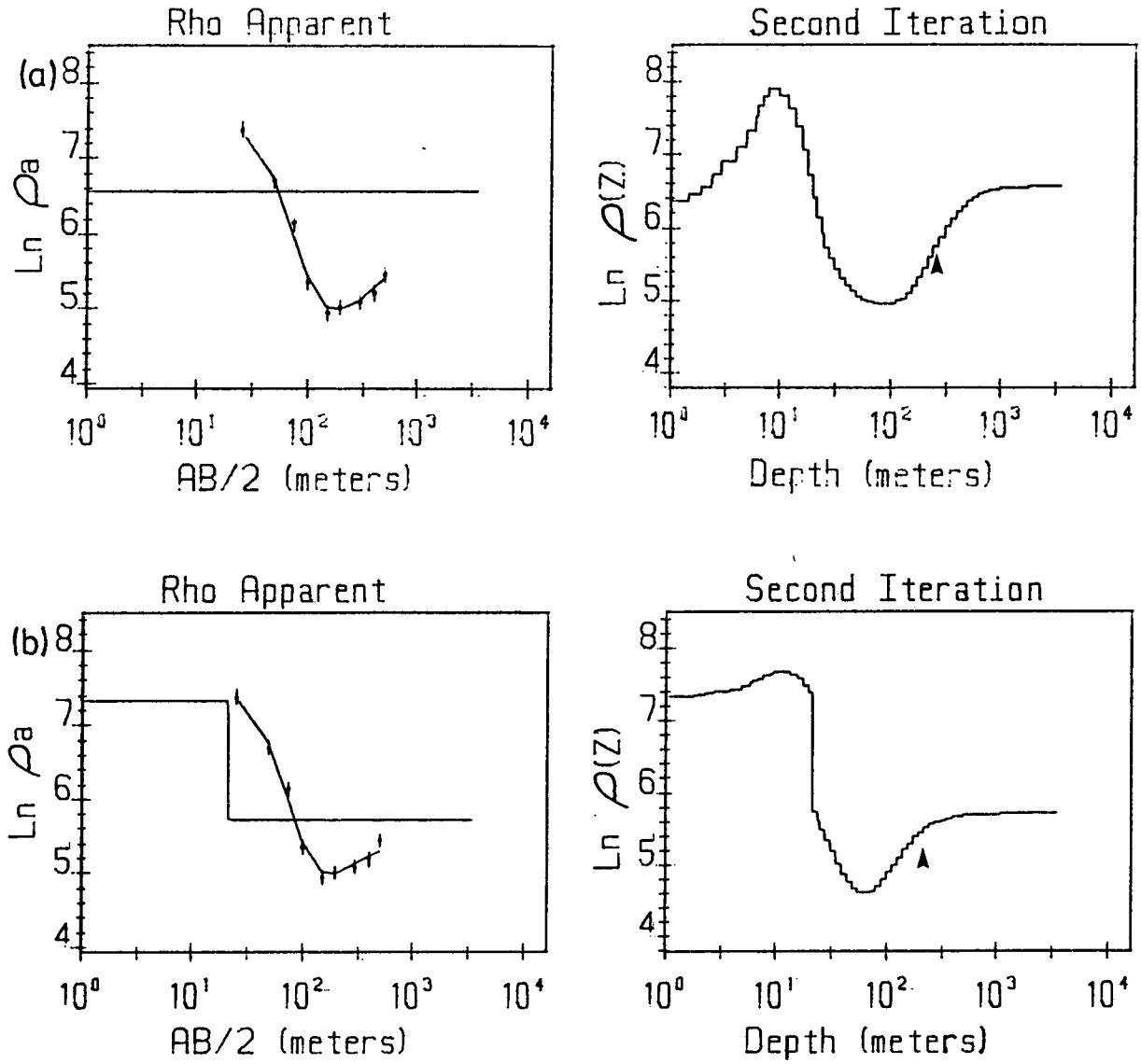

Figure 3.7 VES 1 constructions from a) a half-space of 700 ohm-meters, and b) 1500 ohm-meter layer 22 meters thick over a 300 ohm-meter half space. The models differ only in the top 20 meters illustrating the lack of resolution there. The depth to which the model can be considered reliable is indicated with an arrow.

The interpretation is simply a verification of the known near-surface geology. Highly resistive alluvium overlies the less resistive rock of the Kaza Group. An approximate depth to the Kaza interface is 22 meters and, although it cannot be exactly placed, it likely is a sharp, glacier-scoured boundary.

VES 2

At VES 2 the situation is more complex. The apparent resistivity curve is well sampled by 15 closely spaced data. It shows one major low zone, and an inflection in the last two data. The constructed model however, shows three low resistivity zones with minima at 20, 160, and 1200 meters. Only the main low at 160 m should be interpreted though. The first low is based upon a single point, and is accentuated by the shoulder on the main anomaly (see figure 2.12). At 1200 m, the decrease is also probably a shoulder anomaly. Notice that the predicted apparent resistivity curve shows only one broad low. Again, only the smallest perturbations were used.

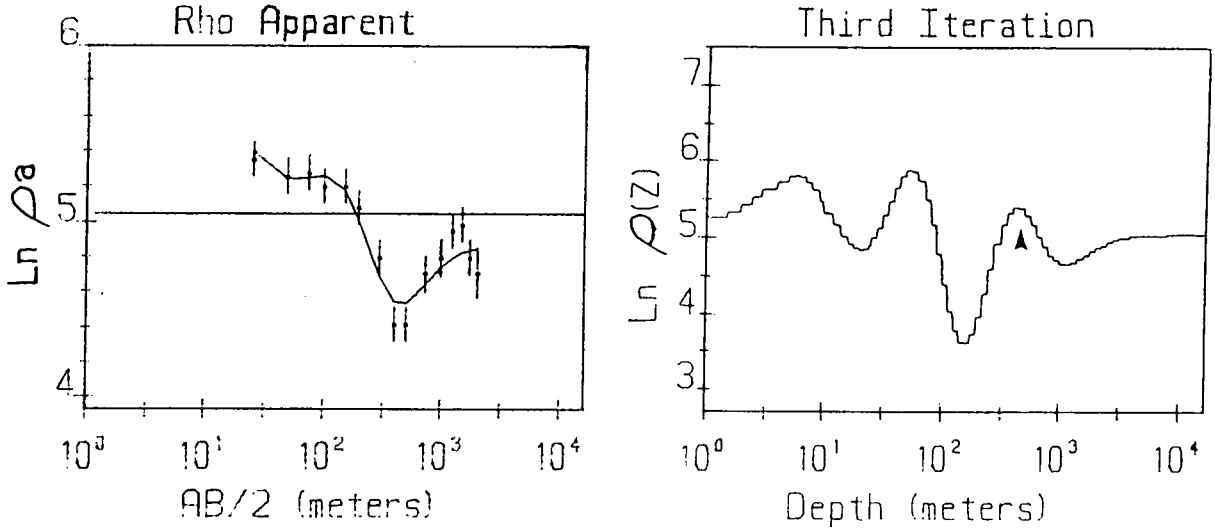

Figure 3.8 VES 2 construction. The starting model was a 155 ohm-meter half-space, and the final model was achieved after 3 iterations. From the left frame, it appears that the 10 percent standard deviations were used to overcome a lateral effect encountered at larger spacings.

Only resistivities representative of the Kaza Group are seen, with an interesting decrease between 50 and 300 meters. No highly resistive top layer is indicated here as it was in VES 1. The lack of colinearity among the electrodes was

compensated for and was found to have a negligable effect.

VES 3

VES 3 is a problematic data set. The data with AB/2 spacings greater than 200 meters show a great deal of scatter; the apparent resistivity changes from 180 ohm-metrs at AB/2 of 400 meters to 1300 ohm-meters at 500 meters. This violates the maximum slope rule for apparent resistivity curves. Either lateral inhomogenity is affecting the measurements or there is some other problem, but these data cannot be fit by the program.

The apparent resistivity curve for the remaining six points looks somewhat similar to that of VES 1. A constant decrease from a high near surface values which probably represent alluvium is shown. Constructions were started from both a 650 ohm-meter half-space, and a model identical to that used for VES 1, except that the top layer was 6 meters thinner.

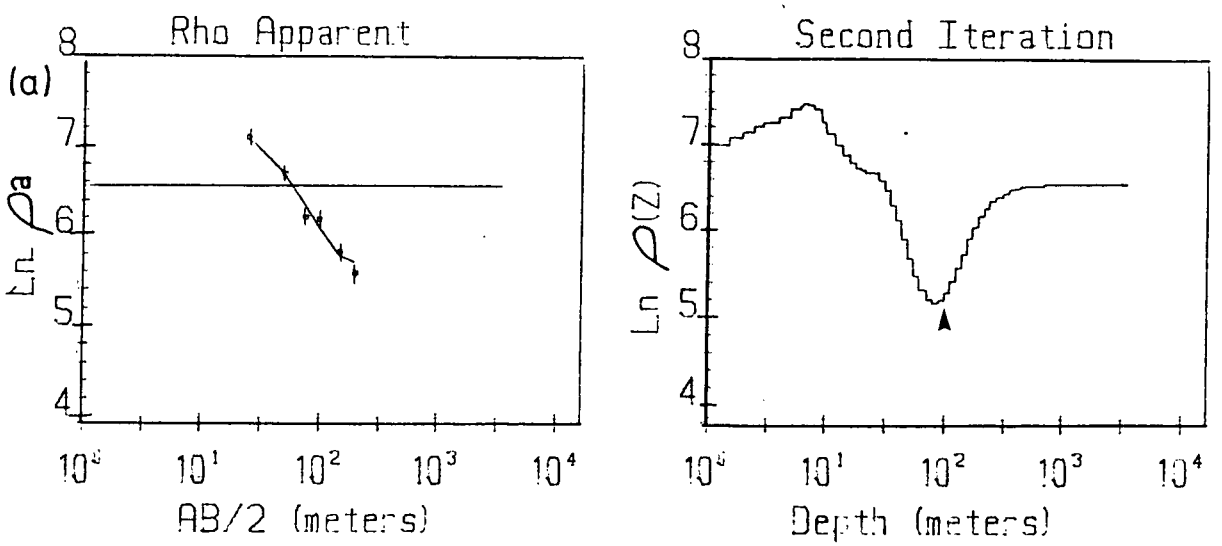

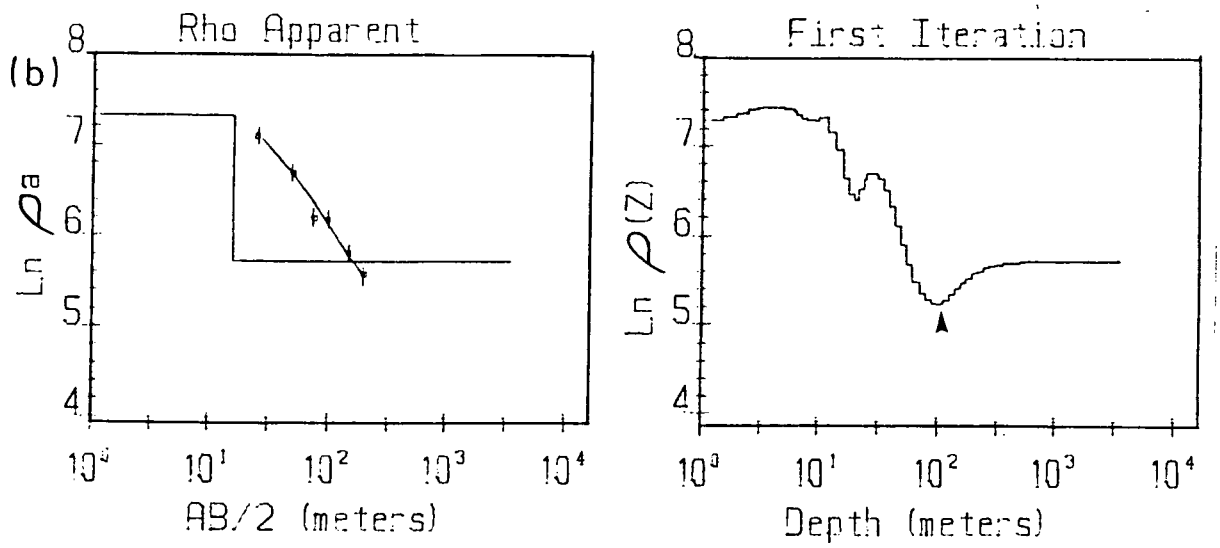

Figure 3.9 VES 3 constructions. The first six data (up to AB/2 = 200 meters) were fit in one iteration from a starting from a starting model similar to that used in VES 1 and in two iterations from a 650 ohm-meter half-space. The starting models seem to have had little effect on the final models since they are so similar between 10 and 200 meters.

The only information that can possibly be gleaned from the last four data points is that they show a general increase in resistivity.

VES 4

The VES 4 data set also shows effects which are probably due to lateral inhomogeneities, but this is not surprising as 50° folding was indicated on the geology map. Apparent resistivity curves as steep as those which appear here are impossible over a one-dimensional structure (Keller and Frischknecht, 1977). Nevertheless a very low resistivity zone is shown in the data and reproduced in the constructed model.

Greater error than 10 percent was needed for the data point at the AB/2 spacing of 500 meters, and the validity of points at 750 and 1000 meter AB/2 spacings must also be questioned. A rock type change was crossed on the surface when the current electrodes were expanded to an AB/2 of 500 meters, so perhaps all of the data points from there out will introduce errors into one-dimensional constructions. For this

reason another model was constructed using only the data up to an AB/2 spacing of 400 meters (see figure 3.10b). It was essentially a half space of 1200 ohm-meters. This resistivity value is very different from those observed in the VES 1-3 constructions and is indicative of a different rock group, the Shushwap Metamorphics. The downturn present in figure 3.10b now arises from only one point and is therefore open to question. If it is considered reliable, an interesting decrease exists and if not, then the resistivity of the first 200 meters is approximately 1200 ohm-meters.

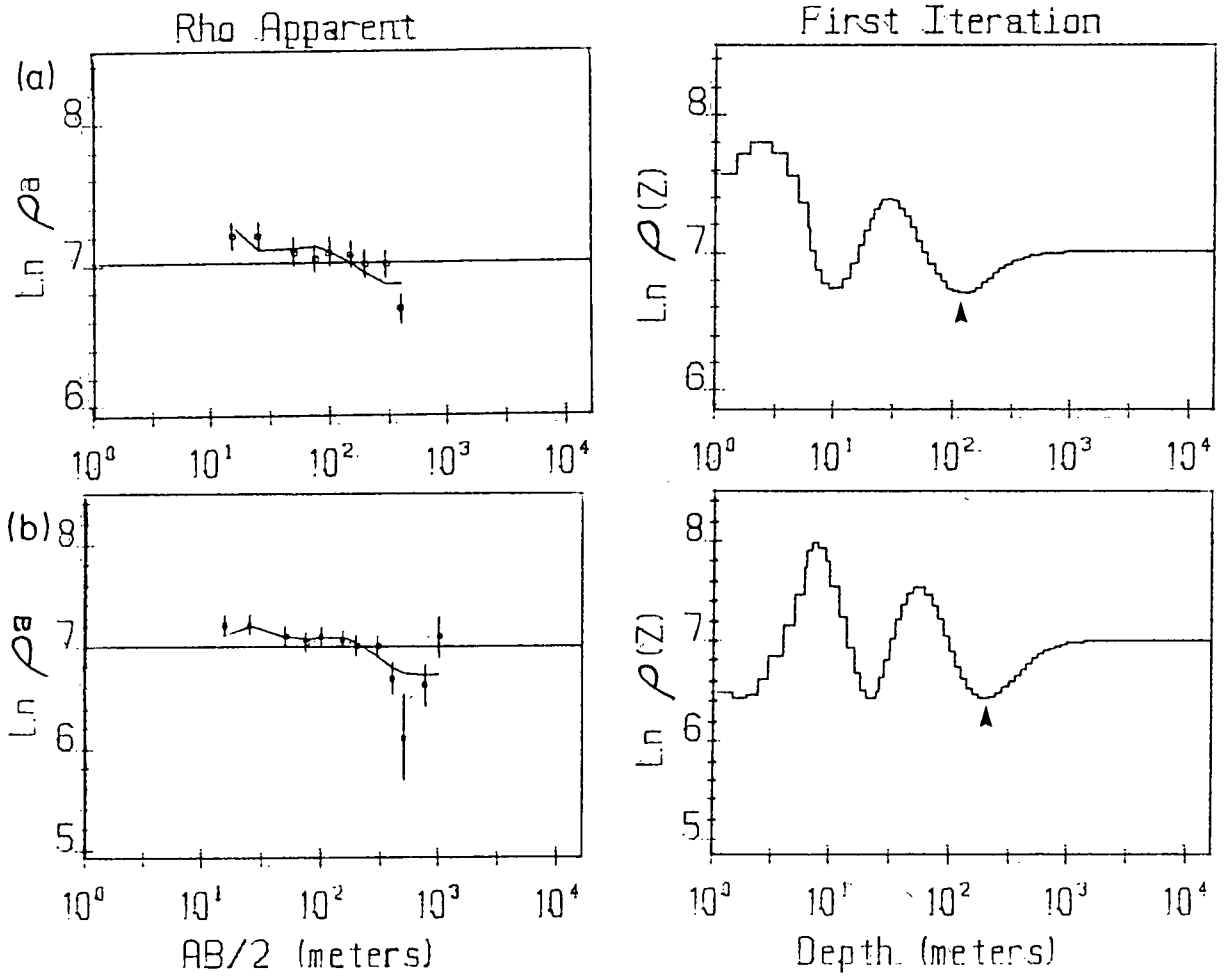

Figure 3.10)a Model constructed from the first nine data in VES 4, all with 10 percent standard deviation. The 1100 ohm-meter starting model fits the data after one iteration.)b shows the construction obtained from all twelve data. The last two data were assigned 20 percent standard deviations, and 40 percent was assigned to the data point at AB/2=500m.

VES 5

The VES 5 model has similar resistivity values to VES 4 down to 200 meters; it is quite resistive. These two soundings are in marked contrast with those in the Kaza Group. From VES 4 and VES 5, the Shushwap Complex is seen to be significantly more resistive than the Kaza Group at shallow depths.

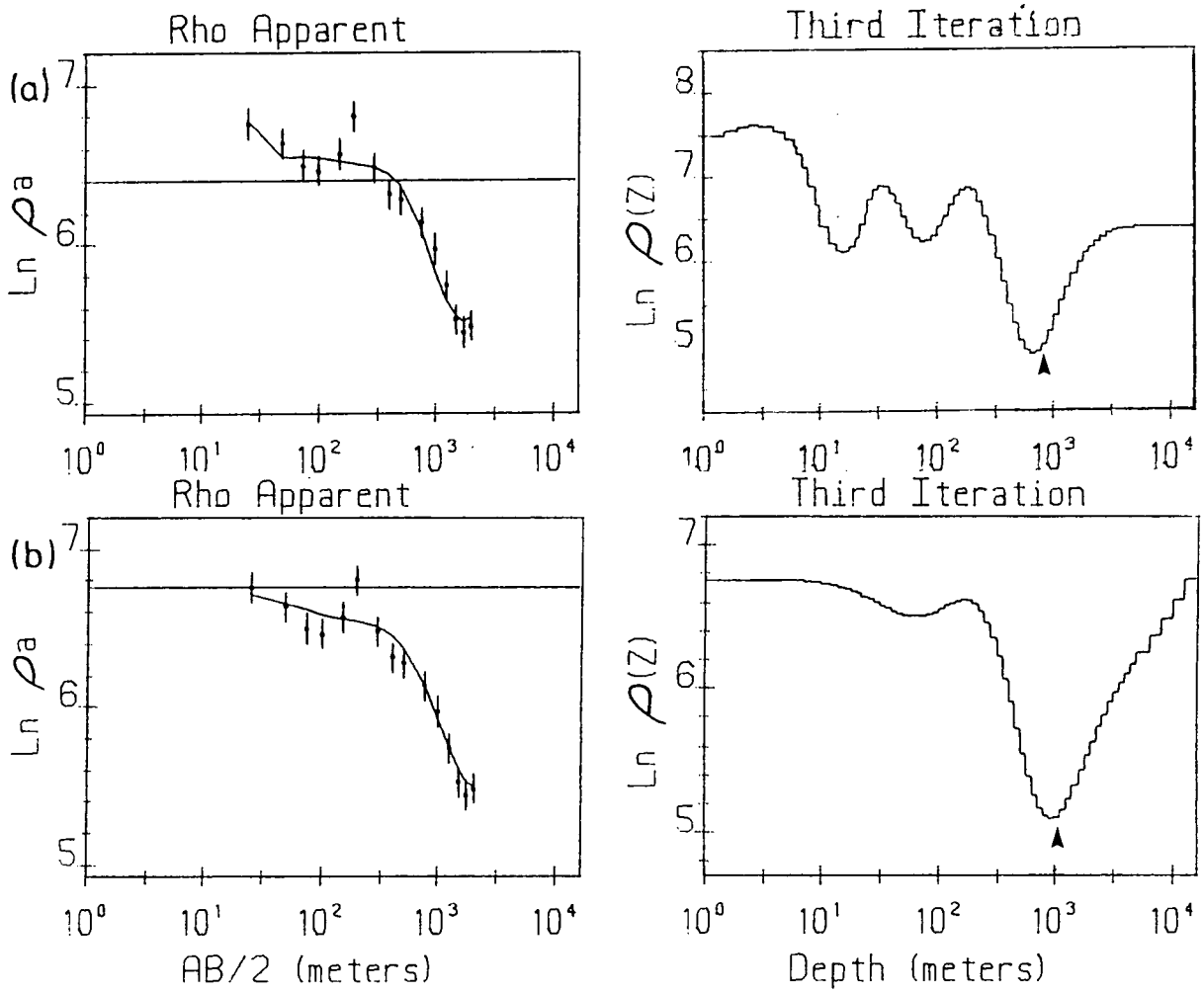

Figure 3.11 Smallest and flattest constructions for VES 5. All of these data were assigned 10 percent standard deviations.
)a shows the final model constructed with smallest perturbations.
)b shows the model construted using the flattest perturbations.
The flattest perturbation model shows that one low resistivity zone can fit the data.

With the exception of the data point at AB/2=200 meters, this data set obeys the slope criterion for one-dimensionality. The downward trend in the apparent resistivity curve is substantiated by eight data points. An upturn is indicated by the last data point; however its reliability is questionable as it is only one point.

Models were constructed using both the smallest and flattest perturbations (figures 3.11a and 3.11b) and both show the same basic features. The resistivity decreases from 900 to 150 ohm-meters over the range from 100 to 1000 meters. Clear trends and reliable depth information make these two constructions very valuable.

A geological explanation for the drop in resistivity is current leakage across the fault into the less resistive rock of the Kaza Group, but it could also be described geothermally by a very high temperature gradient at depth. This is certainly an interesting and important sounding.

VES 6

A half-space of 220 ohm-meters comes very close to fitting the data for VES 6. After one iteration a zone of lower resistivity is placed from 50 to 250 meters. The shoulders on this low resistivity zone are probably insignificant. They have been observed before when the true structure is a half-space with an internal layer of different resistivity (see figure 2.12). Therefore, the structure indicated is a 220 ohm-meter half-space with a zone of 150 ohm-meters extending from 50 to 250 meters in depth.

Resistivities in this range (150-250 ohm-meters) now appear to be representative of the Kaza Group.

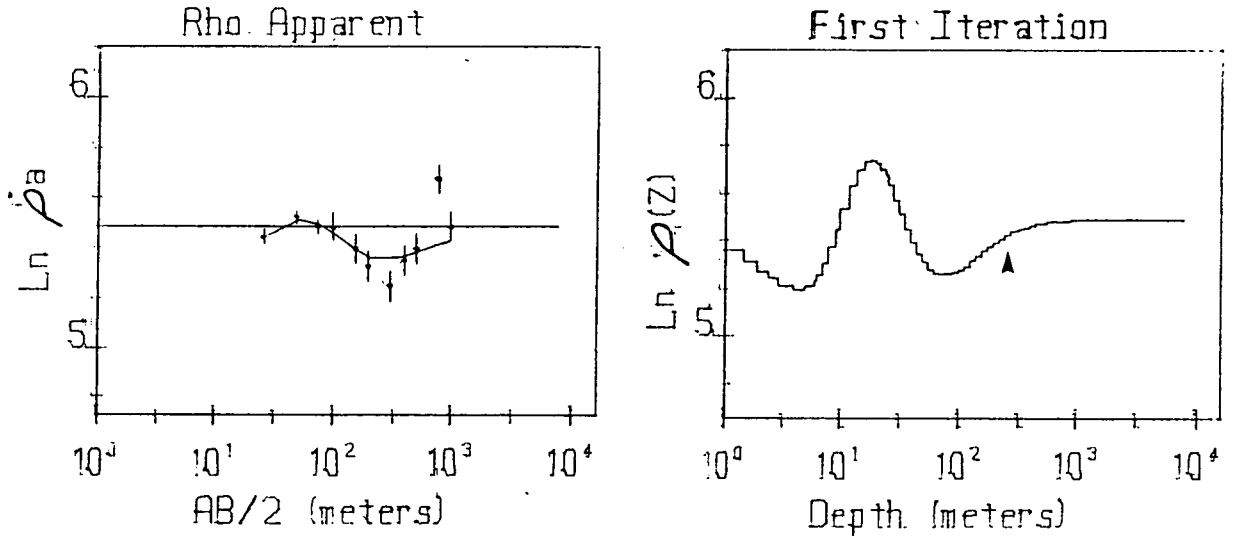

Figure 3.12 Construction obtained from VES 6 data, essentially a half-space.

3-5 Results from the Dipole-Diploe Line

The pseudo-section obtained from the dipole-diploe survey (Schlax and Shore, 1981) aided in the interpretation of Schlumberger soundings VES 5, and VES 2. It was also consulted when formulating the integrated interpretations because it extends on either side of the area where Schlumberger measurements were made. As mentioned earlier though, its information reflects larger scale and deeper features.

The most striking feature on the pseudo-section is a transition from apparent resistivities averaging 400 to values of 2000-3000 ohm-meters which occurs about 10 km. south of Blue River townsite. According to the Canoe River map, this occurs entirely within the Shuswap Complex. North of there, in the Schlumberger region, they generally range from 150 to 450 ohm-meters. At VES 5, they decrease from 350 ohm-meters

at the smallest separation of the 1 km dipoles to 100 ohm-meters at 6 km separation. A general decrease in resistivity with dipole separation is indicated.

At the other large Schlumberger sounding, VES 2, lower apparent resistivities were measured. They average 200 ohm-meters at 1 km separation of the 1 km dipoles and 100 ohm-meters at 2 km separation. At deeper plotting points, apparent resistivities of 27, 28, and 31 ohm-meters were measured. The low resistivity zone in this vicinity appears well substantiated.

The four other Schlumberger soundings were either too far from the dipole-diploe line for correlation, or were not expanded to the point where they would sample depths comparable to those sampled by the diploe-dipole survey.

3-6 Geological-Geothermal Interpretations

Just as the resistivity models constructed from a set of data are nonunique, so are the geological models which fit or explain that set of constructions. However, there is no automatic inversion routine which takes resistivity models as data and produces a geologic model, although the same principles apply. This must be done with geological and geophysical insight. An analogue to the smallest model or perturbation is the simplest geological model. And geological models which incorporate such features as the North Thompson fault, or a heat source may be produced by introducing them as constraints. The principle of nonuniqueness also applies. No unique geological model can be constructed from the finite

number of resistivity models. At best, we will be able to discern the range of geological models which fit our resistivity constructions.

3-6.1 Simplest Model with Geological Constraints

The simplest model is that in which there is no heat source, and the fault has no effect other than to separate the two rock types in one area. This model is only constrained to fit the known geology.

All of the resistivity variations can be explained by the rock types and the grades of metamorphism which they display. Both of the rock groups are thermally metamorphosed everywhere in the survey area, with the metamorphism increasing from south to north. Schlumberger soundings VES 1, VES 2, VES 3, and VES 6 were on glacial deposits overlying the Kaza group of metasediments which is a highly variable group of rocks. Soundings VES 4, and VES 5 are south of the others in the Shushwap Metamorphic Complex with VES 5 lying very close to the fault in the zone where it separates the Shushwap Complex from the Kaza Group.

In the soundings over the Kaza Group, VES 1 is a two layer case suggestive of thick alluvium over the Kaza rock and VES 2 has an average resistivity close to that of the second layer measured in VES 1. VES 3 is also likely alluvium over Kaza, with some lateral variations below 100 meters, and VES 6 is very close to a half space of the same average resistivity seen in the second layer in VES 1. The resistivity level common to all of these is approximately 200 ohm-meters which

therefore seems representative of the Kaza Group.

In the remaining soundings, a more resistive rock with a low resistivity zone at 500 meters depth is indicated. VES 4 however crossed an apparent vertical contact, and VES 5 is close to Kaza rock across the fault. At large electrode separations the currents could leak across the fault and diffuse more easily through the less resistivity Kaza rock on the other side. This would produce the lower voltage readings which caused the low resistivity zone to be constructed. The VES 5 models do approach the resistivity of the Kaza Group at the deepest reliable depths and therefore support this interpretation. (see figures 3.11)

In general, the soundings in the Shushwap showed much higher resistivity levels than those in the Kaza Group. The average resistivities are 900 ohm-meters for the Sushwap and 200 ohm-meters for the Kaza. There is nothing in these constructions which needs to be explained by a heat source because it cannot be by the geology. The effect of the fault is hard to evaluate, but there are three soundings on the fault trace and one (VES 6) shows essentially a half-space response down to a depth of 1 kilometer, so it appears to have very effect there.

The simplest interpretation of the soundings can be summarized as follows:

VES 1 20-25 meters of resistive alluvium over the Kaza Group

VES 2 typical range of Kaza resistivities

VES 3 Kaza Group with a measurable alluvium influence

VES 4 typical Shushwap resistivities with a vertical contact at AB/2=500 meters

VES 5 Shushwap resistivities with current leakage across the fault into the Kaza Group

VES 6 a half-space of typical Kaza resistivities.

3-6.2 Regional Heating Model

Another geological-geothermal model can be constructed using a regional heat flux from the north and high temperatures at depth under the Sushwap Complex to explain some of the low resistivity zones previously attributed to bad data or current leakage. None of the constructions preclude such a model; in fact high temperatures at depth provide quite a plausable explanation for the low resistivity inflections in VES 4 and VES 5. Deeper information from the dipole-dipole line supports this hypothesis by showing decreasing resistivities with depth. This information is only pertinent to the deepest Schlumberger soundings since the minimum dipole separation was 1 kilometer.

The Schlumberger soundings show a trend of decreasing resistivity northward. The apparent resistivity curves shift lower at each site when considered from south to north. On the dipole-dipole line, the average apparent resistivity drops abruptly at all depths about 10 kilometers south of Blue River, and remains at that lower level to the northern end of the line. This drop could signify the southern extent of heat

flowing from a source to the north and the Schlumberger soundings may be showing a north-south temperature gradient.

Schlax and Shore (1981), hypothesized that the pattern of alternating higher and lower resistivity zones on the pseudo-section in this region represents upwelling and downgoing brine circulating in convection cells. The upwelling brine would be hotter and therefore less resistive than the downgoing.

High temperatures at depth are a possible explanation for the two soundings which show indisputable low resistivity zones at large AB/2 spacings, VES 4 and VES 5. Both are in the Shuswap Complex and are therefore more resistive than the others down to about 200 meters for VES 4 and 300 meters for VES 5. At these depths the resistivities begin to drop. In VES 4, this was explained by a vertical contact, however, the geology map shows no rock boundary or facies change there (Canoe River 15-1967). And, in VES 5, the explanation was current leakage into the less resistive Kaza Group. Noting that the resistivity starts dropping when AB/2=300 m, where it would be uninfluenced by the fault, the temperature gradient explains this feature better. In addition, the northernmost of the two soundings, VES 5, is approximately 400 ohm meters less resistive than VES 4 in the top 200 meters which supports the heat from the north interpretation.

The Shuswap Complex is known to be less altered thermally and structurally than the Kaza Group; it displays only Silimanite zone metamorphism. Since it is not so fractured, high temperatures at depth would not be expected to produce a

low resistivity zone which extends up to the surface. The dipole-dipole data support the existence of a low resistivity zone below 1000 meters, and therefore support the high temperatures at depth hypothesis.

Over the 30 kilometer north-south span of the soundings, two things are for certain: The first is that the Shuswap Complex is more resistive, at least at shallow depths, than the Kaza Group, and the second is that the Kaza Group becomes generally less resistive to the north (see figure 2.13). These two observations suggest a regional heat source to the north. The high temperatures in the Shuswap Complex could be plunging isotherms from the northern heat source, or could be related to something entirely different.

The regional heating model can be summarized as follows: (The soundings are arranged from south to north.)

VES 4 cold Shuswap rock down to approximately 300 meters where the temperature begins to increase.

VES 5 low resistivity zone at 500 meters signifying high temperatures at that depth.

VES 1 very resistive alluvium over a warm Kaza basement.

VES 6 half-space of warm Kaza rock

VES 3 an alluvium layer over warmer Kaza rock

VES 2 northernmost sounding and the lowest resistivity values, closest to the heat source.

3-6.3 The Most Probable Model

It is unlikely that either the simplest model or the regional heating model is entirely correct. The most probably correct model is one which combines the most plausable explanations from each and uses them, along with the geology of the area, to complete the geological-geothermal picture. This defines the most probable model. Given the Schlumberger data and the volcanic history of the area, we have significant evidence for regional heating from the north. We also see a large relative difference in resistivity between the two major rock groups in the area with the Kaza being the less resistive of the two.

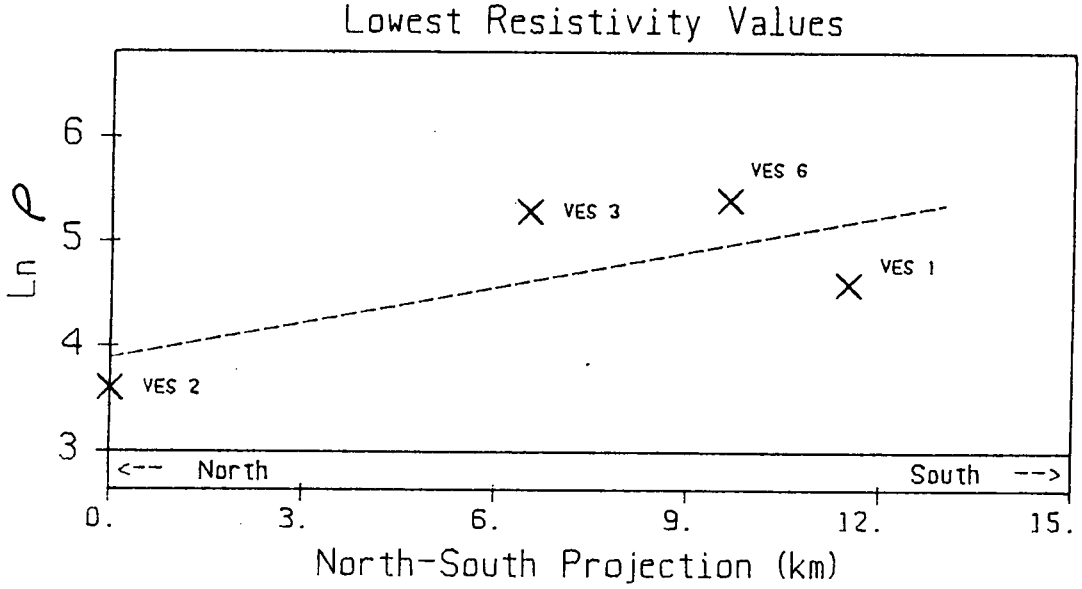

Figure 3.13 This graph shows the lowest resistivity values constructed from the soundings in the Kaza Metasediments. They are plotted against distance south of VES 2, which was the northernmost sounding. The gradient seen here forms the basis of the heat-from-the-north model. The least squares fit to the points has the following formula: $\rho = \exp(3.9 + 0.11x)$ ohm-meters where x is the distance south of VES2 in km.

The North Thompson fault must play a role in producing the measurements because of the enormous vertical displacement that has occured along it. Fault signatures usually manifest themselves with low resistivities resulting from increased porosity. Thus, VES 5 may have been affected by the fault

zone itself, rather than the rock on the other side, or high temperarures. It is indeed unfortunate that the valley bottom, which provides the deepest vantage point also contains such a large fault.

The low resistivity zone indicated on VES 4 is also of questionable reliability. When the data points which violate the slope rule are omitted, the existence of the low resistivity zone hinges upon only one data point. Unfortunately the dipole-dipole line is too distant for correlation, so this low resistivity zone cannot be substantiated.

Without the low resistivity zone on VES 4, and explaining the low zone on VES 5 by the fault itself, there is only evidence for regional heating from the north. Since every sounding contributes to this hypothesis, and it is supported by their average resistivity levels rather than inflections, heat flowing from a source to the north is the most probable model.

3.7 Correlation with the Larger Scale Tectonic Picture

A geological overview of the Anahim volcanic belt and its relationship to the west coast tectonic picture will be presented with the intention of putting our most probable model into its proper perspective. Its "fit" into the large scale hypotheses, or models, concerning the genesis of the Anahim volcanic belt will then be examined.

3-7.1 Geological History of the Anahim Volcanic Belt

The Anahim volcanic belt is composed of a wide variety of extrusive and plutonic features. Extrusive features range from small basaltic cinder cones to huge peralkalic[1] shield volcanoes, and the plutons include dike swarms and subvolcanic plutons (Baer, 1973). From the relative positions of lavas at many volcanic centres, Souther (1977) concluded that most of the basaltic magma rose to the surface quickly through small conduits forming the many small single-eruption volcanoes. Only in places where the magma pooled and melted out a chamber did any differentiation occur. These gave rise to large strato-volcanoes one of which, the Rainbow Range shield volcano, has been investigated isotopically for age information (Bevier et al. 1979). The last eruption there was 8.7 million years before present (K-Ar detemination). This is approximately in the middle of the range of ages found in the Anahim belt which is from 14.5 million years to 10 thousand years before present.

In the late Miocene, at the time of the earliest eruptions in the Anahim, the plate orientations off the west coast were similar to today although the Explorer Plate may not have moved independently at that time. The Juan de Fuca, and Pacific Plates were separated by a spreading ridge, as they are now, and the Juan de Fuca Plate was being subducted under the North American Plate while the Pacific Plate moved

---

[1]Peralkalic igneous rocks are those in which the molecular proportion of Al is less than that of Na and K combined.

north. A right lateral transform fault separates it from the North American Plate (see figure 3.14). The triple junction formed where this spreading ridge meets the North American Plate is known to have jumped around during the last 10 million years (Riddihough and Hyndman, 1976), making reconstruction of the plate positions back to 10 million years before present very difficult. But Riddihough (1977) has placed the triple junction off Brooks Peninsula on Vancouver Island during the period from 5 to 10 million years ago. It was during this time that the Alert Bay volcanoes on the northern end of Vancouver Island became active. (see figure 3.14)

Subduction of the Juan de Fuca Plate under the North American Plate resulted in arc and back arc volcanism, and the Anahim belt, according to Stacey (1974). The Pemberton and Garabaldi volcanic chains are examples of arc volcanism. (see figure 3.14) These were not active simultaneously, however, and activity shifted from the Pemberton chain, which is further inland, to the Garabaldi chain about 2-3 million years ago (Bevier et al. 1979). The Alert Bay volcanoes also became extinct at this time. Riddihough (1977) proposed a tectonic cause for these changes: the reorientation of the Explorer Plate, and subsequent changes in the subduction of the Juan de Fuca Plate. The triple junction was moving north at this time.

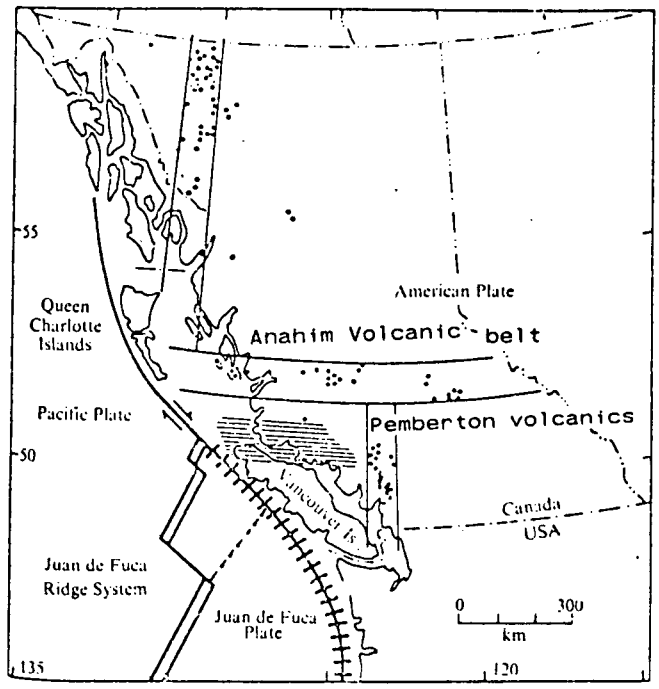

Figure 3.14 Plate boundries and volcanic belts. This shows the orientation of the Juan de Fuca Plate in relation to the Anahim volcanic belt. The present boundry between the Juan de Fuca, and Explorer Plates is shown with a dashed line, and arrows indicate relative plate motions. (from Stacey, 1974)

The Anahim volcanic belt lies just north of the subducting limb of the Juan de Fuca Plate. Stacey (1974) used this relationship and physiographic evidence to arrive at his edge effect hypothesis for the origin of the belt. In this hypothesis, the lithosphere is forced up by the underthrusting Juan de Fuca Plate and flexes where it overlays the northern end of the subduction zone (see figure 3.15). Tension created by the flexure would cause cracking at the base of the lithosphere, and hot mantle material could melt its way to the surface as the cracks opened. Over the flexure zone, chain of volcanoes would ensue. For this mechanism to have activated the Anahim volcanic belt, the Juan de Fuca Plate would have to

underthrust the North American Plate far inland before sinking. At the estimated convergence rate of 2.5 cm/yr in the direction N 35°E, (Atwater, 1970) it would take 24 m.y. for a zone of tension to propagate from the coast to the present eastern edge of the Anahim volcanic belt. As the age difference between the volcanoes in the east and those in the west is 14 m.y., the two time scales do not fit very well. Furthermore, the Anahim belt lies east-west, not N 35°E. (see fig 13.4)

Another hypothesis attributes the Anahim volcanic belt to north-south rifting of the North American Plate (Tipper, 1957, 1969). This theory arises from the common association of Alkalic, and Peralkalic volcanic rocks with tensional environments. However, the lack of extensive east-west normal faulting makes this theory the least credible. The North Thompson fault, because of its north-south orientation makes north-south rifting in the eastern end of the Anahim quite unlikely, and this theory lacks an intrinsic explaination for the trend of decreasing ages seen in the Anahim volcanic belt.

The most favored hypothesis is one which explains the Anahim belt as the trace of a mantle hot-spot over which the North American Plate has been drifting. Strontium isotope analysis of the lavas from the large Rainbow Range Shield Volcano indicates that they originated in the mantle (Bevier et al. 1979). The peralkalic lavas which are found in volcanic centres and roots of shield volcanoes are believed to be a result of fractional crystalization of basaltic magma beneath the large volcanoes.

Further support for the hot-spot theory is contained in Minster's 1974 results for the instantaneous velocities of the major plates. In this investigation, 106 earthquake motion vectors, 68 spreading rates, and 62 fracture zone trends were inverted to obtain the instantaneous velocities. Their solutions were self-consistent; integrating the velocity vectors over any closed path on the surface of the earth returned zero net motion, as it should.

The drift rate Minster et al. obtained for the North America Plate was 2.7 cm/year relative to the mantle hot-spots beneath Yellowstone Park and Raton, New Mexico. Using the gradation in ages and assuming a stationary hot-spot under the Anahim belt, Bevier (1979) calculated a mean drift velocity of 2-3.3 cm/year. Minster's work also uses the global hot spot distribution as a stationary reference.

Still more convincingly, the east-northeast trend of the Anahim volcanic belt at lattitude 52.5° lies along a small circle of Minster's hot spot - North America pole at 48.1° north and 97.9° east. The velocity predicted at the centre of the Anahim volcanic belt is 2.5 cm/year, which is within the range of velocities indicated by the progression of ages. Thus the mantle hot spot hypothesis seems to have the most evidence supporting it, but there is insufficient evidence to rule out the other hypotheses.

We now look to our most probable model to see whether one theory is supported over the other by the resistivity data, as unfolding some of the geologic history was one of the aims of the Anahim resistivity survey.

3-7.2 Fit to the Hot-Spot Trace Hypothesis

A heat source to the north of the survey area was called for in the most probable geological-geothermal model. It would create a south-north temperature gradient in the survey area which could account for the northward decrease in resistivity.

According to the hot-spot hypothesis, the Anahim belt is the trace of a mantle plume which the North American Plate has been drifting over. It is hypothesized to lie under the eastern section of the belt at present. If this plume is taken to be the heat source called for, then the most probable model easily fits into the hot-spot hypothesis. Descriptively, they support each other.

Quantitatively though, there is not enough resistivity or temperature data to verify the fit. If more measurements were available, then the support could be evaluated by checking their fit to the temperature distribution function expected from the hot-spots geometry. Heat flowing from a long column of magma in the lithosphere would have circular symmetry, falling off as a function of the distance from the centre of the column. The theoretical temperature distribution could be modelled by solving the heat equation on the top of a semi-infinite solid with a cylindrical heat source. Then, the hot-spot hypothesis could be tested by comparing the predicted temperatures to those measured, or derived from resistivity measurements.

3-7.3 Fit to the Edge Effect Hypothesis

Stacey's (1974) proposed mechanism attributes the Anahim volcanic belt to cracking at the base of the lithosphere over the northern end of the subduction zone. The following diagram illustrates this hypothesis.

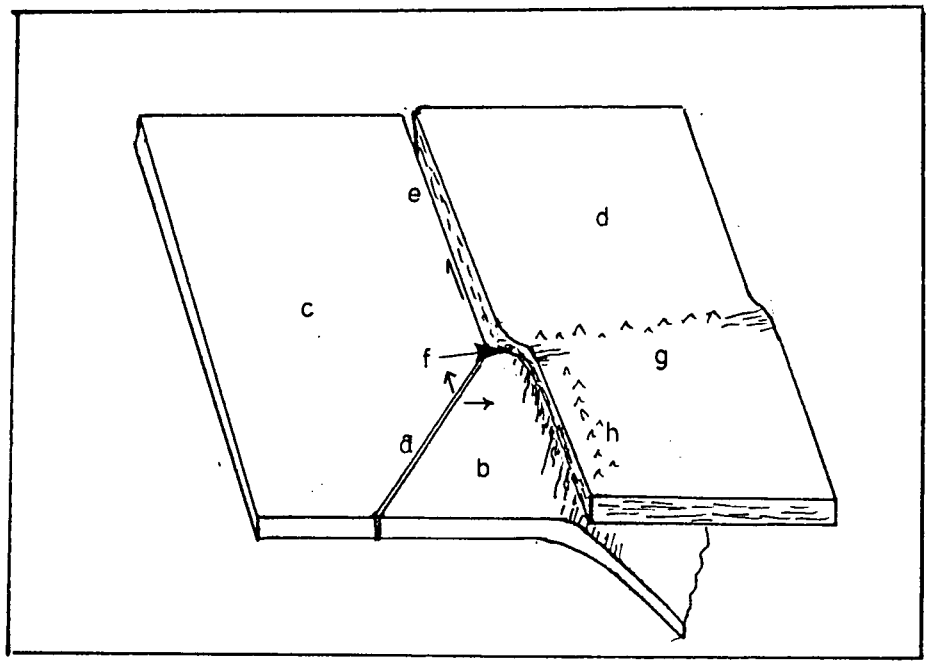

Figure 3.15 the mechanism for Stacey's edge effect hypothesis. a:spreading centre, b:Juan de Fuca Plate, c:Pacific Plate, d:North American Plate, e:Queen Charlotte transform fault, f:zone of tension, g:Anahim volcanic belt, h:coastal volcanic arc.

The heat flow from such a mechanism would be substantially greater than from a single hot spot, and the volcanism more active. Surface temperatures would decrease with lateral distance from the edge of the slab, and near surface resistivities would increase.

Our resistivity constructions do show an increase in the

average resistivities going from north to south which could be the result of decreasing temperature (see figure 3.13). However, with the soundings lying roughly along one line, it is impossible to gather support for an edge effect source from them.

Again, a quantitative approach could be taken if the data warranted it. By modeling the temperature distribution that results from the edge effect heat geometry, and checking the fit to actual measurements, some evidence, either for or against the theory could be obtained. Before such an analysis is carried out, a reliable resistivity to temperature conversion for rock of the Kaza Group should be developed.

In summary, the resistivity models constructed in this chapter support either hypothesis for the origin of the Anahim volcanic belt. There is not enough information in the six resistivity models to support one hypothesis over the other. That could only come from a more detailed experiment.

CHAPTER 4

APPRAISAL

Once a chi-squared acceptable model has been constructed, regardless of the method, it should be appraised. We should know which features of the model likely exist in the real earth, and which are merely artifacts of the construction method. This is especially important for those features which are of high interpretive value in a large scale geological interpretation. We want to be as certain as possible that the earth actually has the structures which form the basis of any such interpretation.

4-1 OBJECTIVES OF APPRAISAL

Models which fit a set of resistivity data, or most other types of geophysical data for that matter, can usually be constructed by a number of different methods. Here, resistivity models have been constructed with the smallest and flattest perturbations in linearized construction, but other methods also exist. Gel'fand-Levitan procedures and modified Dar-Zarrouk functions have also been used to construct resistivity models and, there are different norms to minimize both globally and locally within the realm of linearized construction. In each case different models will be produced. This presents the following dilema: with such a range of models possible, what certainty can we have that a single acceptable model bears any resemblence to the real earth? Very little, it would seem from the number of models that can be constructed, but this should be qualified.

Qualifying the degree to which the constructed models are similar to the real earth model is the object of appraisal. In effect, appraisal is the error analyis of constructed models.

4-2 Linearized Appraisal

Until recently, Backus and Gilbert's linearized approach to appraisal was considered adequate for the nonlinear problems. It is now known, however, that its ability to successfully appraise a model depends upon the validity of the assumption that all the models which fit a set of data are linearly close[1]. By implication of this assumption, the true earth model is linearly close to any data-fitting model. The problem with this approach has recently been illustrated in the case of magnetotellurics, where acceptable models have been constructed from delta function conductances (Parker, 1981) which are not linearly close to either the real earth, or previously constructed models. Linearized appraisal of continuous models had said nothing about the existence of these; they are not linearly close to continuous models. In fact, linearized appraisal does not extend to any models very different in their gross features from the one being appraised.

One conclusion that may be drawn from this, is that the first step towards a comprehensive appraisal should be the

---

[1]The term linearly close will be defined in section 4-2.1

collection of as many varied models as is possible. Then, if all the models are linearly close, one may proceed with linearized appraisal. If not, the appraisal must be done qualitatively. But even if all the collected models were linearly close, there would still be no guarantee that all acceptable models were.

Some solace may be found in the fact that over a one-dimensional earth, there is a uniqueness theorum for resistivity measurements (Langer 1933). This very fortunately implies that as the number of data increases, the structure will become better determined to the limit where infinite accurate data will uniquely determine the real earth's resistivity structure.

4-2.1 Averaging Functions and Model Averages

Backus and Gilbert's linearized method for appraising models in the non-linear problems such as D.C. resistivity and M-T will now be presented. The inherent assumptions, and the conditions under which they are true will also be discussed.

It will be assumed that a chi-squared acceptable model $m_0(z)$ has already been found. Now, by Fréchet differentiability of the data, there exists the function $Gi(m_0(z),z)$ such that if $m_1(z)$ is any other earth model, then

$$Ei(m_1)-Ei(m_0) = \int_0^\infty Gi(z)[m_1(z)-m_0(z)]dz + O[(m_1-m_0)^2] \quad \text{for } i = 1,n \qquad (4.1)$$

where $Ei(m_1)$ and $Ei(m_0)$ are the i'th data predicted by the respective models, and $O[(m_1-m_0)^2]$ is a quadratic remainder term.

When m_1-m_0 is sufficiently small, as measured by a L_2 norm, the quadratic term goes to zero and the difference in data depends almost linearly upon m_1-m_0 (Backus and Gilbert, 1968). The region in model space where this is true is called the linear region around m_0, and the models in this region are said to be linearly close to m_0. It is intuitively obvious that the size of the linear region is dependent upon the relationship between Ei and m. If the relationship is linear over all of model space, then we are back to a linear problem. The kernel, Gi(m(z),z) embodies this relationship through its m(z) dependence in the following way. A kernel which has no dependence upon m(z) is representative of data which are linear in m(z), and in non-linear problems, the region around $m_0(z)$ where Gi(m(z),z) is constant with respect to m(z) is the linear region. Thus, the difference between the kernels of two models which fit the data could possibly be used as a measure of linear closeness.

Assuming that both models fit the data, and are linearly close so that the remainder term is much smaller than the difference in data, we have then to the first approximation

$$\int_0^\infty Gi(z)\ [m_1(z)-m_0(z)]\ dz \;=\; 0 \qquad i=1,n \tag{4.2}$$

which can be separated into two equivalent integrals.

Equality is maintained when the integrals are multiplied by the coefficients a_i which minimize the difference between $\sum_{i=1}^{n} a_i G_i(z)$ and $\delta(z-z_0)$, and we obtain

$$\int_0^\infty A(z,z_0)m_1(z)\,dz = \int_0^\infty A(z,z_0)m_0(z)\,dz \qquad (4.3)$$

where

$$\sum_{i=1}^{n} a_i G_i(z) = A(z,z_0),$$

and $A(z,z_0)$ is the averaging function centred at z_0. The models as seen through the averaging functions are equal, and the only conditions on $m_1(z)$ were that it fits the data, and that it is linearly close to $m_0(z)$. Models satisfying these conditions will have identical averages at any point z_0 in their range.

$$\langle m_1(z_0)\rangle = \langle m_0(z_0)\rangle \qquad (4.4)$$

Average models can be constructed point by point to determine what features all of the linearly close models have in common. Or, the averaging function itself can be constructed at depths of interest to determine over what range of depths the model is averaged. This provides a way of visualizing the depth resolution of a model.

To obtain information about the real earth, though, from linearized appraisal we must know unequivically that the model $m_0(z)$ is linearly close to the true earth model $m_e(z)$. Then, and only then, will averages of the constructed model equal true earth model averages. It is here that the problem with

linearized appraisal lies. Where it was previously thought that all acceptable models were linearly close to each other and the true model, it has been shown to be false.

Recent evidence has shown that in the M-T problem, all acceptable models are not linearly close to each other. Parker (1981) has constructed models for M-T data comprised of a set of Dirac-delta function conductances, where a continuous model had also been found acceptable. The implication that this carries over to D.C. resistivity is that the real earth cannot be guaranteed linearly close to a certain constructed model. As a result, model averages may not convey any information about the real earth structure.

If the constructed models $m_1(z)$ and $m_0(z)$ fit the data, but are not linearly close, the quadratic term $O[(m_1-m_0)^2]$ will not be negligible compared to $Ei(m_1)-Ei(m_0)$, and equation 4.2 will be invalid. Therefore, different model averages will generally result when the models are seen through averaging functions formed from either set of kernels. In general,

$$\int_0^\infty A(z,z_0)m_1(z)\,dz \neq \int_0^\infty A(z,z_0)m_0(z)\,dz \qquad (4.5)$$

where either

$$\sum_{i=1}^{n} a_i Gi(m_0,z) = A(z,z_0)$$

or

$$\sum_{i=1}^{n} a_i Gi(m_1,z) = A(z,z_0)$$

In these cases, linearized appraisal may not reveal what features a constructed model has in common with the real earth.

Used with a different intent though, linearized appraisal

can furnish some useful information. It can tell us what features on a constructed model are not guaranteed to exist in the real earth. Thus, by linearly appraising specific features on a constructed model, we can determine whether or not they are common to all linearly close models. If they are not, then they are two stages removed from being features in the real earth, and should not be pivotal in any physical interpretation of the model. Features which do pass this test can be considered more reliable, although there is still no guarantee that they exist in the real earth. This approach will be taken here.

4-2.2 Deltaness Criterion

For a perfectly resolved model, the averaging functions would be delta functions centred over the depths of interest, and constructed model values would be returned as the average model. Owing to the limited number of data, however, and the resolving power of the Fréchet kernels, only approximations to delta functions can be achieved. Often too, the averaging functions cannot be centred over the region of interest. So in practice, constructing an averaging function amounts to finding the set of coefficients which, when multiplied by the kernels and summed together, gives the best averaging function possible under the circumstances – subject to the condition that the area under it is unity.

Several criteria exist for comparing an averaging function to a true delta function, and the alpha coefficients are chosen so as to minimize the difference between the two

according to one of these criteria.

In the Spread criterion of Backus and Gilbert, an averaging function's narrowness, subject to the unit area condition, measures its similarity to a delta function. To construct averaging functions with this criterion, the width is minimized while the area is constrained to be one. Functions obtained in this way generally have no negative sidelobes, unlike those obtained using other criteria. The spread of an averaging function is defined as:

$$S(A) = 12 \int_{0}^{\infty} (z-z_0)^2 A(z,z_0)^2 dz \qquad (4.7)$$

If $A(z,z_0)$ is a box-car function, of height $1/w$ and width w, the spread is then also w.

by symmetry,
$$w = 24 \int_{z_0-\frac{w}{2}}^{z_0} (z-z_0)^2 \frac{1}{w^2} dz \qquad (4.8)$$

The $(z-z_0)^2$ term heavily weights any area under the averaging function away from its intended centre. Thus, a sharp averaging function displaced from its intended position will have a large spread, just as a wide one will.

In the First Dirichlet criterion, the squared difference between the averaging function and a true delta function centred at z_0 is taken as the measure of deltaness. The alpha coefficients which minimize the two-norm of this difference will contruct the optimal averaging function according to the First Dirichlet criterion.

$$\psi = \int_0^\infty \left[\sum_{i=1}^{n} a_i \mathrm{Gi}(z) - \delta(z-z_0)\right]^2 dz \qquad (4.9)$$

Minimizing this difference would seem to be a more direct way of constructing an averaging function than using the Spread criterion, but it often produces functions with negative sidelobes around the main peak (see Backus and Gilbert, 1968, Appendix B, figure 4.1). An averaging function without negative sidelobes is more easily interpreted, as it graphs the relative importance of the model at every depth to the average model. Furthermore, negative sidelobes could conceivably produce a negative average model, which in the case of resistivity would convey no meaning other than poor resolution. Offsetting this disadvantage though, is the empirical finding that First Dirichlet criterion averaging functions are often narrower than Spread criterion averaging functions. So, the choice of deltaness criterion used is truly a subjective one.

Another deltaness criterion seeks to minimize the difference between a Heavyside function set at z_0, and the indefinite integral of $A(z,z_0)$. This is the Second Dirichlet criterion. Theoretically, there are as many criteria as there are ways of approximating delta functions, and they could all be employed to construct averaging functions. Only the Spread criterion will be used here, however, in our appraisal of the Schlumberger models.

4-2.3 The Tradeoff Between Resolution and Accuracy

The presence of errors in the data makes appraisal more complicated than has been described thus far. Sources of error, which are discussed in section 2.3, are everpresent in geophysical experiments so a method for accomodating the errors which arise must be built into linearized appraisal. In their 1970 paper, Backus and Gilbert allow for the presence of errors in the data and develop the idea of the tradeoff curve. They show that when a model is being appraised, some sacrifice in the resolution of a model average will often be desirable to bring down the variance associated with it.

If errors ΔEi, $i=1,n$ were made in measuring the data, and a model which fit those erroneous data, while being linearly close to the real model was constructed, then the error introduced to the model average is:

$$\Delta\langle m_e(z_0)\rangle = \int_0^\infty \sum_{i=1}^{n} a_i Gi\,[m_0(z)-m_e(z)]\,dz. \qquad (4.10)$$

The error in a model average is thus the a combination of the measurement errors.

$$\Delta\langle m_e(z_0)\rangle = \sum_{i=1}^{n} a_i \Delta Ei$$

since

$$\Delta Ei = \int_0^\infty Gi\,[m_0(z)-m_e(z)]\,dz. \qquad (4.11)$$

Of course the data errors themselves are never known, although

through repeated measurements, their statistics may be learned. It will be assumed that they are random, and follow a Gaussian distribution with zero mean. It will be further assumed that the errors in the i'th datum are independent of those in the j'th datum.

We are assuming:

1. The errors have zero mean; $\Delta Ei = 0$, for i=1,n.
2. The covariance matrix of ΔEi and ΔEj is zero except on the trace. So,

$$Eij = \overline{\Delta Ei \Delta Ej} = \delta_{ij}\ \sigma_i^2$$

where σ_i^2 is the variance of the i'th measurement.

Knowing the covariance matrix, the variance in the model average can now be expressed.

$$\mathrm{var}\langle m_e(z_0)\rangle = \sum_{i,j=1}^{n} a_i\ a_j\ E_{ij} \qquad (4.12)$$

Thus, both variance in the data, and the alpha coefficients determine the variance in the model average.

If the coefficients which maximize deltaness are chosen without regard to the variance which they dictate, the variance may be so large that the model average is highly uncertain. In order to reduce the variance, we must be prepared to accept a less delta-like averaging function. Resolution, as controlled by the averaging function, and accuracy, as expressed by the variance, are mutually antagonistic qualities in the appraisal of models.

If having a small variance is prefered to having good resolution, the coefficients which minimize variance should be found, and if good resolution is desired, then the coefficients which maximize deltaness should be found. However, one quality will always be sacrificed for the sake of the other. There are parallels between this phenomenon and the Heisenburg uncertainty principle.

Backus and Gilbert's tradeoff curve relates the averaging function's width to the variance in a model average at a particular depth (Backus and Gilbert, 1970). The curve is plotted on axes of model variance, and spread. To construct the tradeoff curve at the depth z_0, spread and variance are weighted according to whichever we are more desirous of minimizing and both minimized. The area under the averaging function must be constrained to be one to exclude the $a_i=0$ solution for i=1,n, which gives zero width, and zero variance. This condition is added through a Lagrange multiplier λ. The resulting objective function is then minimized and the resulting spread and variance values are coordinates of a point on the curve. By changing the weighting continuously the whole curve is swept out. This is done by multiplying the spread term by $\cos\theta$, and the variance term by $\sin\theta$, and varying θ from 0 to $\pi/2$. The objective function is then:

$$\psi = \text{spread}(\cos\theta) + \text{var}\langle m(z_0)\rangle(\sin\theta) + \lambda \text{ unimodularity constraint} \quad (4.13)$$

Spread or variance can be minimized independently by setting θ to 0, or $\pi/2$ respectively. Most often though, some tradeoff

of width is made in order to bring the variance down to an acceptable level when constructing an average model.

For averaging functions constructed using the spread criterion, the objective function is:

$$\psi = \cos\theta \sum_{i,j=1}^{n} a_i a_j \Gamma_{ij} + W \sin\theta \sum_{i,j=1}^{n} a_i a_j E_{ij} + \lambda\left(1 - \sum_{i=1}^{n} a_i \int_0^{\infty} Gi(z)dz\right) \quad (4.14)$$

where

$$\Gamma_{ij} = 12 \int_0^{\infty} (z-z_0)^2 Gi(z)Gj(z)dz,$$

and λ is the Lagrange multiplier, and W is a constant which helps theta to vary uniformly along the tradeoff curve. The actual minimization is done by differentiating ψ with respect to a_i and λ to find the minumum with respect to the alpha coefficients and λ.

Now the features in the Schlumberger constructions which our heat-source-to-the-north hypothesis was based upon will be appraised.

4-3 Linearized Appraisal of some Schlumberger Constructions

In Chapter 3, resistivity models were constructed from data taken in the Anahim Volcanic Belt and temperature information was interpreted from them. Three geological-geothermal models for explaining the temperature distribution were inferred from the models and described. The most probable model called for a heat source to the north of the area where the soundings were taken. Evidence for the heat source to the north hypothesis comes from a general trend of

decreasing resistivity to the north. This shows up on all six models, but only in the northernmost four, all in the Kaza Group, is it interpreted as being very significant. (figure 4.1) The low resistivity zones which determine this trend will be linearly appraised.

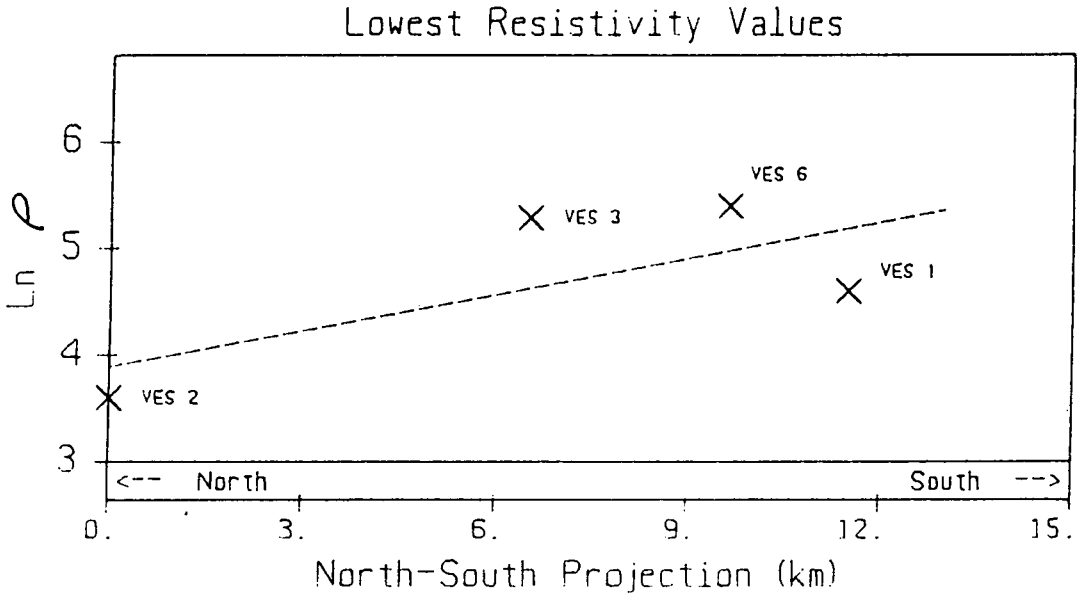

Figure 4.1 North-south resistivity gradient of the constructed models in the Kaza Group. The existance of this gradient depends heavily upon the resistivity low on the VES 2 model. It therefore must be appraised.

The model most important to the hypothesized resistivity gradient is VES 2. Without its low resistivity zone, there would be scant evidence for a trend at all. It is therefore important to the hypothesis that this zone should pass linearized appraisal by being present on average models.

First, a tradeoff curve will be constructed in this low resistivity zone to qualify the interrelation of spread and variance there. Then, the maximum acceptable variance for resolving this low zone will be determined from the constructed model (figure 4.3a). An average model will be

constructed by plotting model averages, each having that variance, at many depths. Each point on this model will have a known standard deviation, and if the low resistivity zone cannot be nullified by two standard deviation error bars, it will be called resolvable.

The tradeoff curve was constructed at the depth of 150 meters (figure 4.2). It decreases monotonically from a variance of 63 with a spread of 81 meters at θ=0.0, to a variance of 0.0007, and a spread of 377 meters at $\pi/2$. The model average increases monotonically as θ —> $\pi/2$ from $\ln(\rho)$=4.0 to $\ln(\rho)$=4.8. As the averaging function gets wider, it samples the flanks of the low resistivity zone as well.

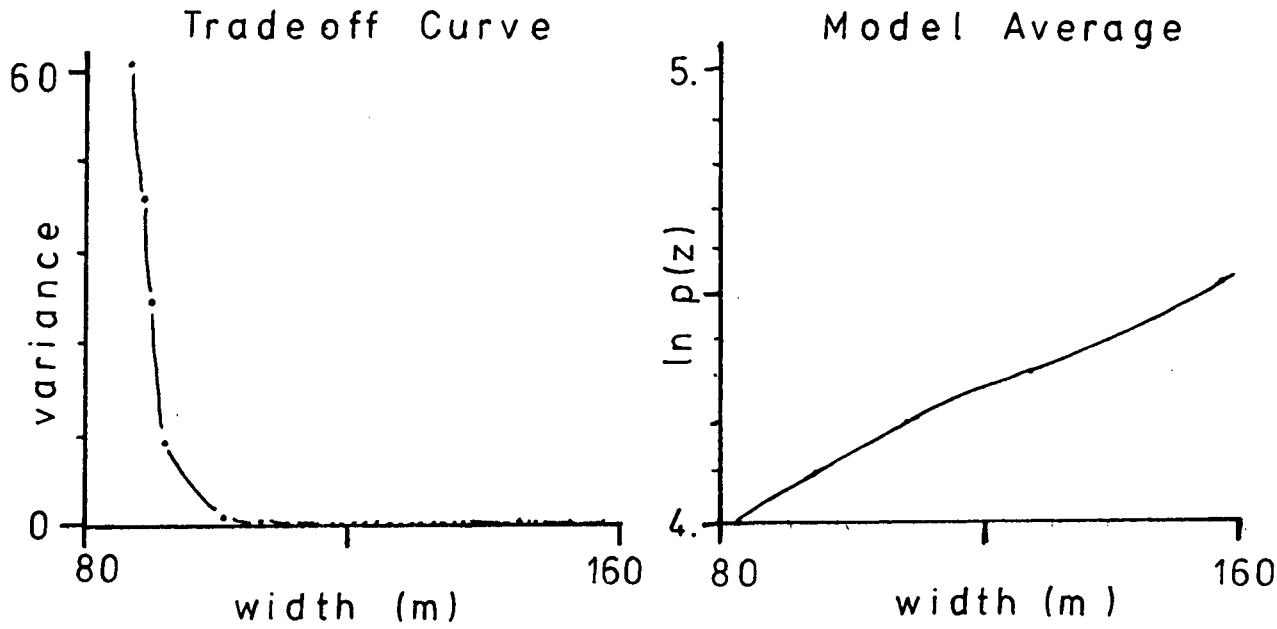

Figure 4.2 Tradeoff curve and average model for VES 2 at 150m. The tradeoff curve does not include the points at $\theta = \pi/2$ because the spread is so large. Instead it shows the curve for $0.0 < \theta < 1.55$.

The amplitude of the resistivity low on the VES 2 model is at least one logarithmic unit. Therefore to rigirously appraise it, it should be unequivocally present on the average model having a two standard deviation level of 0.5. This means a variance of 0.0625 for every point. When the model is computed, we see that this is borne out.

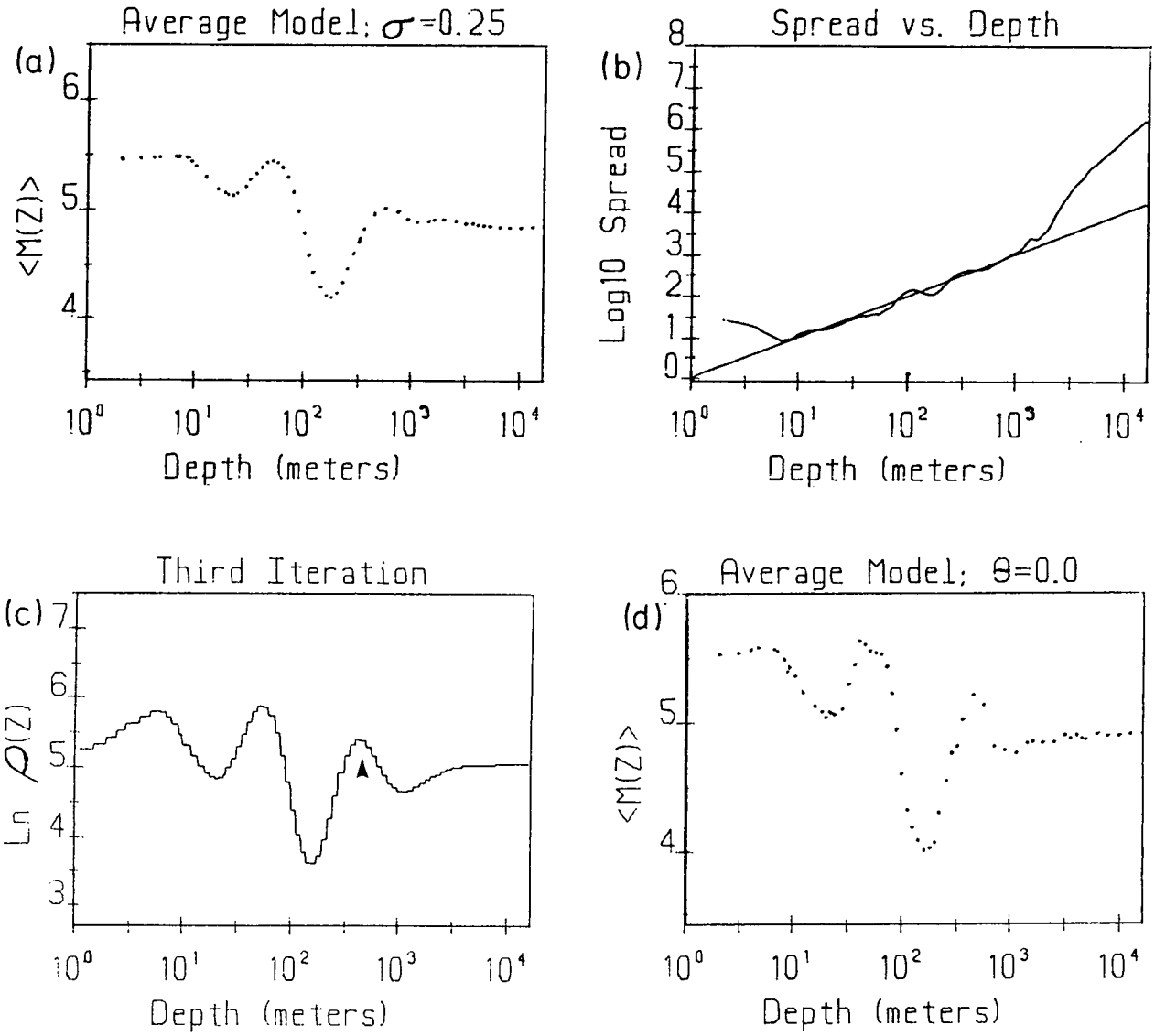

Figure 4.3 a) Average models for VES2. Each point has a standard deviation of 0.25 associated with it. Even at the two standard deviation level, the low zone is resolvable.
)b Spread as a function of depth for each of the points on the average model. Notice how it leaves the s = z line at around 1000 m.
)c Smallest perturbation constructions for VES 2.
)d Average model constructed at θ = 0.0. Each point has an unknown variance.

The low resistivity zone is present on the average model, even if the errors were at the two standard deviation level (figure 4.3a). The width of the Spread criterion averaging function at this variance is also shown as a function of depth. This plot can be used to decide below what depth the model has lost its resolvability and contains no more useful information. Certainly when the spread is much greater than the depth at which it is calculated, the averaging function is not localizing information, and the model average looses its meaning. The line where the spread equals the depth has been plotted for comparison.

Comparing the σ=.25 model to the θ=0 model, little resolution appears to have been lost in sliding down the tradeoff curve to this point. More imporantly, the standard deviation of each point on the σ=.25 curve is known, and the low resistivity zone is the major feature on both models.

It is interesting to note that the third dip in resistivity shown on the smallest perturbation construction for VES 2 (figure 4.3a) is not included in the σ=0.25 average model, and is only hinted at at in the θ=0.0 average. It is therefore not resolvable and is not common to the linearly close models.

At the southern end of the Kaza Group there were three closely spaced Schlumberger soundings, VES 1, VES 3, and VES 6. Here, appraisal is less important to the heat hypothesis for two reasons. Firstly, the common resistivity value below 50 m is substantiated by three models, and secondly, the VES 6 model is essentially a half-space of constant resistivity, so

that data point on figure 4.1 does not rely upon resolution for its resistivity value. Nevertheless, the VES 1 model constructed from a half-space will be appraised to determine the resolvability of its major low.

A two standard deviation level of 0.6 at every point would suffice for resolving this major feature. Thus, model averages having a variance of 0.09 were computed and plotted in figure 4.4. The average model obtained verifies the resolvability of the this low resistivity zone.

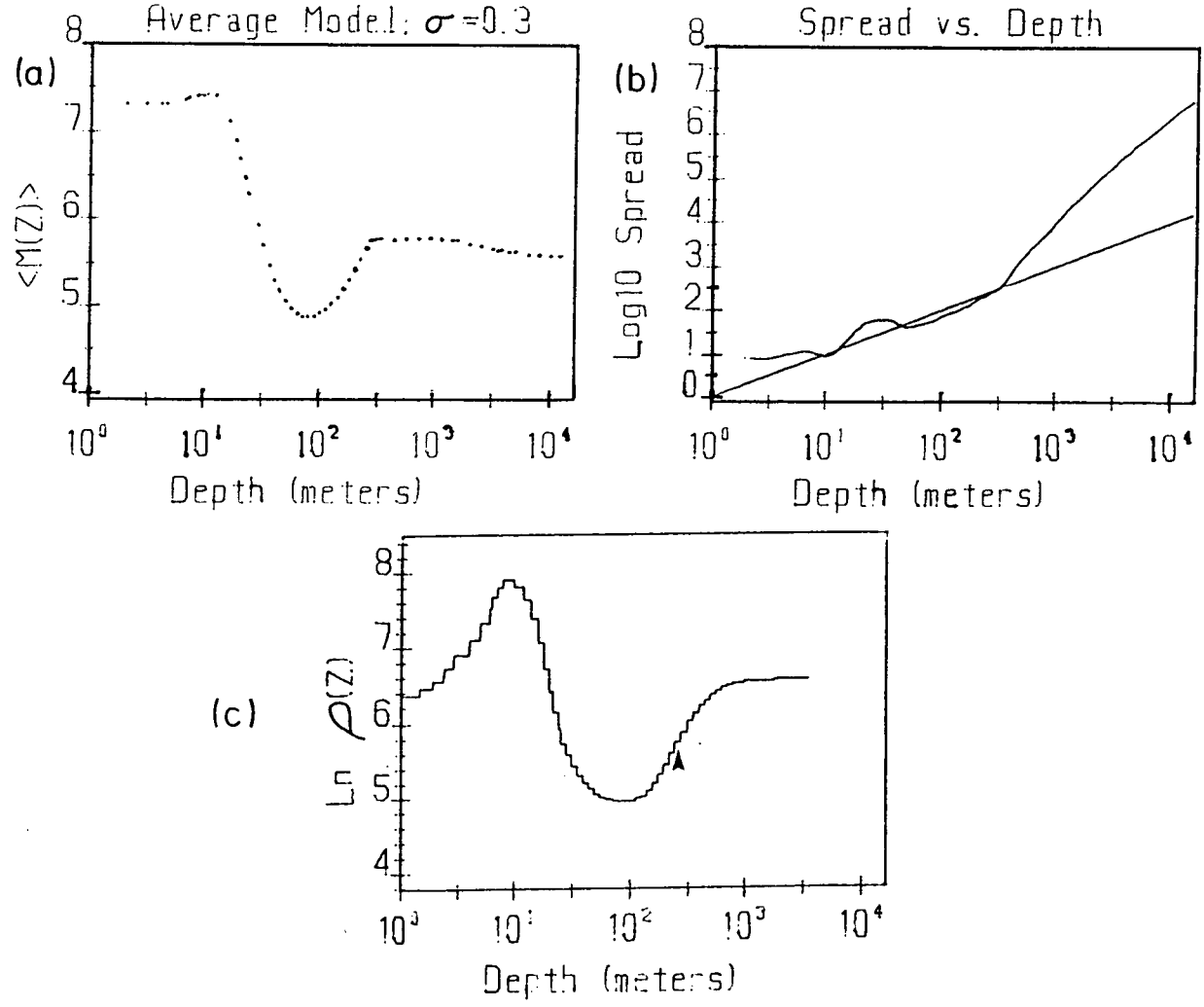

Figure 4.4 a) Average model for VES 1. The low resistivity zone has an amplitude greater than the 2 standard deviation error bars. The two standard deviation level is 0.6.
b) Spread of the averaging functions. This shows that good averaging functions can be constructed down to 500 meters depth.
c) Smallest perturbation construction for VES 1 from a half-space.

The structures which determine the resistivity gradient have been verified as resolvable. The low valves on VES 1. are the major feature on the average models, and in VES 2, the low is also strongly present, so we have not lost any evidence for the resistivity gradient, or the heat-source-to-the-north explanation for it.

Although the most probable model interpretation does not rely on VES 5, it was appraised too. The interesting outcome was that the average models showed a simple structure having fairly high resistivity down to about 200 meters. This is clearly an average of the constructions obtained using the smallest and flattest perturbations. The smallest perturbation model had the decrease at about 200 meters, but it showed much oscillation, and the flattest perturbation model had only one decrease, but it was somewhat deeper.

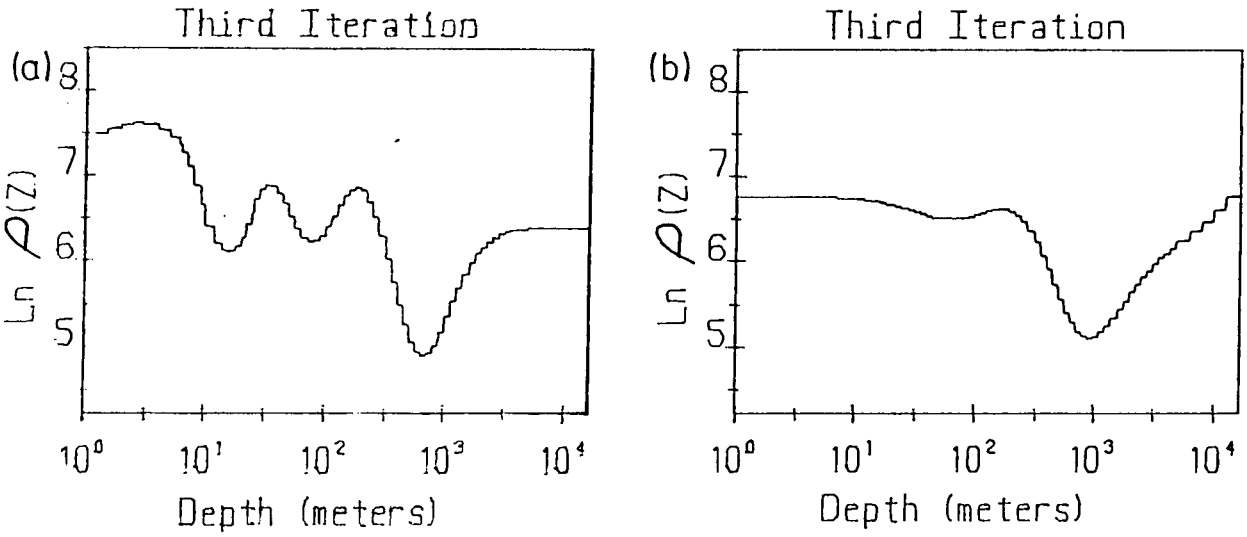

Figure 4.5 a) Smallest perturbation construction for VES 5.
b) Flattest perturbation construction for VES 5.
c) Average model with $\sigma = 0.25$ for VES 5.

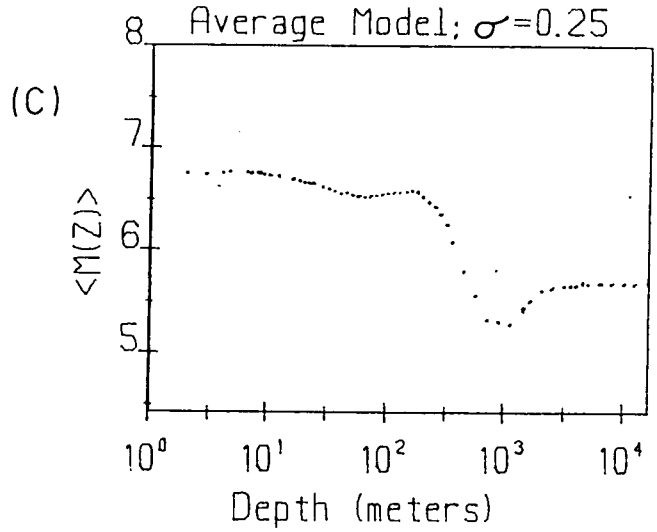

Linearized appraisal does a good job of what it purports to do, and it is a worthwhile exercize after an interpretation has been made. In general linearly appraising models will teach an interpreter not to place too much importance in whatever small scale features a model may have. Instead, only the gross scale features should be considered realistic, and interpreted. One would quickly learn what is resolvable, and what is not, and linearized appraisal would become a formality in interpretation.

4.4 Towards Comprehensive Appraisal

In the nonlinear problems such as D.C. resistivity and M-T, the crux of the problem with appraisal is that models constrcted from a few data are highly nonunique. The degree of nonuniqueness is so great that acceptable models very different from those converged upon by linearized construction may fit the data. Such models would not be linearly close to a linearized construction model and would therefore be beyond the reach of linearized appraisal.

This is well known to be the problem, and some pseudo-solutions to it have been conceived, such as Monte Carlo modelling, and simply comparing models obtained by different construction methods. Neither of these are really the solution because they cannot guarantee that they have swept out the entire space of acceptable models in returning those few.

A more systematic approach has been developed by Oldenburg (1983) where small sections of the model are maximized and minimized to provide information about the average value of the model. This is expressed by the funnel function curves. He also maximizes and minimizes the indefinite integral of the model thus creating the global bounds of the indefinite integral of the model. Intuitively these methods seem to reach much farther into model space than linearized appraisal, but problems with evasive regions possibly harbouring an acceptable model still remain.

One way to envision the relationship between data and models and nonuniqueness is on a two dimensional coordinate system with the axes of Ei(m(z)), and m(z), where every point on the m(z) axis represents a model, and with points proximity to each other representative of their degree of similarity.

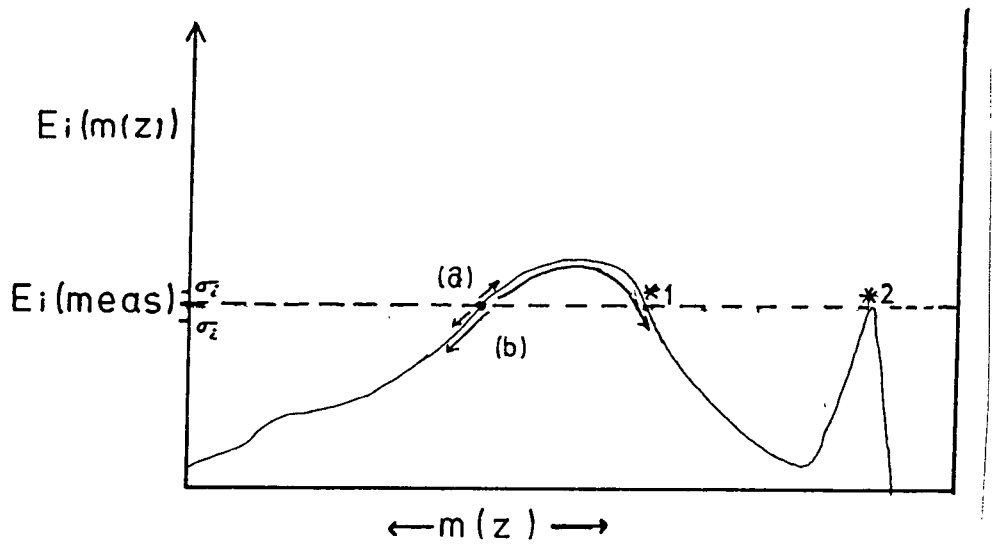

Figure 4.6 A scematic representation of nonuniqueness and appraisal. Linearized appraisal (a) will only appraise models in the linear region around the constructed model. More of model space is scanned in constructing global bound curves (b), but one cannot be certain that inaccessible models such as *2 do not exist.

The functional Ei(m(z)) is plotted out by predicting the i'th datum from every model in model space. Then at every point along the m(z) axis where Ei(m(z))=Ei(meas) for i=1,n there exists an acceptable model.

Now, the appraisal problem is to find and compare all the models m(z) which predict the measured data Ei(meas), for i=1,n. Linearized appraisal scans only the region around $m_0(z)$ where the relationship between Ei and $m_0(z)$ is linear but cannot guarantee against the existence of the models *1 or *2. The methods of Oldenburg may scan much farther and find *1 but still may miss the model at *2. Perhaps they offer the most comprehensive appraisal that will be possible.

Conclusion

In the preceeding chapters an efficient and robust method for inverting direct current resistivity measurements has been presented. Backus and Gilbert's linearized inverse theory has been applied in essentially the same way as Oldenburg (1978) with the one-dimensional structure now approximated by a finite number of layers, and the Hankel transforms computed using the convolutional filter method of Gosh (1971). One-dimensional models can generally be constructed in three or fewer iterations which take 35 seconds on an Amdhal 470 V/8. The construction program has been shown to be fairly insensitive to the starting model chosen and to the presence of moderate errors in the data. Within the ranges tested, neither factor prevented convergence of the program, and varying the starting model seemed not to affect the constructed models representation of the hypothetical structure. On the basis of these results, an efficient, reliable, and robust method for inverting D.C. resistivity measurements has been presented.

Although models may be constructed more quickly using the direct method of Cohen and Yu (1981), the advantage of linearized construction remains in the aspect of appraisal. With linearized construction, the kernels for linearized appraisal are automatically available once the model has converged. In cases where the constructed model is linearly close to the true earth model, unique model averages can be obtained by combining the kernels into an averaging function

and forming its inner product with the model. Linear closeness to the true structure cannot be guaranteed with small data sets, but because there is an uniqueness theorem, the likelihood of this increases with the number of accurate data. Not surprisingly, the implication that this carries over to field experiments is that a large quantity of good guality data is desirable for resolving the underlying resistivity structure. There is no other way to conquer the nonuniqueness problem.

These two factors were taken into consideration in the Anahim resistivity experiment. The data density was high; an expansion factor of 1.24 was used instead of the usual 1.41. So for the array sizes used, a relatively large quantity of data was taken, and the measurement errors on most soundings were less than 3 percent (see figure 3.3). If the topography was more subdued, and there were fewer indications of lateral inhomogenities, both geologically and in the data, then a great deal of confidence could be placed in the models. The underlying rock groups however, are metamorphic, and vary in composition thus depreciating the validity of the one-dimensional approximation. Faults, vertical contacts, and nonplanar topography also violate this approximation. Nevertheless, it is felt that some useful information has been obtained from the constructed models – especially when they are interpreted as a group.

It is immediately apparent that the models divide the soundings into two groups. The two southern soundings produce models with restivities of 800-900 ohm-meters in the first

hundred meters depth, while models with near-surface resistivities averaging 200 ohm-meters are constructed from the four northern soundings. This is indicative of the change in rock types which also divides the soundings into the same two groups.

When the four northern soundings in the Kaza Metasediments are examined as a group, a trend of decreasing average resistivities is seen. There are two possible explanations for this. It could be the result of some nonrandom compositional variations within the Kaza group or, of a temperature gradient increasing to the north. The temperature gradient was chosen as the more probable because it is also indicated by the metamorphic gradation, furthermore, the two models in the Shuswap group to the south show the same trend.

A heat source to the north was inferred from this gradient, and is compatible with both of the major theories for the genesis of the Anahim Volcanic belt: the mantle hot-spot theory, and the edge-effect hypothesis. It is felt that evidence which would support one theory over the other could be obtained through either a more extensive resistivity experiment, or from a net of heat flow measurements. A hot-spot heat source would produce a temperature distribution with radial symmetry, while a line source such as the edge-effect hypothesis calls for, would have laterally symmetric isotherms. If such an experiment strongly indicated either heat source geometry, other parameters such as depth, and power output could be estimated through mathematical

modelling. The thermal conductivity of the Kaza Metasediments would have to be known, and if resistivity measurements were being used, the resistivity of the Kaza rock would have to be calibrated in terms of temperature. In any event, a large amount of good quality data would be required. The uniqueness of any model depends upon both of these factors.

Bibliography

American Geological Institute, 1962, Dictionary of geological terms: Garden City, N.Y., Doubleday & Co., 545 p.

Anderson, W.L., 1979, Numerical integration of related Hankel Transforms of order 0 and 1 by adaptive digital filtering: Geophysics, v.44, p. 1287-1305.

Atwater, T., 1970, Implications of plate tectonics for the Cenozoic tectonic evolution of western North America: Bull. geol. Soc. Am., v. 81, p. 3513-3536.

Backus, G.E., and Gilbert, J.F., 1967, Numerical applications of a formulisn for geophysical inverse problems: Geophys. J. Roy. Astr. Soc., v. 13, p. 247-276.

———— 1968, The resolving power of gross earth data: Geophys. J. Roy. Astr. Soc., v. 16, p. 169-205.

———— 1970, Uniqueness in the inversion of inaccurate gross earth data: Phil. Trans. Roy. Soc., v. A266, p. 123-192.

Baer, A.J., 1973, Bella Coola - Laredo Sound map areas, British Columbia, Geological Survey of Canada Memoir 372, 122 p.

Berg, P.W., and McGregor, J.L., 1966, Elementary partial differential equations: San Francisco, Holden Day, 421 p.

Bevier, M.L., Armstrong, R.L., and Souther, J.G., 1972, Miocene peralkaine volcanism in west-central British Columbia — its temporal and plate tectonic setting: Geology, v. 7, p. 389-392.

Boyce, W.E., and DiPrima, R.C., 1977, Elementary differential equations and boundary value problems: Toronto, John Wiley & Sons, 3rd ed., 421 p.

Campbell, R.B., 1967, Canoe River, British Columbia: Geological Survey of Canada, Map 15 - 1967.

Carslaw, H.S., and Jaeger, J.C., 1976, Conduction of heat in solids: Oxford, Clarendon Press, 2nd ed., 510 p.

Clark, C., 1972, The theoretical side of calculus: Belmont, Calif., Wadsworth, 240 p.

Coen, S., and Yu, M.W.H., 1981, The inverse problem of the direct current conductivity profile of a layered earth: Geophysics, v. 46, p. 1702-1713.

Fullagar, P.K., 1980, Inversion of horizontal loop electromagnetic soundings over a stratified earth: Ph.D. thesis, Univ. of B.C., 264 p.

Garland, G.D., 1979, Introduction to geophysics - mantle, crust and core: Toronto, W.B. Saunders, 2nd ed., 494 p.

Gosh, D.P., 1971a, The application of linear filter theory to the direct interpretation of geoelectric resistivity soundings measurements: Geophys. Prosp., v. 19, p. 192-217.

———— 1971b, Inverse filter coefficients for the computation of apparent resistivity standard curves for a horizontally stratified earth: Geophys. Prosp., v. 19, p. 769-775.

Gradshten, I.S., and Ryzhik, I.M., 1965, Tables of integrals series and products: New York, Academic Press, 1086 p.

Horn, J.R., 1982, A snapshot of the Queen Charlotte fault zone obtained from P-wave refraction data: M.Sc. thesis, Univ. of B.C., 79 p.

Inman, J.R., 1975, Resistivity inversion with ridge regression: Geophysics, v. 40, p. 798-817.

Keller, G.V. and Frischknecht, F.C., 1977, Electrical methods in geophysical prospecting: Edinburgh, Pergamon, 519 p.

Koefoed, O., 1972, A note on the linear filter method of interpreting resistivity sounding data: Geophys. Prosp., v. 20, p. 403-405.

Kunetz, G., 1966, Principals of direct current resistivity prospecting: Berlin, Gebruder Borntraeger, 103 p, (English translation from the French by Robert Van Nostrand.)

Lancsoz, C., 1961, Linear differential operators: London, Van Nostrand, 564 p.

Langer, R.E., 1933, An inverse problem in differential equations: Am. Math. Soc. Bull., ser. 2, v. 39, p. 814-820.

———— 1936, On the determination of earth conductivity from observed surface potentials: Am. Math. Soc. Bull., ser. 2, v.42, p. 747-754.

Maillet, R., 1947, The fundamental equations of electrical prospecting: Geophysics, v. 12, p. 529-556.

Milne, R.D., 1980, Applied functional analysis: London, Pitman, 501 p.

Minster, J.B., Jordan, T.H., Molnar, P., and Haines, E., 1974, Numerical modelling of instantaneous plate tectonics: Geophys. J. Roy. Astr. Society, v. 36, p. 541-576.

Muscat, M., 1933, Potential distribution about an electrode on the surface of the earth: Physics, v. 4, p. 129-147.

Oldenburg, D.W., 1978, The interpretation of direct current resistivity measurements: Geophysics, v. 43, p. 610-625.

———— 1979, One-dimensional inversion of natural source magnetotelluric observations: Geophysics, v. 44, p. 1218-1244.

———— 1983, Funnel functions in linear and nonlinear appraisal. (In press).

Parker, R.L., 1977a, Understanding inverse theory: Ann. Rev. Earth Planet. Sci., 1977, p. 35-64.

———— 1977b, The Fréchet derivative for the one dimensional electromagnetic induction problem: Geophys. J. Roy. Astr. Soc., v. 49, p. 543-547.

Parker, R.L., and Whaler, K.A., 1981, Numerical methods for establishing solutions to the inverse problem of electromagnetic induction: J. Geophys. Res., v. 86, No. B10, p. 9574-9584.

Pell, J., and Simony, P.A., 1981, Stratigraphy, structure and metamorphism in the southern Cariboo Mountains, British Columbia: Current Research Part A, Geological Survey of Canada, Paper 81-A1, p.227-230.

Peters, L.J., and Bardeen, J., 1932, Some aspects of electrical prospecting applied in locating oil structures: Physics, v. 2, p. 103-122.

Premier Geophysics Inc., 1979, Note on mechanical waveform separation for filtering chart records: internal operating memo by Greg Shore, Premier Geophysics, 2 p.

Riddihough, R.P., 1977, A model for recent plate interactions off Canada's west coast: Can. J. Earth Sci., v. 4, p. 384-396.

Riddihough, R.P., and Hyndman, R.D., 1976, Canada's active western margin - the cause for subduction: Geoscience Canada, v. 3, p. 269-278.

Rybach, L., and Muffler, L.J.P., 1981, Geothermal systems principles and case histories: Toronto, John Wiley & Sons, 453 p.

Schlax, M.G., and Shore, G.A., 1981, D.C. resistivity survey near Blue River, B.C., June, July, 1981. for Geological Survey of Canada, Anahim Project, 24 p.

Shields, P.C., 1968, Elementary linear algebra: New York, Worth, 393 p.

Slichter, A.B., 1933, The interpretation of the resistivity prospecting method for horizontal structures: Physics, v. 4, p. 307-322.

Souther, J.G., 1970, Volcanism and its relationship to recent crustal movement in the Canadian Cordillera: Can. J. Earth Sci., v.7, p. 553-568.

———— 1977, Volcanism and tectonic environments in the Canadian Cordillera - A second look in Barager, W.R.A., and others eds., Volcanic regimes in Canada: Geol. Assoc. of Canada, Special Paper 16, p.3-27.

Stacey, R.A., 1974, Plate tectonics, volcanism and the lithosphere in British Columbia: Nature, v. 250, p. 133-134.

Tipper, H.G., 1969, Anahim Lake map-area British Columbia: Geological Survey of Canada, Map 1202A.

Watson, G.N., 1966, A treatise on the theory of Bessel functions: Cambridge University Press, 2nd ed., 804 p.

Yorath, C.J., and Chase, R.L., 1981, Tectonic history of the Queen Charlotte Islands and adjacent areas - a model: Can. J. Earth Sci., v. 18, p. 1717-1739.

Zohdy, A.A.R., 1975, Automatic interpretation of Schlumberger sounding curves using modified Dar Zarrouk functions: Geolog. Survey. Bull., 1313-E, 39 p.

Appendix A

Evaluation of the Modal Coefficient A(λ)

Separating the variables in the conservation of current equation resulted in the following expression for the potential.

$$V(r,z) = \int_0^\infty A(\lambda)H(z,\lambda)J_0(\lambda r)\, d\lambda \qquad (A.1)$$

V(r,z) is a continuous Bessel series expansion, or Hankel Transform. The modal coefficients, A(λ) must be evaluated. Using a condition implied by the conservation of current, Oldenburg (1978) calculated a computationally economical expression for A(λ). Specifically, the condition used is that the surface integral of current flux j, through an infinitely long cylinder centered on the current source must equal I, the source current.

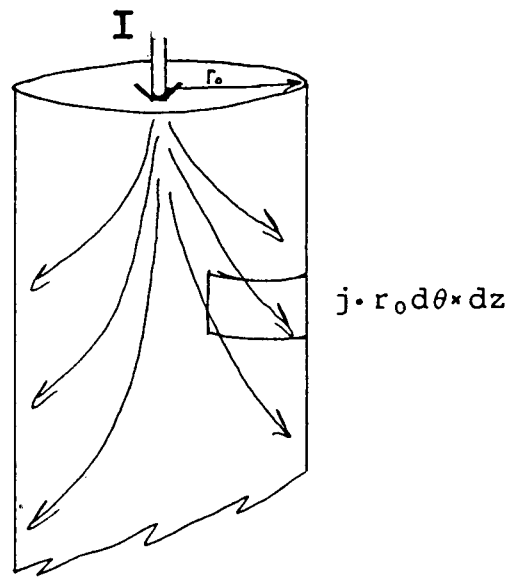

The current, I, equals

$$\int_0^{\infty}\int_0^{2\pi} j(r_o,z) \cdot r_o d\theta \; dz \qquad (A.2)$$

$d\theta$, and dz are unit vectors in the θ, and z directions, and r_o is the radius of the cylinder.

$$I = 2\pi r_o \int_0^{2\pi} j_r(r_o,z) \; dz \qquad (A.3)$$

And from Ohm's Law, $j(r_o,z) = - \frac{\nabla V(r_o,z)}{\rho(z)}$,

so the r component of $j(r_o,z)$ is

$$j_r(r_o,z) = \frac{-1}{\rho(z)} \frac{\partial V(r_o,z)}{\partial r} \qquad (A.4)$$

Using the expression for V(r,z) from (A.1),

$$j_r(r_o,z) = \frac{1}{\rho(z)} \int_0^{\infty} A(\lambda) J_o'(r_o\lambda) H(z,\lambda) \; d\lambda \qquad (A.5)$$

It can be proven (Berg+McGregor,1966) that $J_o'(r\lambda) = \lambda J_1(r\lambda)$.

$$j_r(r_o,z) = \frac{1}{\rho(z)} \int_0^{\infty} \lambda A(\lambda) J_1(r_o\lambda) H(z,\lambda) \; d\lambda \qquad (A.6)$$

Therefore,

$$I = 2\pi r_o \int_o^\infty \lambda A(\lambda) J_1(r_o\lambda) \int_o^\infty \frac{H(z,\lambda)}{\rho(z)}\, dz d\lambda \qquad (A.7)$$

It is easy to see that if $A(\lambda) = \frac{I}{2\pi\lambda} \int_o^\infty \frac{\rho(z)}{H(z,\lambda)}\, dz$

the resultant would be simply:

$$I = I r_o \int_o^\infty J_1(r_o\lambda)\, d\lambda,$$

which contains one of the analytic Hankle Transforms (Gradshteyn + Ryzhik, no. 6.511.1, p.665, 1965).

$$\frac{1}{r_o} = \int_o^\infty J_1(r_o\lambda)\, d\lambda \qquad (A.8)$$

$A(\lambda)$ can be further simplified by noting from equation (1.4b),

$$\frac{H(z,\lambda)}{\rho(z)} = \frac{1}{\lambda^2}\left(\frac{H'(z,\lambda)}{\rho(z)}\right)'$$

and integrating both sides from 0 to ∞.

$$\int_o^\infty \frac{H(z,\lambda)}{\rho(z)}\, dz = \frac{1}{\lambda^2} \frac{H'(z,\lambda)}{\rho(z)} \Bigg|_o^\infty$$

$H(z,\lambda)$ is a monotonically decreasing function (Langer, 1933), and consequently goes to zero as z goes to infinity. Thus

$$\int_o^\infty \frac{H(z,\lambda)}{\rho(z)}\, dz = \frac{-1}{\lambda^2} \frac{H'(0,\lambda)}{\rho(0)} \qquad (A.9)$$

simplifying $A(\lambda)$ to

$$A(\lambda) = \frac{-I\rho_o}{2\pi} \frac{\lambda}{H'(0,\lambda)}, \qquad (A.10)$$

where ρ_o is the surface resistivity. The final form of the potential equation is:

$$V(r,z) = \frac{-I\rho_o}{2\pi} \int_0^\infty \lambda \frac{H(z,\lambda)}{H'(0,\lambda)} J_o(r\lambda)\, d\lambda \qquad (A.11)$$

Appendix B

Solving for $H(z,\lambda)$ in a Layered Medium

In a continuous resistivity structure $\rho(z)$, the Sturm-Liouville equation,

$$H'' - \frac{\rho'}{\rho}H' + \lambda^2 H = 0 \qquad (B.1)$$

must be solved before the potential distribution can be calclated. Both $H(0,\lambda)$ and $H'(0,\lambda)$ are needed from $\lambda=0$ to $\lambda=\infty$ to perform the integral in the potential difference equation.

$$\int_0^\infty \lambda \frac{H(0,\lambda)}{H'(0,\lambda)} Cj(\lambda)\, d\lambda \qquad (B.2)$$

Obtaining $H(0,\lambda)$ and $H'(0,\lambda)$ for this kind of structure is an onerous task. If, however, $\rho(z)$ can be approximated by a finite number of layers, each isotropic, having a constant resistivity, then equation (B.1) is vastly simplified. The ρ' term is zero within each layer so the equation

$$H'' + \lambda^2 H = 0 \qquad (B.3)$$

describes H within any single layer. The solution of this in the j'th layer is of course exponential functions.

$$Hj(z_j,\lambda) = Aje^{-\lambda z_j} + Bje^{\lambda z_j} \qquad (B.4)$$

where z_j is the depth from the top of the j'th layer. This general solution applies in every layer. The boundry conditions for the current and potential at layer interfaces determine the A and B coefficients for each layer. The layering scheme and variables used are illustrated below.

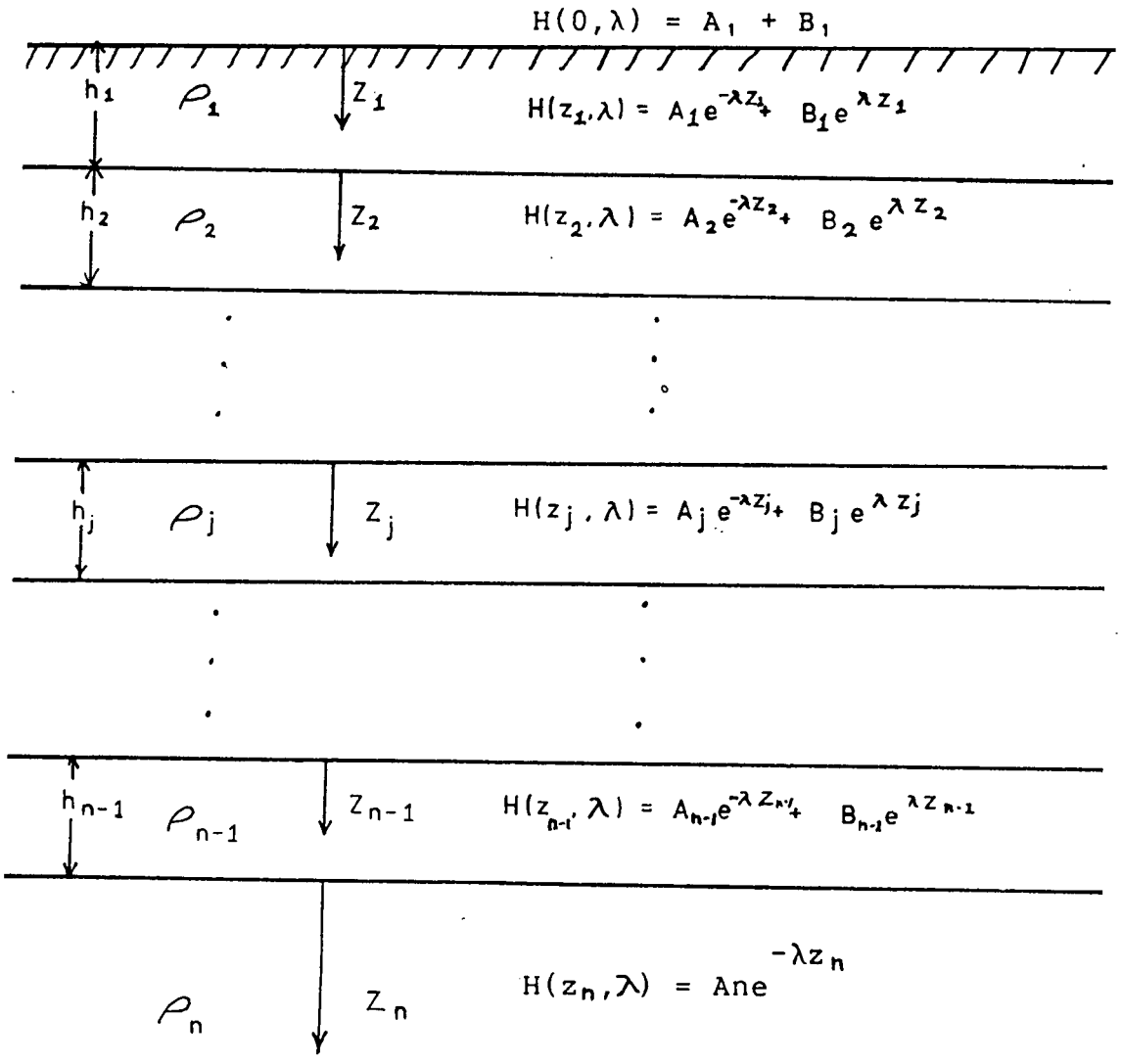

In the deepest layer, Bn must be zero because the current density decays to zero at great depth. Across every layer boundary, the potential distribution, and the vertical component of current density vary continuously (Keller and Frischknecht, 1977). At the bottom of the j'th layer, the potential is continuous.

$$V_j(r,h_j) = V_{j+1}(r,0)$$

$$V_j(r,h_j) = \frac{-I\rho_0}{2\pi}\int_0^\infty \left(\frac{Aje^{-\lambda h_j}}{A_1} + \frac{Bje^{\lambda h_j}}{B_1} \right) J_0(\lambda r)\, d\lambda$$

$$V_{j+1}(r,0) = \frac{-I\rho_0}{2\pi}\int_0^\infty \left(\frac{Aj_{+1}}{A_1} + \frac{Bj_{+1}}{B_1} \right) J_0(\lambda r)\, d\lambda \qquad (B.5)$$

Equating the kernels,

$$Aje^{-\lambda h_j} + Bje^{\lambda h_j} = Aj_{+1} + Bj_{+1} \qquad (B.6)$$

The vertical component of current density is also continuous.

$$J_z(r,h_j) = J_z(r,0)$$

$$\frac{1}{\rho_j}\frac{\partial}{\partial z}Vj(h_j,r) = \frac{1}{\rho_{j+1}}\frac{\partial}{\partial z}Vj_{+1}(0,r) \qquad (B.7)$$

$$-Aje^{-\lambda h_j} + Bje^{\lambda h_j} = \frac{\rho_j}{\rho_{j+1}}(-Aj_{+1}+Bj_{+1}) \qquad (B.8)$$

Combining equations (B.6) and (B.8) results in the relations for Aj and Bj in terms of Aj_{+1} and Bj_{+1},.

$$Aj = e^{\lambda h_j}\left[\left(1+\frac{\rho_j}{\rho_{j+1}}\right)/2\ A_{j+1}(\lambda) + \left(1-\frac{\rho_j}{\rho_{j+1}}\right)/2\ B_{j+1}(\lambda)\right] \qquad (B.9a)$$

$$Bj = e^{-\lambda h_j}\left[\left(1-\frac{\rho_j}{\rho_j}\right)/2\ A_{j+1}(\lambda) + \left(1+\frac{\rho_j}{\rho_j}\right)/2\ B_{j+1}(\lambda)\right] \qquad (B.9b)$$

Using the boundary condition that B in the deepest layer is zero, and setting A in that layer to unity, renders A, and B in every other layer up to the surface immediately available through the recurrsion relations (B.9a) and (B.9b). The constant to which A in the deepest layer is equated is of no particular significance (although every A and B is scaled by it), because it is normalized out of the final expressions for the potential difference and the Fréchet kernel. In a layered medium, these equations are:

$$\Delta Vi = \frac{I\rho_0}{2\pi}\int_0^\infty \left[\frac{A_1(\lambda) + B_1(\lambda)}{-A_1(\lambda) + B_1(\lambda)}\right] Ci(\lambda)\ d\lambda \qquad (B.10)$$

and,

$$Gi(z_j) = \frac{\rho_0}{\rho_j}\int_0^\infty \lambda\left[\frac{Aj(\lambda)e^{-\lambda z_j} + Bj(\lambda)e^{\lambda z_j}}{A_1(\lambda)^2 - 2A_1(\lambda)B_1(\lambda) + B_1(\lambda)^2}\right] Ci(\lambda)\ d\lambda \qquad (B.11)$$

Ideally, Aj and Bj are very easy to calculate with the recurrsion relations (B.9), but complication can arise however, when calculating A's and B's numerically. The A's may at some point become too large for machine storage when

calculating successively shallower A's. Likewise Bj may become too small. This problem is skirted by starting the recurrsion relations at a shallower depth with the following boundary conditions.

$$A + B = 0 \tag{B.12a}$$

$$A - B = 1 \tag{B.12b}$$

Appendix C

Frechet Differentiability of the Data Functionals

For the successful convergence of an iterative scheme, such as the one used here to construct resistivity models, continuity is essential. Its convergence depends upon the derivatives of the functionals with respect to the model vector indicating the direction in which to perturb a model towards fitting the data. And if the data functionals are not continuous with respect to their model argument, they will not be everywhere differentiable and areas will exist in data space for which no acceptable model can be converged upon using Newton's method. Therefore, the data functionals must be continuously differentiable for any model vector in model space. This is the Fréchet differentiability condition.

C-1 Development of the Idea.

I will now show that the mere existence of the derivative of a functional (or a functional of many variables) does not guarantee continuity, but that continuity can be established using the differential function.

Regressing momentarily to functions of a single variable, the derivative, f'(x), is defined as the limit

$$\lim_{\lambda \to 0} \frac{f(x+\lambda) - f(x)}{\lambda} \qquad (C.1)$$

where it exists (Milne,1980). Such a function is said to be

differentiable where this limit exists, moreover, the continuity of f(x) at x is certified by the existence of the limit (Clark, 1972, p83). For functions of many variables, however, continuity at $(x_1,x_2,x_3,....x_n)$ is not implied by the existence of the partial derivatives. An example of this is given in Milne (1980, p285).

$$f(x_1,x_2) = \begin{cases} x_1+x_2 & \text{if } x_1 \text{ or } x_2 = 0 \\ 1 & \text{otherwise} \end{cases}$$

At (0,0), both partials exist, although the function is discontinuous. And as stated earlier, continuity is crucial for the successful convergence of an iterative scheme such as we use.

This somewhat suprising result is also true for functionals; derivatives may exist without the functional being continuous. We cannot then take the existence of derivatives of our data to mean that they are Fréchet derivatives or that the functionals are continuous.

This difficulty in analysing continuity is overcome through the use of the differential. For functions of a single variable, it is defined wherever f'(x) exists as follows:

$$df(x;s) = f'(x)s \qquad (C.2)$$

where s is an increment along the x axis. Graphically, df(x;s) is a linear approximation to the change in f(x) over the interval from x to x+s. When λ is replaced by s in the

definition of the derivative, we have:

$$df(x;s) = \lim_{s \to 0} f(x+s) - f(x), \qquad (C.3)$$

and the following inequality,

$$\left| \frac{f(x+s) - f(x)}{s} - f'(x) \right| < \epsilon, \qquad (C.4)$$

provided $|s|$ is sufficiently small. Alternatively, for every $\epsilon>0$ there exists an interval containing x and s such that

$$| f(x+s) - f(x) - f'(x)s| < \epsilon|s|. \qquad (C.5)$$

By extending the concept of the differential to functions of n real variables,

$$df(x;s) = \sum_{i=1}^{n} \frac{\partial f}{\partial x_i}(x)s_i \qquad \text{where } s=(s_1,s_2,s_3,.....s_n) \text{ and } x=(x_1,x_2,x_3,.....x_n),$$

the connection between the differential and continuity can now be elucidated. If for any $\epsilon>0$ there exists an s in the neighbourhood of x, such that

$$| f(x+s) - f(x) - df(x;s) | < \epsilon\|s\|_2, \qquad (C.6)$$

f(x) is differentiable at x. This condition is sufficient for the continuity of f(x) at x. In the example from Milne, for $\epsilon<1$, there is no small s for which the inequality will hold, so the function is not differentiable at (0,0).

We now generalize further to operators which take a vector from R^n to R^m. Let E be an operator which takes a vector, x, from a vector space V to a normed vector space U. If the limit

$$dE(x;s) = \lim_{\lambda \to 0} \frac{E(x+\lambda s) - E(x)}{\lambda} \qquad (C.7)$$

exists, it is the Gateaux Differential of E at x. If, in addition, dE(x;s) exists for <u>all</u> s in V, then E is Gateaux differentiable at x. It should be noted that the existence of a Gateaux differential does not guarantee Gateaux differentaibility at that x; it may be the result of some fortunate choice of s. Continuity of E is therefore not proven by the existence of dE(x;s) (Milne, 1980, p289). In addition, V must be normed before continuity of E can be defined.

If V and U are both normed vector spaces, and E takes a vector in V to U, it is Fréchet differentiable at $x \subset V$ if the continuous linear operator E'(x) exists such that

$$E(x+s) - E(x) = E'(x)s + \epsilon(x;s) \qquad (C.8)$$

for all vectors $s \subset V$ with the limit

$$\lim_{\|s\|_v \to 0} \frac{\|\epsilon(x;s)\|_v}{\|s\|_v} = 0.$$

$E'(x)$ is the Fréchet derivative at x and it is unique. In the limit $\|s\|_v \to 0$, the standard expression for the derivative, with the correct norms, applies.

$$\lim_{\|s\|_v \to 0} \frac{E(x+s) - E(x)}{\|s\|_v} = E'(x) \qquad (C.9)$$

C-2 Application to the D.C. Resistivity Problem

Let us now move to the specific case of the data functionals in the D.C. resistivity problem. The nonlinear functionals (Ei;i=1,n) are a subset of vector operators which take the model vectors from L_2 to points in R. Both the spaces L_2 and R are normed, with the following integral defining the functionals.

$$Ei = \int_0^\infty \lambda\, S(0,\lambda) Ci(\lambda)\, d\lambda \qquad (C.10a)$$

$$\text{where} \quad S' + wS + \lambda^2 S^2 - 1 = 0 \qquad (C.10b)$$

A linear approximation to the differential may be obtained by letting δw be the incremental vector s in the previous formalism.

$$dEi(w;\delta w) \simeq Ei(w+\delta w) - Ei(w) \qquad (C.11)$$

Now the continuity of Ei(w) must be checked. Ei is continuous if for any $\epsilon>0$, there exists a $\delta>0$ such that

$$|Ei(w+\delta w) - Ei(w)| < \epsilon \text{ whenever } \|\delta w\|_2<\delta \qquad (C.12)$$

for any w in L_2 (Milne, 1980, p129). We know that

$$Ei(w+\delta w) = \int_0^\infty (S(0,\lambda)+\delta S(0,\lambda))Ci(\lambda)\, d\lambda \qquad (C.13)$$

and δS is linear in δw

$$\delta S(0,\lambda) = \frac{\rho_0}{H'(0)} \int_0^\infty \frac{HH'\delta\, w(z)}{\rho(z)}\, dz \qquad (C.14)$$

which makes the difference $\delta Ei(\delta w)$ also linear in δw.

To find δ, the inequality is expressed for the n data functionals, and the resulting set of linear equations $(\delta Ei(\delta w) = \epsilon; i=1,n)$ is solved for the smallest δw, the L_2 norm of which is our δ. Clearly since δEi is the inner product of the Fréchet derivative and δw (equation 1.18), δEi will be less than ϵ for any δw having a two norm less than δ. The inequality holds; Ei <u>is</u> continuous with respect to w. Therefore, the data functionals are Fréchet differentiable. This is an intuitively correct result, as we would expect a small change in the resistivity to produce a correspondingly small change in the data.

Thus for small $\|\delta w\|_2$, the difference

$$\delta Ei = Ei(w+\delta w) - Ei(w) \qquad (C.15)$$

approximates the Fréchet differential, $dEi(w;\delta w)$. In the iterative construction method, we make this approximation using the misfit to the i'th datum as δEi, then solve for the perturbation.

Appendix D

Evaluating Indefinite Integrals

Computing the flattest perturbation involves manipulating indefinite integrals of Fréchet kernels and, as the last step, integrating $\delta m'(z)$ to obtain the perturbation, $\delta m(z)$. We want to use everything we know about these functions to integrate them as accurately and as quickly as possible. The two indefinite integrals needed are:

$$Hi(z) = \int_0^z Gi(u)\, du \quad \text{for } i=1,n \tag{D.1}$$

and

$$\delta m(z) = \int_0^z \delta m'(u)\, du \tag{D.2}$$

D-1 Indefinite Integrals of Fréchet Kernels

The Fréchet kernels are obtained through a Hankel transform (equation 1.28), and are evaluated above and below each layer boundary. They are assumed to vary linearly with z inside that layer. Thus, within the l'th layer $Gi(z_l)$ is represented by

$$Gi(0_l) + \{Gi(h_l)-Gi(0_l)\}\frac{z_l}{h_l} \tag{D.3}$$

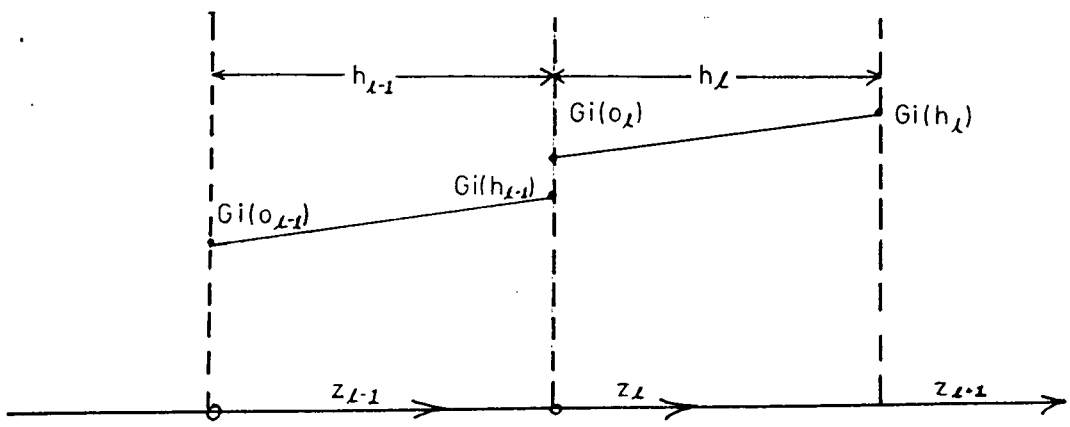

The indefinite integral over this layer has both a linear term and a squared term in z_ℓ.

$$\int_0^{z_\ell} Gi(u)\,du = Gi(0_\ell)z_\ell + \{Gi(h_\ell)-Gi(0_\ell)\}\frac{z^2_\ell}{2h_\ell} \qquad (D.4)$$

This must be added to the integrals of Gi(z) from 0 to h_κ, for the l-1 shallower layers. The full indefinite integral, $Hi(z_\ell)$ is therefore,

$$\sum_{\kappa=1}^{\ell-1}\{Gi(0_\kappa)+Gi(h_\kappa)\}\frac{h_\kappa}{2} + Gi(0_\ell)z_\ell + \{Gi(h_\ell)-Gi(0_\ell)\}\frac{z^2_\ell}{2h_\ell} \qquad (D.5)$$

Unlike Gi(z), Hi(z) needs to be evaluated only once at every layer boundary because the indefinite integral is continuous. Thus Hi(z) at the l'th boundary is:

$$\sum_{\kappa=1}^{\ell}\{Gi(0_\kappa)+Gi(h_\kappa)\}\frac{h_\kappa}{2} \qquad (D.6)$$

The inner product of Hi(z) and Hj(z) is calculated by multiplying equation D.5 by its j'th counterpart and integrating the product, layer by layer, from z=0 to z=Zmax.

D-2 Obtaining δm(z) from δm'(z)

Once the inner product matrix has been inverted, and the chi-squared acceptable β coefficients have been calculated, the preturbation's derivative is available.

$$\delta m'(z) = \sum_{i=1}^{n}\beta_i Hi(z) \qquad (D.7)$$

Since there is a greater probability of knowing the surface resistivity than that at depth, the integration constant will be set to zero at the surface. So,

$$\delta m(z) = \int_0^z \delta m'(u)\, du \qquad (D.8)$$

Now, instead of linearly interpolating $\delta m'(z)$ between layer boundaries, it is more accurate to integrate equation D.7 directly. This is possible because the character of Hi(z) between the layers is known. Thus,

$$\delta m(z) = \sum_{i=1}^{n} \beta_i \int_0^z Hi(u)\, du, \qquad (D.9)$$

and the indefinite integral of Hi(z) is the second indefinite integral of Gi(z).

$$\int_0^z Hi(u)\, du = \int_0^z \int_0^u Gi(v)\, dv\, du \qquad (D.10)$$

Assumptions regarding the nature of $\delta m'(z)$ were avoided. Equation D.10 results in an expression similar to D.5 for the indefinite integral of Hi(z) in the l'th layer. The constants are unchanged with the first term now multiplied by z_l, the second term by $z_l^2/2$, and the third by $z_l^3/6$.

Appendix E

Winnowing Eigenvalues

Owing to the presence of errors in the data, the smallest and flattest perturbation equations should not be solved exactly. Instead, coefficients which solve the n equations according to the chi-squared criterion should be found.

For the smallest perturbations this means finding the a coefficients which solve

$$\delta Ei = \Gamma_{ij}\ a_j \qquad \text{for } i=1,n \tag{E.1}$$

such that

$$\sum_{i=1}^{n} \left[\frac{\delta Ei - \Gamma_{ij}\ a_j}{\sigma_i}\right]^2 = n \tag{E.2}$$

In practice, normalized perturbation equations are solved for normalized alpha coefficients.

$$\sum_{i=1}^{n} \left[\delta\hat{E}i - \hat{\Gamma}_{ij}\ \hat{a}_j\right]^2 = n \tag{E.3}$$

When eigenvalues have been winnowed to obtain $\hat{a}$ we will call it $\hat{a}^{\dagger}$, and call the products $\hat{\Gamma}_{ij}\ \hat{a}_j^{\dagger}$ truncated data misfits, $\delta\hat{E}i^{\dagger}$. Now equation E.3 can be written as

$$\sum_{i=1}^{n} \left[\delta\hat{E}i - \delta\hat{E}i^{\dagger}\right]^2 = n \tag{E.4}$$

where

$$\delta\hat{E} = U\Lambda U^{T}\ \hat{a} \tag{E.5a}$$

and

$$\delta\hat{E}^{\dagger} = U\Lambda U^{T}\ \hat{a}^{\dagger} \tag{E.5b}$$

Truncated alpha coefficients are obtained by truncating the eigenvalue matrix and the orthonormal matrix U (see section 2-4.2, equation 2.19).

$$\hat{a}^{\dagger} = U^{\dagger}\ \Lambda^{-1\dagger}\ U^{T\dagger}\delta\hat{E} \tag{E.6}$$

It follows from equations E.5a, and E.5b, that

$$\delta\hat{E} = U\ \Lambda\ U^{T}\ U\ \ \Lambda^{-1}\ U^{T}\delta\hat{E} \quad = \quad U\ U^{T}\delta\hat{E} \tag{E.7}$$

$$\delta\hat{E}^{T} = U\ \Lambda\ U^{T}\ U^{\dagger}\ \Lambda^{-1\dagger}\ U^{T\dagger}\delta\hat{E} \quad = \quad U\ I^{\dagger}\ U^{T\dagger}\delta\hat{E} \tag{E.8}$$

The $n \times m$ matrix $I^{\dagger}$ is a zero matrix with an $m \times m$ identity matrix in the top m rows, where n-m is the number of eigenvalues that have been winnowed. It is the product $\Lambda U^{T}U^{\dagger}\Lambda^{-1\dagger}$.

$$\begin{array}{cc} & \overbrace{\hphantom{1\quad 1\quad 1\quad 1\quad 1}}^{m} \\ n\left\{\begin{array}{c} \\ \\ \\ \\ \\ \\ \end{array}\right. & \left|\begin{array}{ccccc} 1 & & & & 0 \\ & 1 & & & 0 \\ & & 1 & & 0 \\ & & & 1 & 0 \\ & & & & 1 \\ 0 & \cdots & \cdots & \cdots & \cdots \\ 0 & 0 & 0 & 0 & 0 \end{array}\right| \left.\begin{array}{c} \\ \\ \\ \\ \\ \\ \end{array}\right\} m \end{array}$$

and equation E.4 can now be written as length of the

difference vector, squared.

$$\| U\{U^T \delta\hat{E} - I^{\dagger} U^{T\dagger} \delta\hat{E}\} \|^2 = n \qquad (E.9)$$

It is apparent that $I^{\dagger}U^{T\dagger}\delta\hat{E}$ is a vector in which the first m values are the normalized data misfits rotated by U^T, and the last n-m values are zeros. Identifying $U^T\delta\hat{E}$ as $\delta\hat{E}rot$, equation E.9 is the squared sum from 1 to n of the following vector

$$[\, 0_1,\ 0_2, \ldots,\ 0_m, \delta\hat{E}rot_{m+1}, \ldots, \delta\hat{E}rot_n] \qquad (E.10)$$

after it has been rotated by U. Since U is orthonormal, this last rotation will not change the length, and therefore will make no difference to n. Thus, the misfit condition is:

$$[\, 0_1 + 0_2 + \ldots + 0_m + \delta\hat{E}rot^2_{m+1} + \ldots + \delta\hat{E}rot^2_n\,] = n, \qquad (E.11)$$

and the value of m for which makes this true is most easily found by summing the vector $\delta\hat{E}rot$ in the direction from n to 1. Then the minimum m for which

$$\sum_{i=n}^{m+1} \delta\hat{E}rot_i^2 \quad \leq \quad n \qquad (E.12)$$

is the number of eigenvalues which are kept. This is the way in which the number of eigenvalues to be winnowed for a chi-squared acceptable set of alpha coefficients is determined.

Appendix F

The Schlumberger Data

Listed below are the apparent resistivities and AB/2 distances which formed the data set used in chapter 3. The third column in each case is the standard deviation level in percent that was assigned to the datum.

Current and voltage information were not directly available, but were recovered using the Schlumberger apparent resistivity formula.

$$\frac{\Delta V}{I} = \rho a \times \frac{MN}{\pi (AB/2)^2} \qquad \text{for } MN < .1 \times AB/2$$

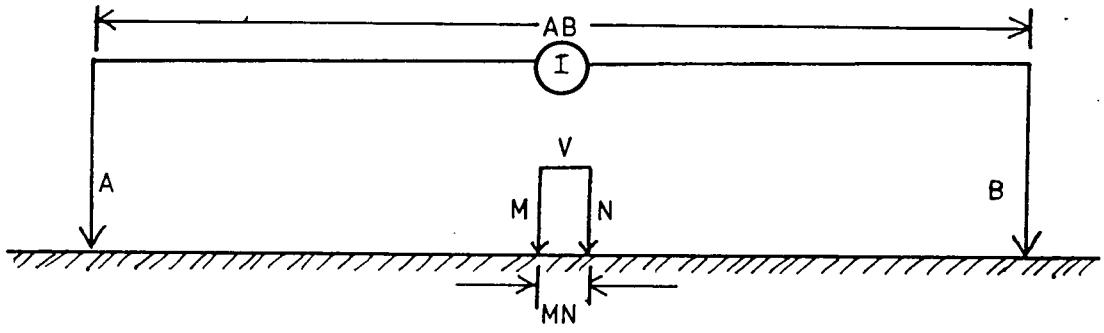

Schlumberger Configuration

VES 1

ρa	AB/2 (meters)	std. dev.
1600	25	10
810	50	10
460	75	10
210	100	10
140	150	10
150	200	10
160	300	10
180	400	10
230	500	10

VES 2

ρa	AB/2 (meters)		std. dev.
210	25		10
190	50		10
195	75		10
180	100		10
180	150		10
160	200		10
120	300		10
82	400		10
82	500		10
110	737	(corrected	10
120	975		10
140	1225	for	10
145	1495		10
120	1725	noncolinearity)	10
110	2000		10

VES 3

ρa	AB/2 (meters)	std. dev.
1200	25	10
800	50	10
490	75	10
480	100	10
330	150	10
260	200	10
	--- data not used ---	
360	300	
180	400	
1250	500	
550	750	

VES 4

ρa	AB/2 (meters)	std. dev.
1350	15	10
1350	25	10
1200	50	10
1150	75	10
1200	100	10
1175	150	10
1100	200	10
1100	300	10
800	400	15
450	500	40
750	750	20
1200	1000	20

VES 5

ρa	AB/2 (meters)	std. dev.
860	25	10
760	50	10
660	75	10
640	100	10
710	150	10
900	200	10
650	300	10
550	400	10
530	500	10
460	750	10
390	1000	10
310	1250	10
250	1500	10
230	1750	10
240	2000	10

VES 6

ρa	AB/2 (meters)	std. dev.
230	25	10
250	50	10
240	75	10
240	100	10
220	150	10
205	200	10
190	300	10
210	400	10
220	500	10
290	750	10
240	1000	10